

AD-A128 675 IMAGING SENSOR DEVELOPMENT FOR SCATTERING ATMOSPHERES  
(U) ENVIRONMENTAL RESEARCH INST OF MICHIGAN ANN ARBOR  
RADAR AND OPTICS DIV A M TAI MAR 83 ERIM-155600-3-F  
UNCLASSIFIED ARBRL-CR-00508 DAAK11-81-K-0005 F/G 17/8

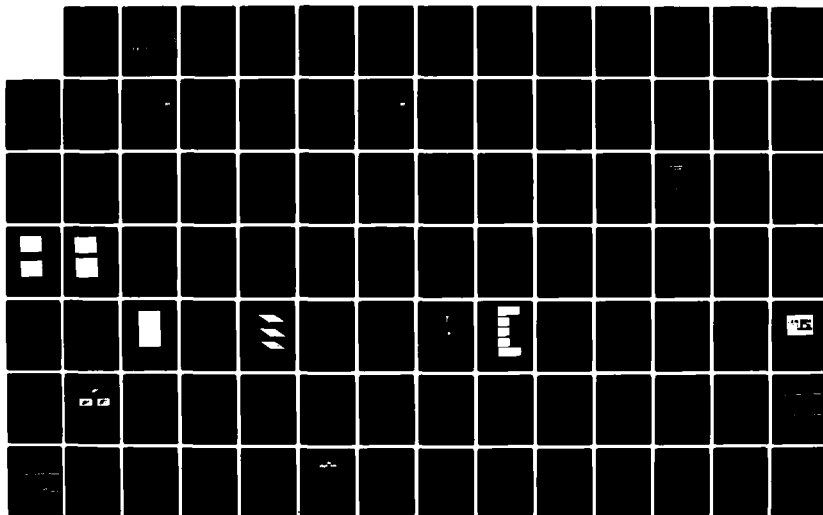
IMAGING SENSOR DEVELOPMENT FOR SCATTERING ATMOSPHERES  
(U) ENVIRONMENTAL RESEARCH INST OF MICHIGAN ANN ARBOR  
RADAR AND OPTICS DIV A M TAI MAR 83 ERIM-155600-3-F  
ARBRL-CR-00508 DAAK11-81-K-0005 F/G 17/8

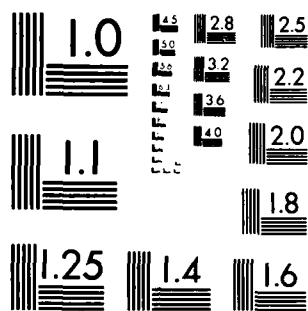
112

UNCLASSIFIED ARBRL-CR-00508 DAAK11-81-K-0005 F/G 17/8

F/G 17/8

NL





MICROCOPY RESOLUTION TEST CHART  
NATIONAL BUREAU OF STANDARDS 1963-A

DA 126675

(12)  
AD-F300220

AD

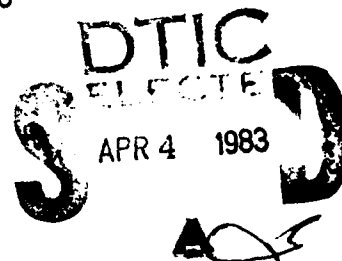
CONTRACT REPORT ARBRL-CR-00508

IMAGING SENSOR DEVELOPMENT FOR  
SCATTERING ATMOSPHERES

Prepared by

Environmental Research Institute of Michigan  
Radar and Optics Department, P.O. Box 8618  
Ann Arbor, MI 48107

March 1983



US ARMY ARMAMENT RESEARCH AND DEVELOPMENT COMMAND  
BALLISTIC RESEARCH LABORATORY  
ABERDEEN PROVING GROUND, MARYLAND

Approved for public release; distribution unlimited.

DTIC FILE COPY

Destroy this report when it is no longer needed.  
Do not return it to the originator.

Additional copies of this report may be obtained  
from the National Technical Information Service,  
U. S. Department of Commerce, Springfield, Virginia  
22161.

The findings in this report are not to be construed as  
an official Department of the Army position, unless  
so designated by other authorized documents.

*The use of trade names or manufacturers' names in this report  
does not constitute endorsement of any commercial product.*

UNCLASSIFIED

SECURITY CLASSIFICATION OF THIS PAGE (When Data Entered)

REPORT DOCUMENTATION PAGE		READ INSTRUCTIONS BEFORE COMPLETING FORM
1 REPORT NUMBER	2 GOVT ACCESSION NO.	3 RECIPIENT'S CATALOG NUMBER
CONTRACT REPORT ARBRL-CR-00508 AD-A124 675		
4 TITLE (and Subtitle)		5 TYPE OF REPORT & PERIOD COVERED
IMAGING SENSOR DEVELOPMENT FOR SCATTERING ATMOSPHERES		Final Technical Report June 1, 1981-June 1, 1982
		6 PERFORMING ORG REPORT NUMBER
		755600-3-F
7 AUTHOR(s)		8 CONTRACT OR GRANT NUMBER(s)
Anthony H. Tai		DAAK11-81-K-0005
9 PERFORMING ORGANIZATION NAME AND ADDRESS		10 PROGRAM ELEMENT, PROJECT TASK AREA & WORK UNIT NUMBERS
Environmental Research Institute of Michigan Radar and Optics Department, P.O. Box 8618 Ann Arbor, MI 48107		1L151101A91A
11 CONTROLLING OFFICE NAME AND ADDRESS		12 REPORT DATE
US Army Armament Research & Development Command US Army Ballistic Research Laboratory (DRDAR-BLA-S) Aberdeen Proving Ground, MD 21005		March 1983
14 MONITORING AGENCY NAME AND ADDRESS (if different from Controlling Office)		13 NUMBER OF PAGES
		114
		15 SECURITY CLASS (of this report)
		UNCLASSIFIED
		15a DECLASSIFICATION/DOWNGRADING SCHEDULE
16 DISTRIBUTION STATEMENT (of this Report)		
Approved for public release; distribution unlimited.		
17 DISTRIBUTION STATEMENT (of the abstract entered in Block 20, if different from Report)		
18 SUPPLEMENTARY NOTES		
19 KEY WORDS (Continue on reverse side if necessary and identify by block number)		
Scattering media                      Holography Image processing                      Interferometry Contrast enhancement                  Digital processing		
20 ABSTRACT (Continue on reverse side if necessary and identify by block number)		
Several approaches are studied to determine their effectiveness in ex- tracting a low contrast target image from a nonuniform background bias. The approaches are chosen for their potential of being implemented in a real-time imaging system. Novel techniques for combining the advantages of interferometry and digital processing are introduced. A real-time sensor system concept is proposed.		

DD FORM 1473 EDITION OF 1 NOV 65 IS OBSOLETE  
1 JAN 73

UNCLASSIFIED

SECURITY CLASSIFICATION OF THIS PAGE (When Data Entered)

## PREFACE

The work reported here was performed in the Electro-Optics Department of the Infrared and Optics Division of the Environmental Research Institute of Michigan (ERIM). This work was sponsored by the Army ARRADCOM under Contract DAAK11-81-K-0005.

This report covered work performed between June 1, 1981, and June 1, 1982. The contract monitor was Charles Stumpf of the Ballistic Research Laboratory. The principal investigator was Anthony M. Tai. Major contributions to the efforts were Anthony M. Tai, Jack Cederquist, Jim Abshier, Kim Winick and Carl C. Aleksoff.



✓	
Distribution/	
Availability Codes	
Dist. and/or	
Special	
A	100

## TABLE OF CONTENTS

List of Figures.....	7
List of Tables.....	9
1. Introduction.....	11
2. Analog and Hybrid Techniques.....	13
2.1 Defocus-Subtract	13
2.2 High Pass Filtering	23
2.3 Interferometric Techniques	25
2.4 Experimental Comparison	39
2.5 SNR Performance Comparison	46
3. Digital Technique.....	62
3.1 Processing Incoherent Images	63
3.2 Processing Coherent Images	69
4. Photoplastic Recording.....	93
4.1 Recording Mechanism	94
5. Conclusions and Recommendations.....	106
Reference List.....	112
Distribution List.....	113

## LIST OF FIGURES

2-1.	Defocus-Subtract Process.....	14
2-2.	MTFs of Focussed and Defocussed Imaging Systems and the Defocus-Subtract Process.....	16
2-3.	Experimental Setup for Testing the Removal of Focus-Independent Background.....	17
2-4.	Image of Four Bars on a Nonuniform Bias that Is Independent of Focussing Condition.....	19
2-5.	Images Processed by Subtracting Defocussed Frames...	20
2-6.	Experimental Setup for Testing the Removal of Focus-Dependent Background.....	21
2-7.	Images Processed by Subtracting Defocussed Frames for a Background Bias that Is Dependent on the Focussing Condition.....	22
2-8.	Analog Two-Dimensional High Pass Filtering.....	24
2-9.	Basic Arrangement of a Four-Grating Interferometer..	28
2-10.	Bias Subtraction with a Grating Interferometer.....	30
2-11.	Direct Implementation of an Image Grating Interferometer.....	33
2-12.	Construction and Reconstruction Geometries of a Holographic Element.....	33
2-13.	Optical Arrangement of an Imaging Grating Interferometer with On-Axis Aberration-Free Performance..	35
2-14.	Spot Diagrams for Off-Axis Image Points Obtained with Imaging Grating Interferometer Shown in Figure 2-13.....	36
2-15.	A Wide Field Imaging Grating Interferometer.....	37
2-16.	Output Beam Positions for Upper and Lower Beams of a Grating Interferometer for a Field Angle of $1.5^\circ$ .	38
2-17.	Calibration Curve for Piezoelectric Translator Used in Experiment.....	40
2-18.	Experimental Setup for Comparing Background Bias Removal Techniques.....	41
2-19.	Experimental Comparison of Background Bias Removal Techniques.....	43



# LIST OF FIGURES (Continued)

2-20. Probability Density Distributions of the Detector Output for a Dark and a Bright Area of an Incoherent Image.....	48
2-21. Probability Density Distributions of the Detector Outputs for a Dark and a Bright Area of a Speckled Image.....	54
2-22. Probability Density Distributions of a Filtered and Rectified Speckled Image.....	55
2-23. Probability Density Distributions of a Speckled Image Processed by the Interferometric Technique....	56
2-24. Probability Density Distribution of Image Processed by Interferometric Technique After Rectification....	58
2-25. Computed and Measured Amount of SNR Improvement by Integrating N Frames.....	59
2-26. Improving the Image Quality of a Two-Dimensional Image by Integration.....	61
3-1. Bias Removal by Sliding Pedestal and Rolling Ball Processing Techniques.....	64
3-2. Digital Processing of Low Contrast Incoherent Image with the Rolling Ball and Defocus-Subtract Techniques.....	65
3-3. Intensity Mapping Functions Used in Figures 3-2(c), 3-2(d) and 3-2(e).....	67
3-4. Intensity Mapping Function Used in Figure 3-2(f)....	68
3-5. Illustration of High Pass and Halo Effects on Images Processed by the Rolling Ball.....	70
3-6. The Image of a Dark Object on a Bright Background Processed by the Rolling Ball.....	72
3-7. Applying the Rolling Ball to Coherent Speckle Image.....	73
3-8. Parameters Describing the Shape of the Rolling Ball.	76
3-9. Probability Density Distributions of a Biased Two-Tone Incoherent Image with Gaussian Noise.....	78
3-10. Probability Density Distributions of Two-Tone Incoherent After Being Processing by the Rolling Ball Technique.....	79
3-11. Probability Density Distribution of a Biased Two-Tone Coherent Speckle Image with Gaussian Noise.....	80
3-12. Probability Density Distributions for a Two-Tone Coherent Speckle Image After Being Processed by a Rolling Ball Covering an Area of 9 Pixels.....	82

# LIST OF FIGURES (Continued)

3-13. Probability Density Distributions for a Two-Tone Coherent Speckle Image After Being Processed by a Rolling Ball Covering an Area of 45 Pixels.....	83
3-14. Waveform Reversal Before Applying Rolling Ball.....	84
3-15. Processed Coherent Speckle Image.....	85
3-16. Probability Density Distributions for a Two-Tone Coherent Image After Being Processed by a Rolling Ball Covering an Area of 9 Pixels Using Waveform Inversion.....	86
3-17. Probability Density Distributions for a Two-Tone Coherent Image After Being Processed by a Rolling Ball Covering an Area of 45 Pixels Using Waveform Inversion.....	87
3-18. Comparison of Smoothed Outputs Obtained With and Without Waveform Inversion.....	90
4-1. Composition of a Photoplastic Recording Device.....	95
4-2. Standard Recording Procedure for Photoplastic Device.....	97
4-3. Modified Recording Procedures for Low Contrast Fringes.....	99
4-4. Experimental Setup for Testing the SNR Performances of Two Different Recording Procedures on the Photoplastic Device.....	100
4-5. SNR Performances of the Photoplastic Device Using the Normal and Modified Recording Procedures.....	101
4-6. Optical Arrangement Utilized for Simulating the Effect of Imaging through a Scattering Medium.....	103
4-7. Performances of the Photoplastic Device and Kodak 649F Plates in Imaging Low Contrast Signal.....	104
5-1. Functional Diagram of Approaches for an Imaging Sensor for Scattering Atmospheres.....	107
5-2. Multimode Sensor System for Imaging through Scattering Media.....	111

# LIST OF TABLES

3-1. Ratio of Signal to Noise Powers with Threshold Level Set to Give $P_{e0} = 0.1$ .....	88
3-2. Visibility Attenuation Coefficients (D) versus Visibility Ranges.....	92

## 1 INTRODUCTION

When imaging through an aerosol filled atmosphere, the light reflected from the target area is attenuated and a bright background is created by the scattering. These two effects together produce a sharp drop in the contrast or visibility of the target image. In our previous work, we introduced an interferometric technique [1-3] for separating the attenuated signal light emanated from the target and the background light scattered by the aerosol. The separation was achieved by discriminating between the coherence properties of the scattered and unscattered light. Basically, the coherent light reflected by the target that reaches the observer unscattered is made to interfere with itself to form stationary fringes which are recorded on a photographic plate. The light scattered by the moving aerosol, on the other hand, produces a rapidly changing interference pattern which a sufficiently long integration period will average out into a smooth background bias. In other words, the light scattered by the moving aerosol becomes incoherent over the observation time. Since the fringes recorded are contributed only by the unscattered portion of the received light field, the target image can be extracted from the background bias by simple optical high pass filtering [1, 3].

In this report, we examine means of achieving near real-time operation and explore techniques for enhancing images of incoherently illuminated targets obtained through a scattering atmosphere.

To achieve near real-time operation, a key requirement is a real time detector for detection of the two-dimensional image or fringe plane in the case of an interferometer receiver. One of several possible candidates for direct detection of received optical radiation is photoplastic recording device [4-5]. The photoplastic device is relatively simple and inexpensive when compared with other real-time spatial light modulators such as the liquid

light valve [6] and the PROM [7]. More important, its recording mechanism makes it possible to build up the signal level of the fringes by continuously replenishing the charge depleted by the background light.

The photoplastic material, however, is thermally developed and erased. While the process is much faster than photographic development, it is still far from real time. In addition, the spectral responses of current devices are limited to the visible region and their sensitivities are not very high.

Solid state detectors are generally much more sensitive than spatial light modulators, and some (e.g., HgCdTe detectors) can respond up to the 10  $\mu\text{m}$  region. Several processing schemes are examined using the video outputs of an imaging detector. Both digital and analog approaches are considered. The performance of the processing schemes are evaluated in terms of SNR and the effectiveness in removing the background bias.

In Section 2, analog and hybrid techniques are first examined. They include high pass filtering, the use of defocussing and low pass filtering to simulate the background light distribution, and a novel interferometric approach for imaging targets that are coherently illuminated. A digital processing scheme for estimating the background distribution and subtracting it from the image scene is then presented in Section 3. Its application for both incoherent and coherent (speckled) images is demonstrated. The algorithm is very amiable to parallel processing implementation, making it possible to process images in real time. In Section 4, the use of the photoplastic recording device with a grating interferometer is presented. The unique properties of the photoplastic device and their applications for imaging low contrast coherent images are emphasized. Some of the drawbacks of the photoplastic device are also discussed.

Finally, the characteristics of the various approaches are summarized and their usefulness assessed. Based on the evaluation, an integrated sensor system for imaging through scattering media is proposed.

## 2 ANALOG AND HYBRID TECHNIQUES

To enhance the visibility of an image obtained through a scattering medium, the background light that is obscuring the desired target image must first be removed. If the background light distribution is uniform, such as those often encountered when imaging through fog, the bias can be removed simply by lowering the dc level of the detector outputs. In many situations, however, the background is non-uniform due to differences in the density of the scatterers and the lighting conditions. For such images, simply lowering the dc level of the detector output cannot adequately enhance the visibility of the target image, and a more elaborate processing technique is necessary. This is particularly true when imaging through smoke and other man-made obscurants. One possible approach to the problem is to determine the intensity distribution of the background and subtract it from the image scene. In this section, we examine some analog means for estimating and removing the background bias.

### 2.1 DEFOCUS-SUBTRACT

The image field of a focussed image may be described as  $B(x, y) + [A(x, y) + g(x, y)]$  where  $B(x, y)$  is the background added to the target image  $[A(x, y) + g(x, y)]$ .  $A(x, y)$  represents the average values of the target image which varies slowly across the image field, and  $g(x, y)$  is the portion of the image that fluctuates rapidly as illustrated in Figure 2-1(a). When properly defocussed, the high frequency information of the image is lost, and we obtain an intensity distribution that is approximately equal to  $B(x, y) + A(x, y)$  as shown in Figure 2-1(c). Subtracting the defocussed images in Figure 2-1(c) from the focussed image in Figure 2-1(b), what remains is the high frequency portion of the target image  $g(x, y)$ . As shown in Figure 2-1(d), the subtracted output is bipolar. A video monitor,

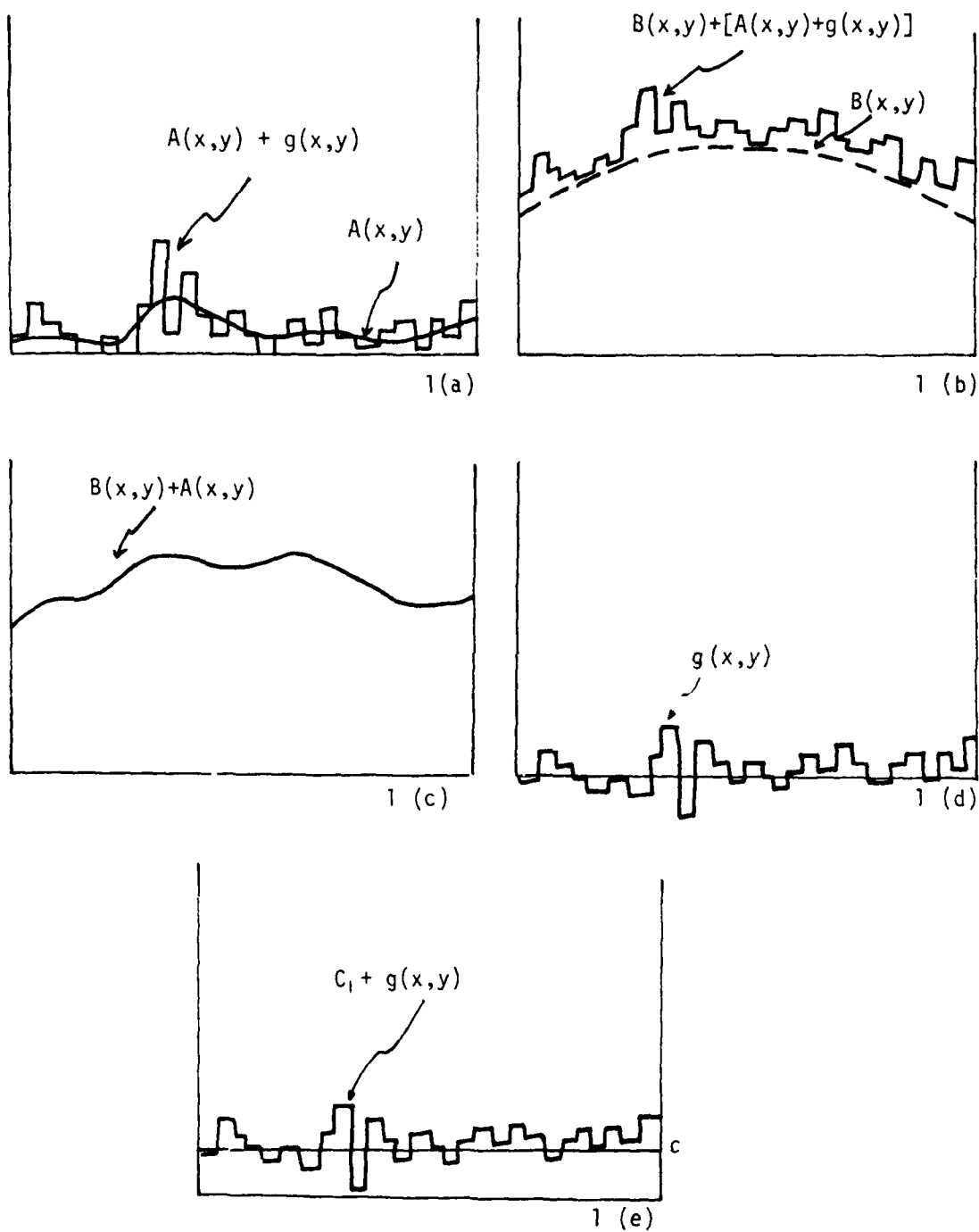


Figure 2-1. Defocus-Subtract Process.

however, displays only image intensity which must be positive in value. A constant bias equalling the largest negative value in  $g(x, y)$  is then added to make the output to the monitor positive over the entire frame as shown in Figure 2-1(e).

The process can also be described in the spatial frequency domain. The image spectrum is weighted by the modulation transfer function (MTF) of the imaging system. The MTF of a focussed and defocussed imaging system are represented by the curves C and D in Figure 2-2(a). If we subtract a defocussed image from a focussed one, the resulting MTF in the final image is effectively the difference between C and D, as represented by E in Figure 2-2(b). The defocus-subtract procedure is therefore essentially a two-dimensional high pass filtering operation. The shaded area indicates the amount of image information that may be lost in the process. This loss in low frequency information can be reduced by increasing the amount of defocussing as illustrated in Figure 2-2(c) and (d). However, the maximum amount of defocussing that can be used is limited by the changes in the background pattern that may occur when the system is defocussed. To study this effect, a set of experiments was performed utilizing the defocus-subtract technique.

Parts of the background variations are caused by shading and pattern noise in the detector. This type of background pattern is independent of the focussing condition. On the other hand, forward scattered light and nonuniform illumination patterns exist at the object plane. The background distribution they create varies with the focussing condition of the imaging system. To separate these two types of background, a focus-independent background was first created by illuminating the imaging detector with a nonuniform pattern from the side as illustrated in Figure 2-3. The input object was composed of four light bars of different widths. In

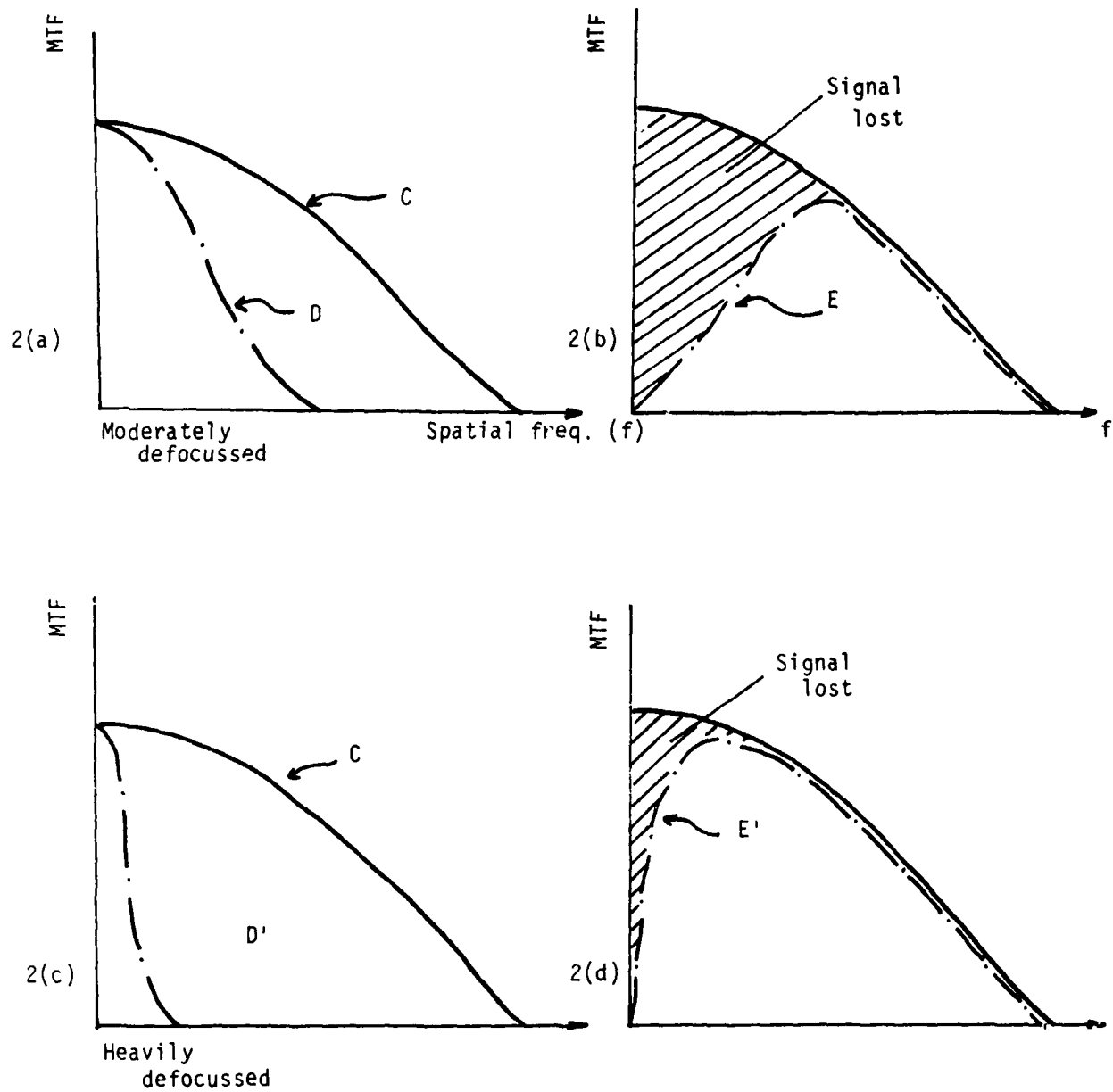


Figure 2-2. MTFs of Focussed and Defocussed Imaging Systems and the Defocus-Subtract Process.



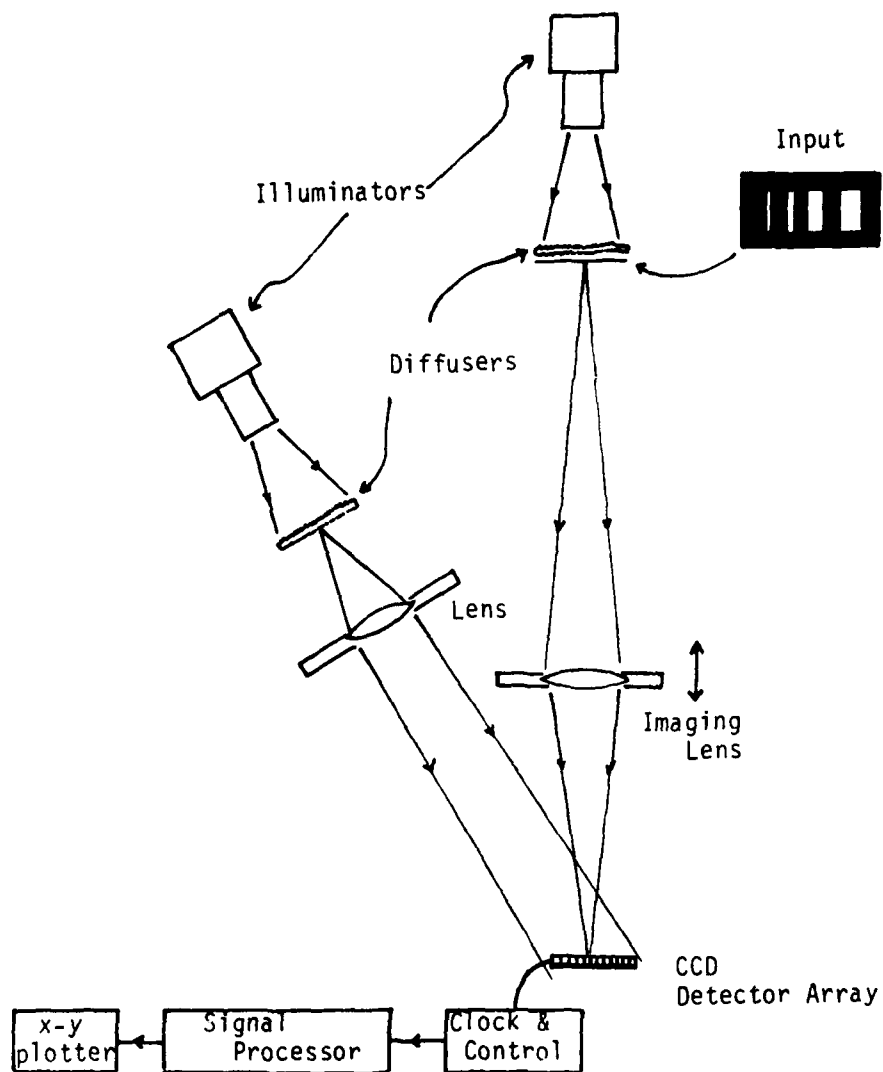


Figure 2-3. Experimental Setup for Testing the Removal of Focus-Independent Background.

Figure 2-4(a), we show the output of the imaging detector,  $B(x) + [A(x) + g(x)]$ , which is the sum of the target image and the background bias. Ideally, the added background is subtracted out to give the desired object image  $[A(x) + g(x)]$  as shown in Figure 2-4(b).

The image in the second frame was slightly defocussed and then subtracted from the original image in the first frame. As shown in Figure 2-5(a), a substantial amount of low frequency information is lost in the process. The images of the two widest bars are severely distorted. The amount of defocussing was then increased, and the results are shown in Figure 2-5(b). The image quality of the second widest bar is improved, but the widest bar is still quite distorted. The amount of defocussing was increased further as shown in Figure 2-5(c). All the bars are now resolved without noticeable distortion.

Thus, as indicated earlier in Figure 2-2, the amount of image information lost is minimized by heavily defocussing the second frame. However, if the background pattern originates at the object plane, heavily defocussing the image can alter the background distribution so much that the background can no longer be properly removed. To illustrate this characteristic, the experiment was re-set up as depicted in Figure 2-6. A nonuniform background was superimposed on the target at the object plane. In Figure 2-7(a), we show the detector output with the added background. The desired target image after removing the background is shown in Figure 2-7(b). The defocus-subtract technique was then used to remove the background light pattern. The imaging system was first defocussed slightly in the second frame as shown at the top of Figure 2-7(c). The processed image is shown in the bottom of Figure 2-7(c), and we can see that even though most of the background pattern was removed, the images of the low frequency bar pattern were severely distorted. The amount of defocussing was then increased. As shown in Figure 2-7(d), the image quality was improved, but the defocus-subtract process was



Figure 2-4. Image of Four Bars on a Nonuniform Bias That is Independent of Focussing Condition.

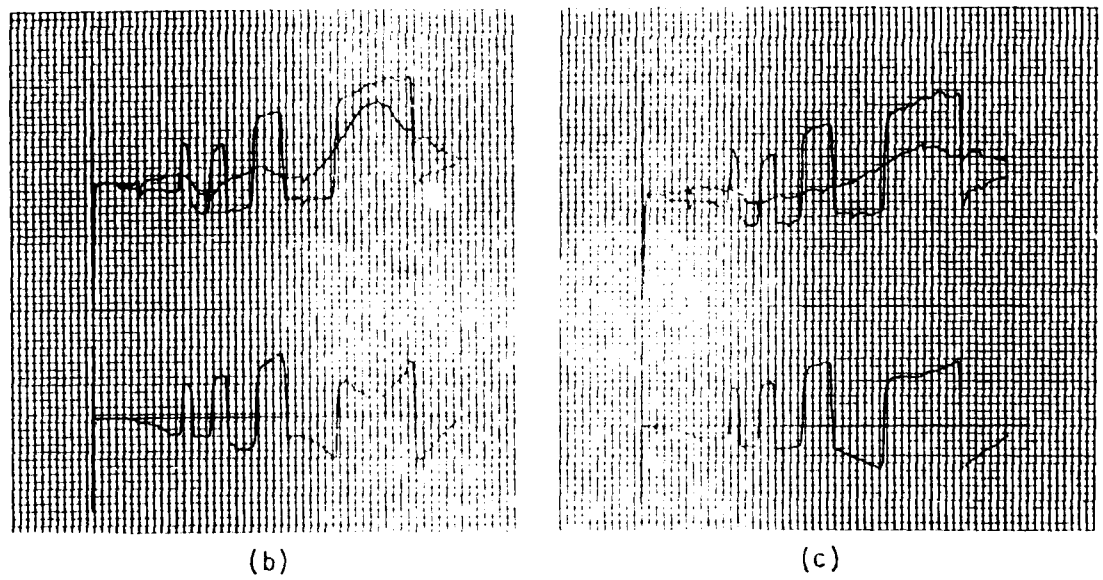
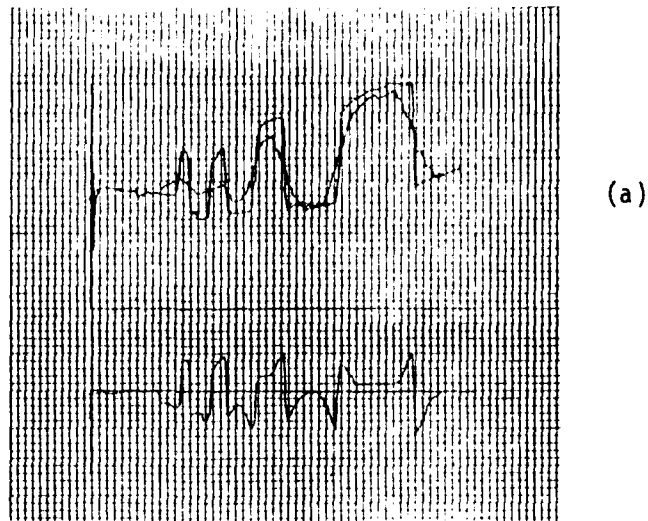


Figure 2-5. Images Processed by Subtracting Defocused Frames.

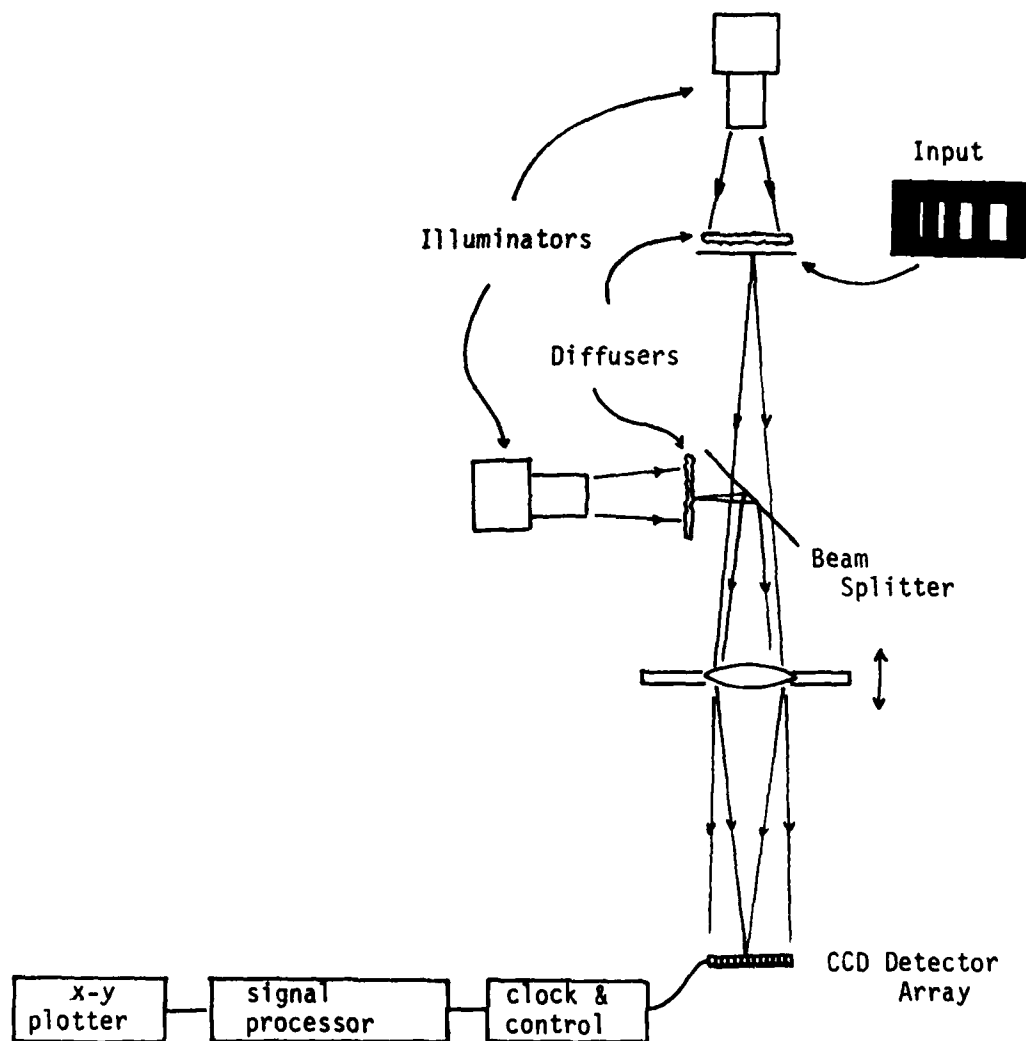


Figure 2-6. Experimental Setup for Testing the Removal of Focus-Dependent Background.

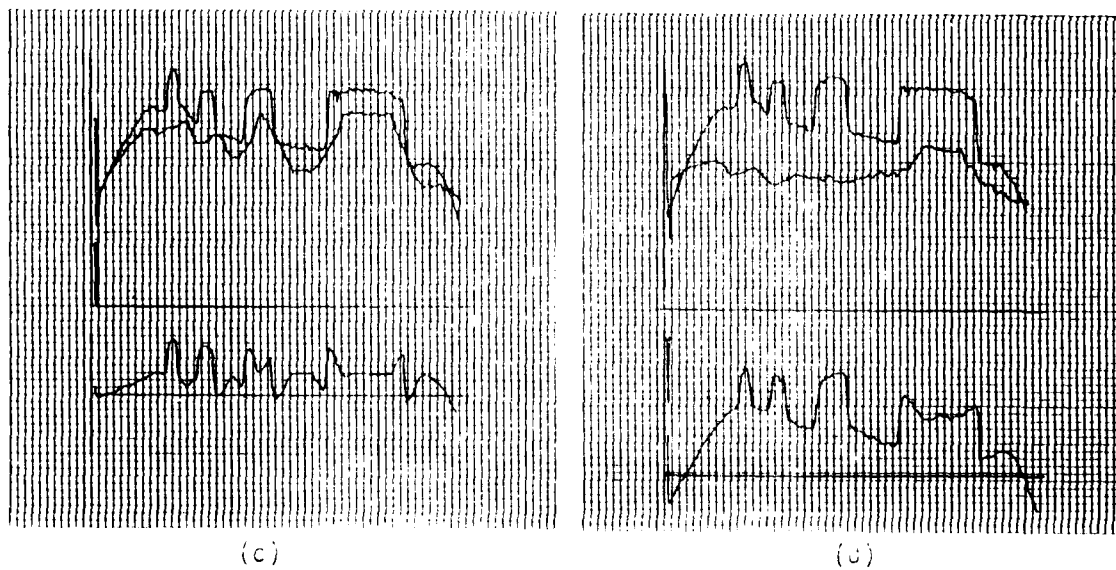
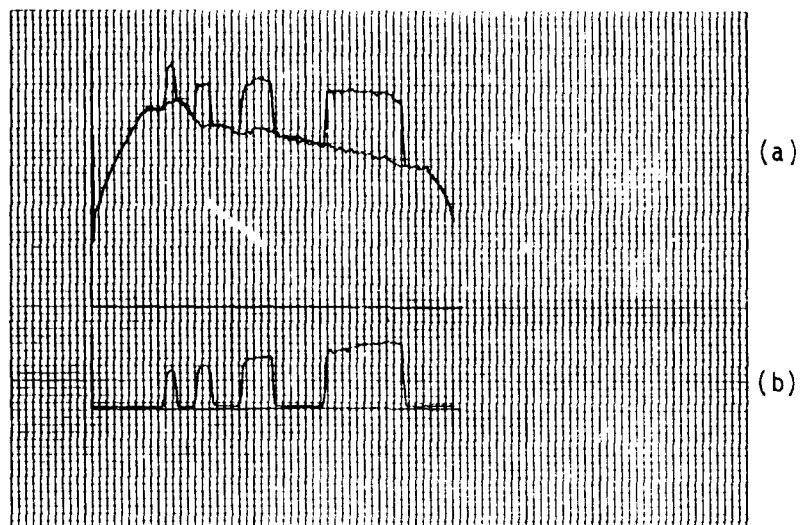


Figure 2-7. Images Processed by Subtracting Defocussed Frames for a Background Bias That is Dependent on the Focussing Condition.

unable to remove much of the background. The change in the focussing condition had caused the background distribution to vary significantly between the two frames.

The defocus-subtract processing technique is very effective in eliminating background patterns which are independent of the focusing condition of the imaging system such as detector shading and pattern noise. For backgrounds that are present in the object field, such as those due to the forward scattered light or nonuniform illumination pattern, the effectiveness in removing the background has to be traded off with the retention of low frequency image formation. The need to mechanically defocus the imaging system slows the process down. It may be difficult to implement the process at or near the TV frame rate. Subtracting a defocussed frame from a focussed frame also lowers the SNR because the desired image signal exists in only one frame while system noise is present in both frames. On the positive side, the defocus-subtract technique is also able to remove the detector pattern noise without the need for any additional processing. The technique is therefore particularly useful when an imaging detector with strong pattern noise is used.

## 2.2 HIGH PASS FILTERING

As pointed out earlier, the defocus-subtract technique performs essentially a high pass operation. (An equivalent operation is to low pass filter the image scene and then subtract it from the original image.) For those limited applications where one-dimensional filtering is acceptable, the system will be very simple, composing of a single electronic high pass filter. To achieve two-dimensional high pass filtering, a system similar to that depicted in Figure 2-8 may be used.

Direct high pass filtering offers several advantages. First of all, the system is relatively simple, and it does not require mechanical manipulation such as defocussing the lens. Unlike the defocus-subtract or low pass-subtract techniques, it is not necessary to

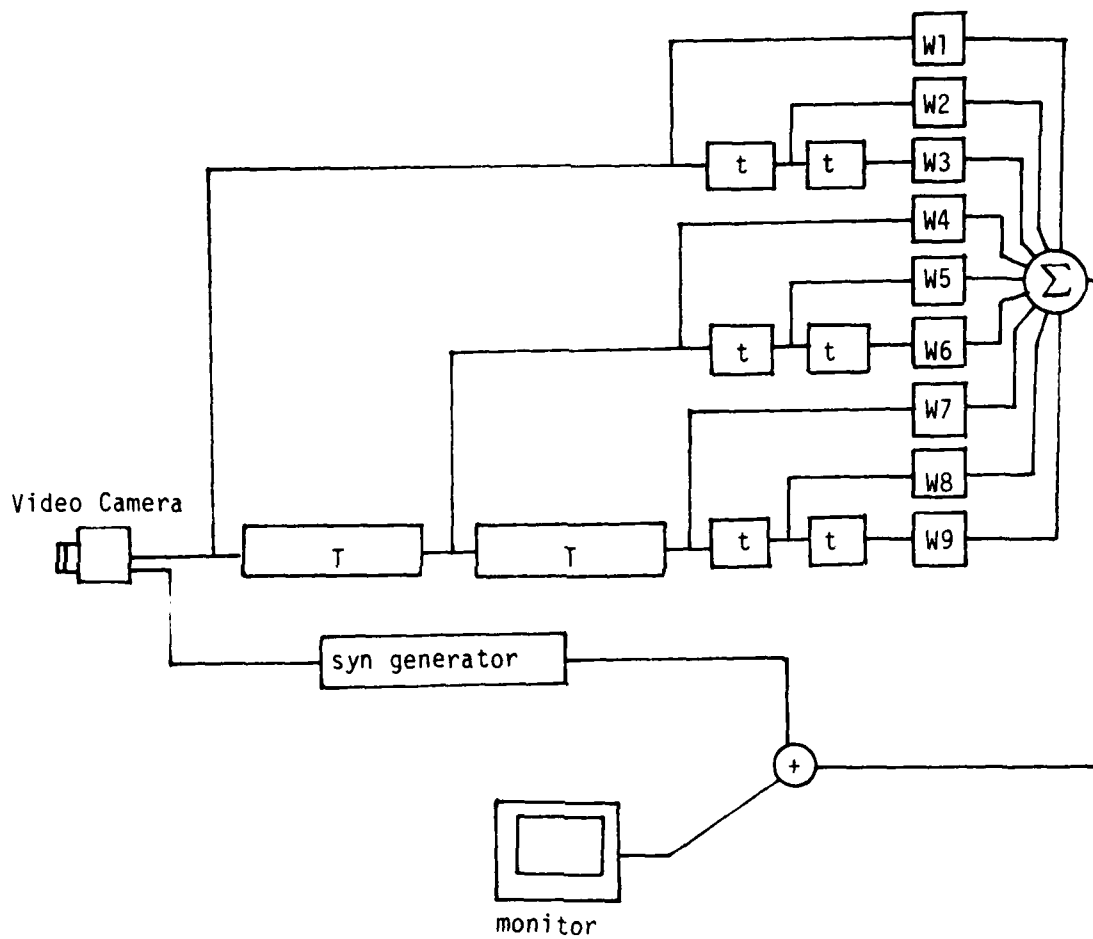


Figure 2-8. Analog Two-Dimensional High Pass Filtering.



record two frames in order to produce one processed plane. Without the use of a second frame, extra noise will not be added as with the defocus-subtract process.

To image through scattering media, solid state imaging detector arrays such as CCD cameras are generally preferable to vidicons due to their superior SNR performance. However, detector arrays exhibit pattern noise which is deterministic and cannot be removed by averaging. The defocus-subtract technique is able to remove both the background bias and the pattern noise. Direct filtering, on the other hand, tends to enhance the high frequency pattern noise. To remove the pattern noise, it is necessary to pre-store a frame consisting only of the pattern noise and subtract it from the filtered image. This can be done by uniformly illuminating the imaging detector and storing the detector output in a digital memory. However, by doing so, much of the advantages mentioned earlier are negated.

### 2.3 INTERFEROMETRIC TECHNIQUES

There are three main sources of background light: (1) forward scattered light originated from the target scene, (2) backscattered light from an active illuminating source, and (3) scattered light originated from natural light sources such as the sun. In daytime operation, scattered sunlight predominates. To reduce this source of background light, one may illuminate the target with monochromatic light and employ a narrow band spectral filter at the receiver. Since natural light sources are broadband, only a small portion of the scattered sunlight can reach the detector. Furthermore, the backscattered light from the illuminating source can be minimized by placing the illuminating beam at a large angle from the observer's line of sight. This will limit the background to mostly forward scattered light from the target scene.

If coherent monochromatic light is used to illuminate the target, one may also take advantage of the differences in the coherence properties of the scattered and unscattered light. In our earlier work, we showed that the coherent unscattered portion of the light forms stationary fringes when the received light field is made to interfere with itself. The scattered light, on the other hand, simply adds by intensity and forms a smooth background. We recorded the fringe pattern on a high resolution photographic plate and extracted the target image which was encoded by the fringe pattern using optical spatial filtering. Recording on a spatial light modulator such as photographic plate which offers very high recording resolution, the carrier frequency can be made very high to maximize the system sensitivity and SNR [1-3]. However, the pixel sizes of present day imaging detectors are much larger and the space-bandwidth product much smaller than that of spatial light modulators. To optimize the system performance, a different approach has to be taken.

The most direct means of utilizing the differences in coherence is to take advantage of the speckle effect. The coherent image of a diffuse object is characterized by speckles. When imaging through a scattering medium, the image formed by the unscattered light is encoded by a speckle pattern while the scattered light forms a smooth background. The image can therefore be easily extracted by high pass filtering. The advantage of speckle encoding is that it is independent of the object structure. The speckle statistic is determined by the transfer function of the imaging system, and it is fixed. The optimum filter bandwidth can be predetermined regardless of the spatial frequency content of the target scene. However, as mentioned earlier, detector pattern noise cannot be removed by high pass filtering. Moreover, the impulse response of a high pass filter tends to distort the processed image. We now introduce a novel technique with which the background and the pattern noise can both be completely removed without causing any distortion of the image.

Consider the four-grating interferometer shown in Figure 2-9. (Gratings 2 and 3 can be parts of the same grating.) The incoming light field is split into two and then recombined by the fourth grating such that the wavefront interferes with a slightly displaced version of itself. If we describe the light field as  $f(x, y)$ , then the output light intensity distribution becomes

$$\begin{aligned} g_1(x, y) &= |f(x, y) + f(x + \Delta x, y)|^2 \\ &= |f(x, y)|^2 + |f(x + \Delta x, y)|^2 \\ &\quad + f(x, y)f^*(x + \Delta x, y) \\ &\quad + f^*(x, y)f(x + \Delta x, y) \end{aligned} \quad (2-1)$$

Now if we translate the fourth grating by a quarter fringe, the intensity distribution changes to

$$\begin{aligned} g_2(x, y) &= \left| f(x, y) e^{i \frac{\pi}{2}} + f(x + \Delta x, y) e^{-i \frac{\pi}{2}} \right|^2 \\ &= |f(x, y)|^2 + |f(x + \Delta x, y)|^2 \\ &\quad - f(x, y)f^*(x + \Delta x, y) \\ &\quad - f^*(x, y)f(x + \Delta x, y) \end{aligned} \quad (2-2)$$

The two patterns,  $g_1$  and  $g_2$ , are more or less contrast reversed versions of each other. For example, if at  $(x_0, y_0)$ ,  $f(x_0, y_0) = f(x_0 + \Delta x, y_0)$ , then

$$g_1(x_0, y_0) = 4|f(x_0, y_0)|^2$$

while

$$g_2(x_0, y_0) = 0$$

On the other hand, if  $f(x_0, y_0) = f(x_0 + \Delta x, y_0) e^{i\pi}$ , then

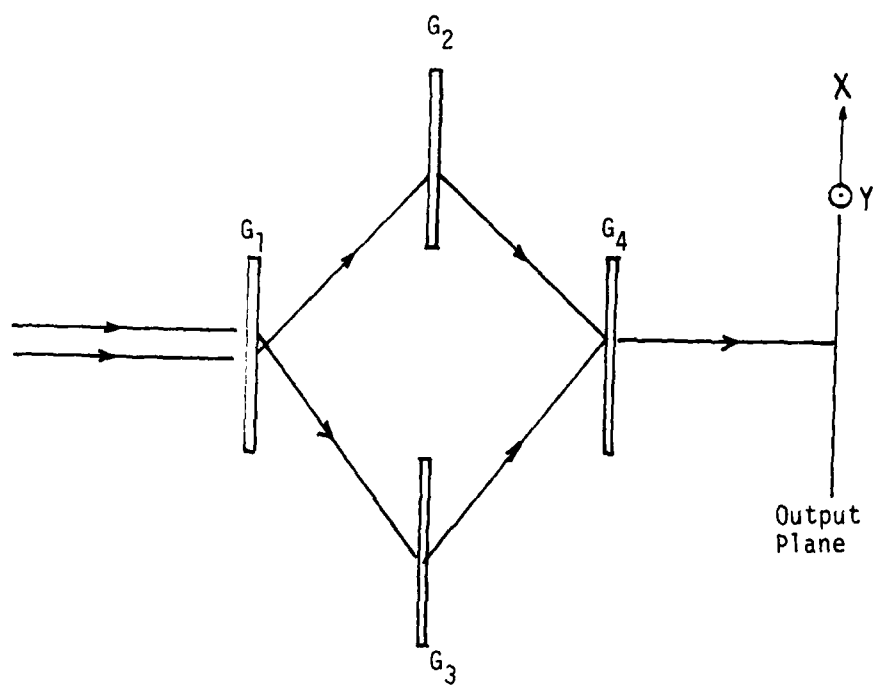


Figure 2-9. Basic Arrangement of a Four-Grating Interferometer.

$$g_1(x_0, y_0) = 0$$

and

$$g_2(x_0, y) = 4|f(x_0, y_0)|^2$$

To use the interferometer to process coherent images obtained through a scattering medium, one may first record the light distribution at the output of the interferometer and store it in a digital memory. The light distribution of the image can be written as

$$I_1(x, y) = B(x, y) + G(x, y) \quad (2-3)$$

where  $B(x, y)$  is the bias distribution and  $G(x, y)$  is a bipolar function corresponding to the spatially varying portion of the image.

The fourth grating is then translated by a quarter fringe and the light intensity distribution becomes

$$I_2(x, y) = B(x, y) - G(x, y) \quad (2-4)$$

Subtracting the second frame from the first, we have

$$I_3(x, y) = I_1(x, y) - I_2(x, y) = 2G(x, y) \quad (2-5)$$

The background bias is removed while the signal level is doubled. The process is illustrated in Figure 2-10.

We emphasize that the removal of the background is complete with this technique. The background light distribution is not simply approximated as in defocussing or low pass filtering. The incoherent background light is unaffected by the shifting grating. Its intensity distributions are identical between the two frames. The background is therefore completely removed after the subtraction. Similarly, the pattern noise in the detector output are also identical between the two frames, and they, too, are completely removed in the subtraction process. The only part of the image that remains after the subtraction is the coherent part of the image whose contrast is reversed by the shifting of the grating.

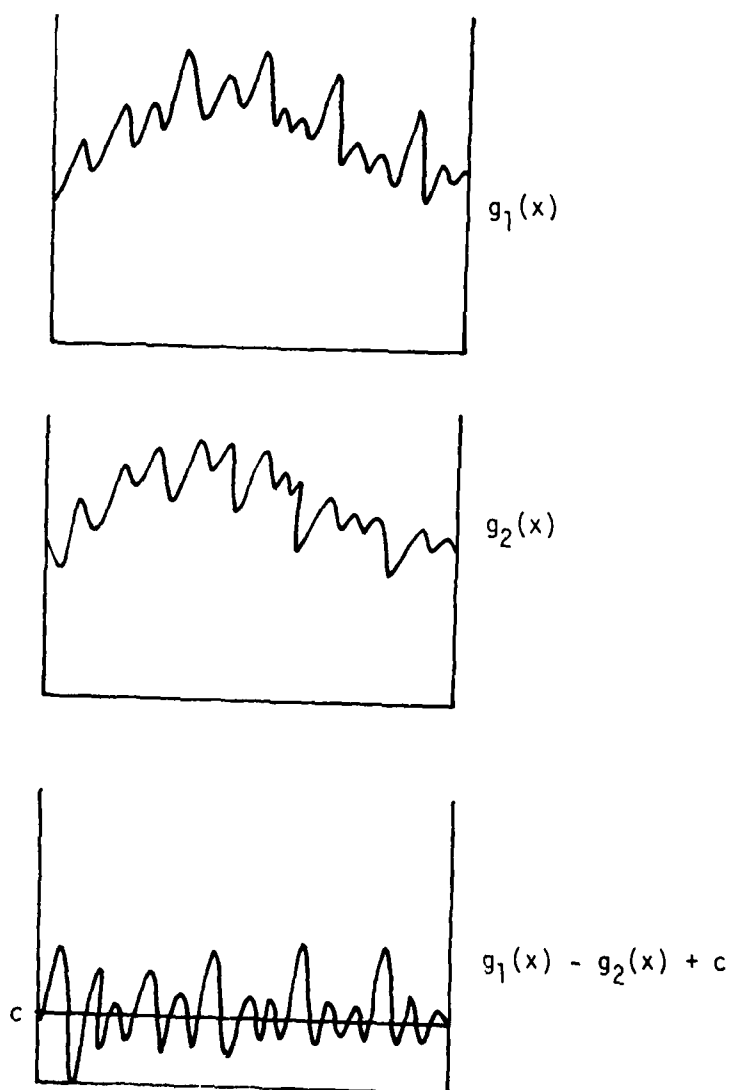


Figure 2-10. Bias Subtraction with a Grating Interferometer.

To be able to utilize this technique, the imaging detector must be able to resolve the speckles of the image. The average speckle size of a coherent image is equal to  $1.22\lambda f$  where  $\lambda$  is the wavelength of the light and  $f$  is the  $f$ /number of the imaging lens. Thus, the detector pixel size must be smaller than  $1.22\lambda f$  in order to be able to resolve the speckle pattern. A pixel size of a typical CCD detector array is about  $25 \mu\text{m}$ . With  $\lambda = 0.6 \mu\text{m}$ , the  $f$ /number of the image lens must be larger than  $f/34$ . The light collection efficiency will therefore be very low. However, operating at  $\lambda = 10.6 \mu\text{m}$ , the  $f$ /number of lens needs only be larger than  $f/1.9$  which is quite reasonable. Thus, due to the limitation of the pixel size available on current detector arrays, this interferometric technique will be more practical at the longer wavelengths (e.g., far infrared). This may not be a significant drawback since operation at FIR is often preferred in imaging through scattering media. Scattering is much less severe at the longer wavelengths, and one of the most powerful lasers available ( $\text{CO}_2$ ) operates at  $10.6 \mu\text{m}$ .

The most direct implementation of the interferometer in an imaging mode is shown in Figure 2-11. Such an arrangement, however, suffers severely from aberration. The gratings can be considered as a hologram constructed with plane waves, and the converging beam originated from an object point can be considered as the reconstructing beam. The deviation (in wavelength) of the diffracted light field was computed to be [8]

$$\Delta = \frac{1}{\lambda} \left[ -\frac{1}{8} (x^2 + y^2)S + \frac{1}{2} (x^2 + y^2)xC_x - \frac{1}{2} x^2A_x \right] \quad (2-6)$$

where

$$S = \frac{1}{R_c^3} - \left( \frac{1}{R_o^3} - \frac{1}{R_r^3} \right) - \frac{1}{R_i^3} \quad (2-7)$$

(spherical aberration)

$$C_x = \frac{\sin \alpha_c}{R_c^2} - \left( \frac{\sin \alpha_o}{R_o^2} - \frac{\sin \alpha_r}{R_r^2} \right) - \frac{\sin \alpha_i}{R_i^2} \quad (2-8)$$

(coma)

$$A_x = \frac{\sin^2 \alpha_c}{R_c} - \left( \frac{\sin^2 \alpha_o}{R_o} - \frac{\sin^2 \alpha_r}{R_r} \right) - \frac{\sin^2 \alpha_i}{R_i} \quad (2-9)$$

(astigmatic aberration)

The parameters  $R_c$ ,  $R_r$ ,  $R_o$ ,  $R_i$ ,  $\alpha_c$ ,  $\alpha_o$ ,  $\alpha_i$  and  $\alpha_r$  describe the construction and reconstruction geometry as shown in Figure 2-12. With  $R_o = R_r = \infty$ , they can be simplified to

$$S = \frac{1}{R_c^3} - \frac{1}{R_i^3} \quad (2-10)$$

$$C_x = \frac{\sin \alpha_c}{R_c^2} - \frac{\sin \alpha_i}{R_i^2} \quad (2-11)$$

and

$$A_x = \frac{\sin^2 \alpha_c}{R_c} - \frac{\sin^2 \alpha_i}{R_i} \quad (2-12)$$

Since  $R_i = R_c$ , we have  $S = 0$ ; there would not be any spherical aberration. By placing the grating perpendicular to the optical axis of the reconstructing beam,  $\alpha_c = 0$ , and we have

$$C_x = \frac{\sin \alpha_i}{R_i^2} \text{ and } A_x = \frac{\sin^2 \alpha_i}{R_i} \quad (2-13)$$

The image would therefore suffer from coma and astigmatic aberration. We can see that the aberration increases with the diffraction angle and for the geometry used in the grating interferometer, astigmatism is the more dominant aberration.



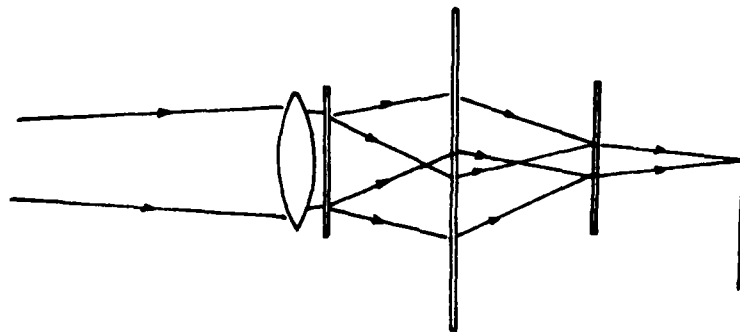


Figure 2-11. Direct Implementation of an Image Grating Interferometer.

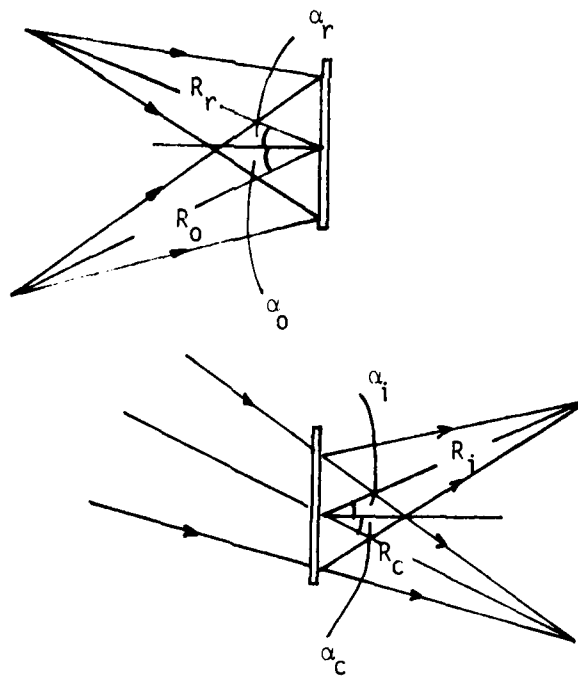


Figure 2-12. Construction and Reconstruction Geometries of a Holographic Element.

From Eq. (2-12), we also find that the astigmatic aberration can be made to vanish by making  $\alpha_c = \alpha_i$ . This can be achieved by tilting the grating an angle  $\alpha_i/2$ . The remaining coma is quite small, and it does not significantly affect the spot size. In Figure 2-13, we show one possible arrangement where the entrance and diffraction angles are equal for all the gratings in the interferometer. However,  $\alpha_c$  can be made equal to  $\alpha_i$  for only one input field angle. Thus, the system is free of astigmatism only for an on-axis image point. To analyze the severity of off-axis aberration, we utilize ERIM's Holographic Optical Analysis and Design (HOAD) ray tracing program. In Figure 2-14(a) and (b), we show the output spot diagrams for a f/5.6 imaging system at  $\pm 1.5^\circ$  field angles. We find that there are significant amount of astigmatic aberrations. The 0.049 mm and 0.064 mm RMS spot sizes are about 11.3 and 14.8 times larger than the diffraction-limited spot size (at  $\lambda = 0.6328\text{\AA}$ ).

Going back to Eqs. (2-11) and (2-12), we see that both coma and astigmatic aberration vanish if  $R_c = R_i = \infty$ . In other words, a wavefront will be diffracted unaberrated for all angles by a plane grating if it is a plane wave. Thus, to assure aberration-free performance over a wide field of view, the wavefronts propagating inside the interferometer must be plane waves. This is achieved by the arrangement illustrated in Figure 2-15. We may note that for distance object, the light field entering the interferometer is approximately a superposition of plane waves, and the collimator at the front end can be eliminated.

Another question that arises is whether the upper and lower beams maintain registration for off-axis field angles. In Figure 2-16, we show the computed ray positions at the output plane for the upper and lower beams with an input field angle of  $1.5^\circ$ . We see that the beams remain in excellent registration.

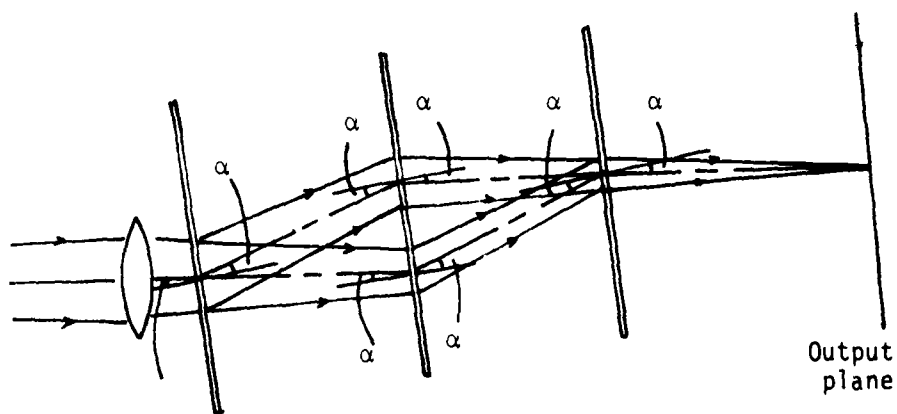
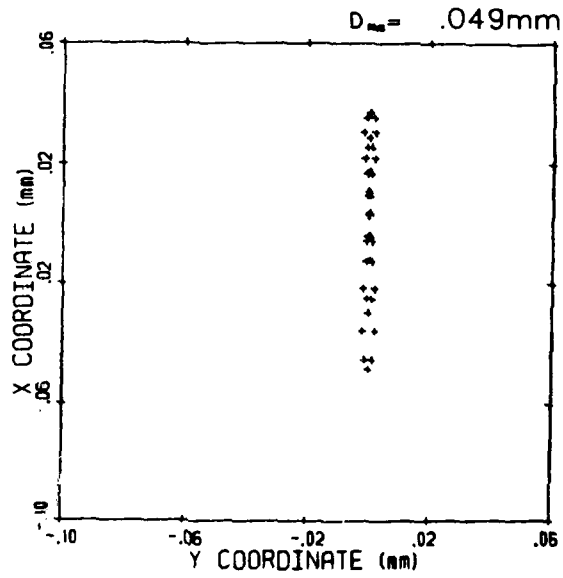


Figure 2-13. Optical Arrangement of an Imaging Grating Interferometer With On-Axis Aberration-Free Performance.

# SPOT DIAGRAM

field angle  
+ 15°



field angle  
- 15°

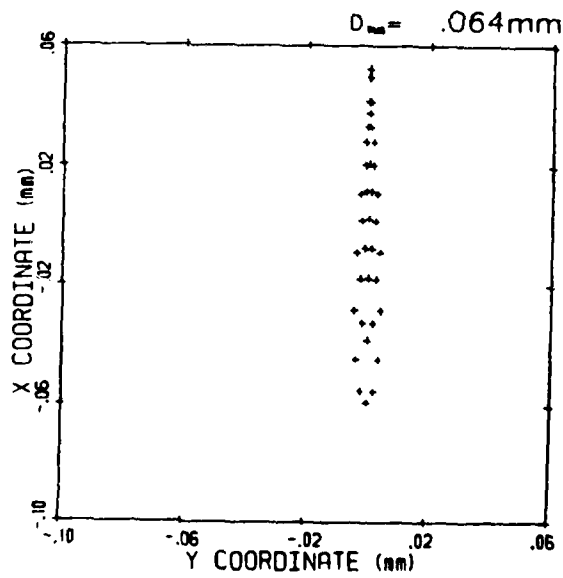


Figure 2-14. Spot Diagrams for Off-Axis Image Points Obtained with Imaging Grating Interferometer Shown in Figure 2-13.

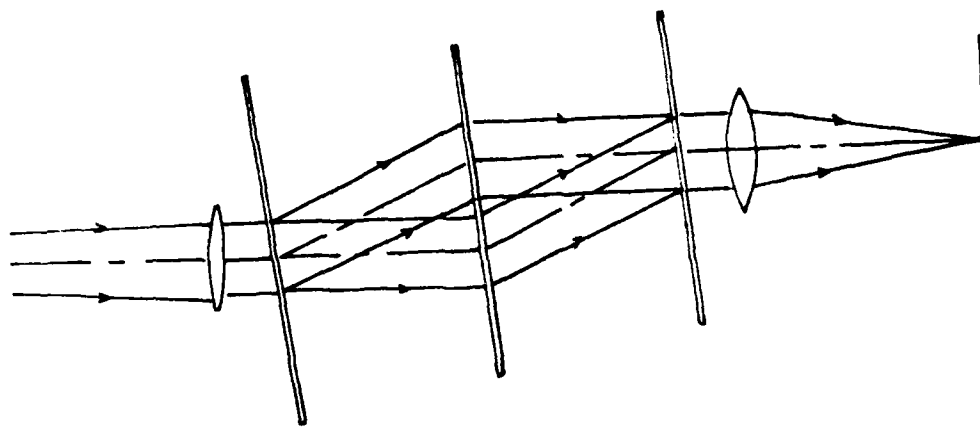
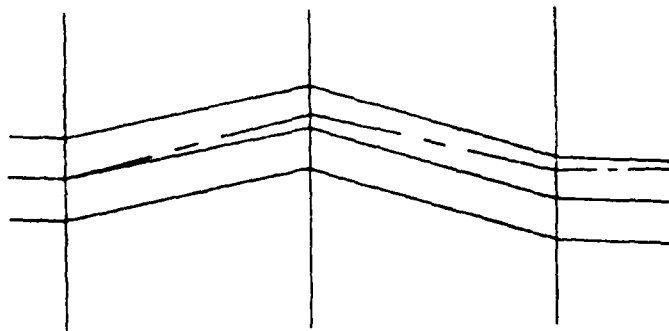


Figure 2-15. A Wide Field Imaging Grating Interferometer.

T01	RAY	X	Y	Z
T01	1	7.53518E-03	0.0	0.0
T01	2	-2.99648E-02	0.0	0.0
T01	3	-6.74648E-02	0.0	0.0



T01	RAY	X	Y	Z
T01	1	7.53518E-03	0.0	0.0
T01	2	-2.99648E-02	0.0	0.0
T01	3	-6.74648E-02	0.0	0.0

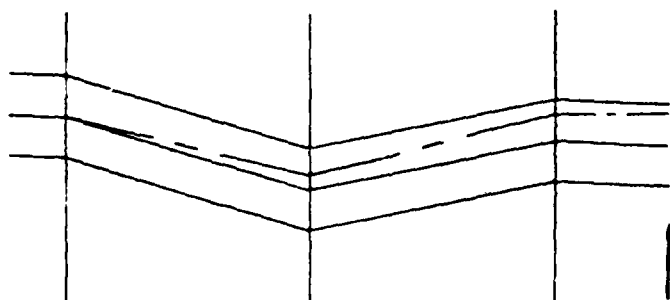


Figure 2-16. Output Beam Positions for Upper and Lower Beams of a Grating Interferometer for a Field Angle of 1.5°.

This interferometric technique also requires mechanical manipulation, namely, the shifting of the grating by a quarter fringe. However, the amount of movement required is very small, especially when compared with the amount needed for defocussing. For example, if the spatial frequency of the fourth grating is 1000 lines/mm, then the amount of movement required is only 0.25  $\mu\text{m}$ . Such fine resolution translation can be achieved with a translator drive by a piezoelectric crystal. The Jodon piezoelectric translator we used can provide a translation resolution better than 0.03  $\mu\text{m}$  as shown by the calibration curve in Figure 2-17.

Since the amount of movement required to produce the phase shifts is so small, it is possible for the system to keep up with the T.V. frame rate.

#### 2.4 EXPERIMENTAL COMPARISON

The three techniques were experimentally compared on their effectiveness in removing the background bias and pattern noise. An expanded laser beam was used to illuminate a rotatable ground glass. The light scattered by the ground glass diffuser was then used as the object beam to illuminate a slit which was backed by another ground glass diffuser. The laser beam was expanded sufficiently such that the objective speckles formed on the object surface would be too small to be resolved by the imaging lens. With this arrangement, incoherent and coherent illuminations of equal intensity can be obtained by either rotating the diffuser or letting it remain stationary. A grating interferometer was placed between the imaging lens and the imaging detector as shown in Figure 2-18. All the images were obtained through the interferometer even though the property of the grating interferometer was actually used only in the implementation of the interferometric scheme. This was done to assure that the recording conditions were the same in the implementation of the different schemes. A background bias was added by illuminating the imaging detector from the side with a microscope illuminator.

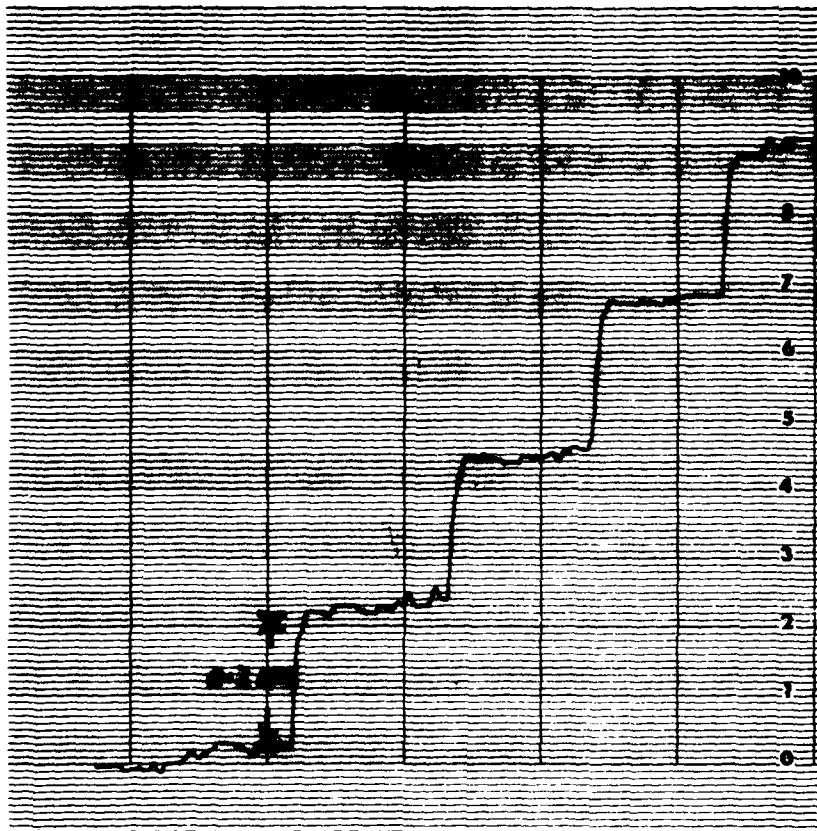


Figure 2-17. Calibration Curve for Piezoelectric Translator Used in Experiment.



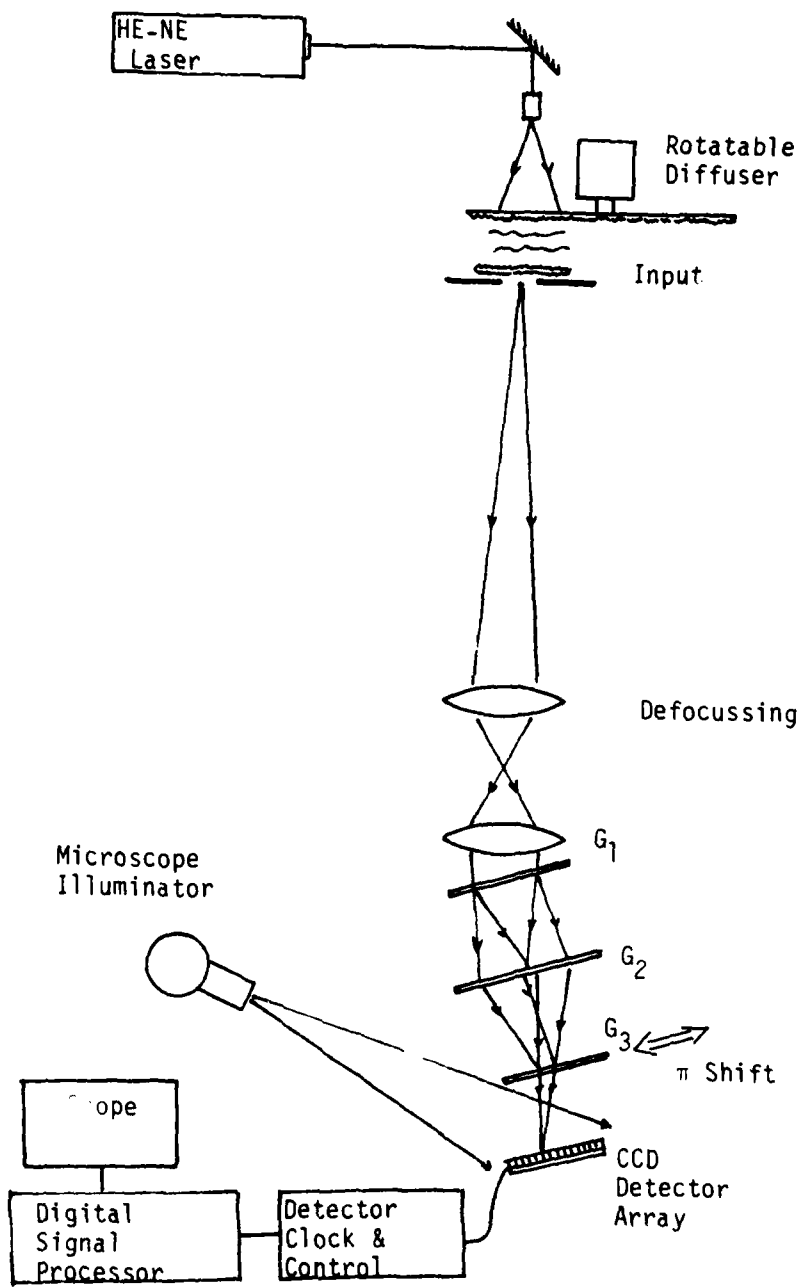


Figure 2-18. Experimental Setup for Comparing Background Bias Removal Techniques.

The main purpose of this experiment is to examine the effectiveness of the various techniques in removing the nonuniform background, including that due to detector shading and pattern noise. To make it easier to examine the results, 100 frames were integrated to produce images with high signal-to-noise ratios.

The image of an input slit under incoherent illumination is shown in Figure 2-19(a), and the image with the added background is shown in Figure 2-19(b). First, we implemented the incoherent-defocus-subtract technique, and the result is shown in Figure 2-19(c). The process effectively removed both the background and the irregularities due to pattern noise. However, a significant amount of low frequency information was lost. (See Section 2.1.) Since the defocus-subtract technique performs essentially a high-pass filtering operation, for comparison, we performed the high-pass filtering directly with an analog filter ( $-3$  dB bandwidth  $1\text{K} > 200$  kHz where 200 kHz is the full bandwidth of the detector output). In Figure 2-19(d), we show the filtered image. The background is removed, but the high-frequency pattern noise remained. To eliminate also the pattern noise, we illuminated the detector uniformly and we high-pass filtered the detector output and then stored the filtered image in a digital memory. We should emphasize that this procedure has to be performed only once at the beginning. In Figure 2-19(e), we show the result after the pre-stored pattern noise was subtracted from the high-pass output. As expected, the result is similar to that obtained with the defocus-subtract technique. The high-passed output shows more ringing at the edge because the filter cut-off was sharper in the analog filter than in the effective filter of the defocus-subtract process.

The drawback of both the defocus-subtract and high-pass technique is that a substantial amount of low frequency image information may be lost in the processing. One approach to the problem is to encode the image with a high-frequency pattern. The speckle pattern offers

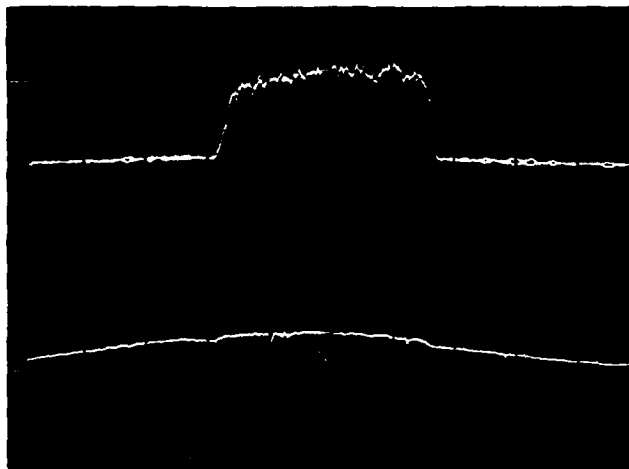


Figure 2-19 (a).  
Input.

Figure 2-19 (b).  
Input on  
Nonuniform  
Bias (1/16 Scale).

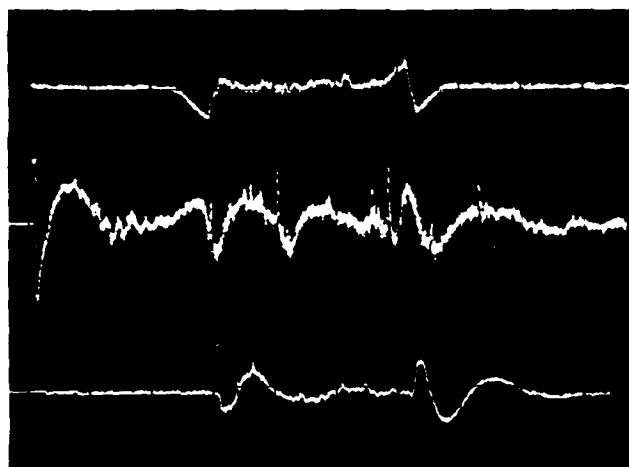


Figure 2-19 (c).  
Incoherent-  
Defocus-Subtract.

Figure 2-19 (d).  
Incoherent-  
High Pass.

Figure 2-19 (e).  
Incoherent-  
High Pass-  
Subtract  
Pattern Noise.

Figure 2-19. Experimental Comparison of Background Bias Removal Techniques.

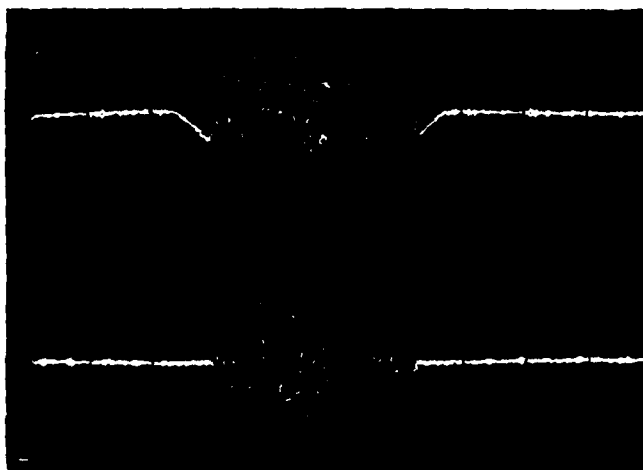


Figure 2-19 (f).  
Coherent-  
Scan Grating-  
Defocus-Subtract.

Figure 2-19 (g).  
Coherent-  
 $\pi$  Phase Shift-  
Subtract.

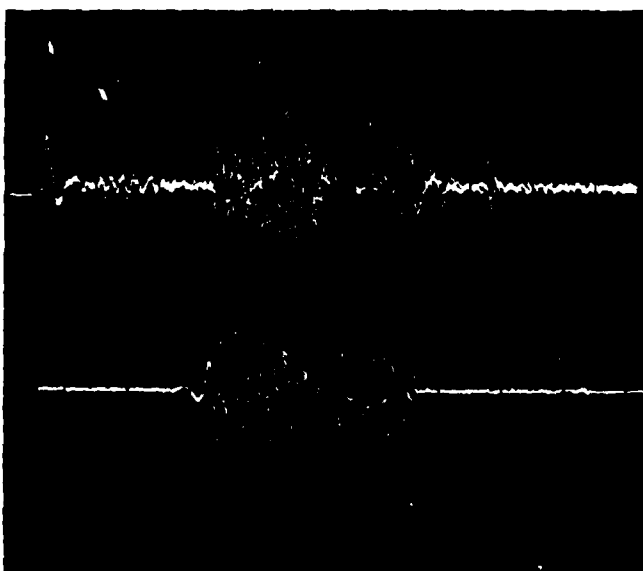


Figure 2-19 (h).  
Coherent-  
High Pass.

Figure 2-19 (i).  
Coherent-  
High Pass-  
Subtract  
Pattern Noise.

Figure 2-19. Experimental Comparison of Background Bias Removal Techniques  
(Continued).

a natural means of encoding the image. In Figure 2-19(f), we show the processed output using the defocus-subtract technique for an object under coherent illumination. We note that the coherent image is speckled regardless of the focussing condition. To obtain the background bias, besides defocussing the image, the grating was also scanned during the exposure. Scanning the grating produced a time-varying speckle pattern that averaged out during the integration period of the detector. As we can see from Figure 2-19(f), with the speckle encoding, the processed image does not suffer from a loss in signal level as in Figure 2-19(c) where incoherent illumination was used.

A more efficient processing technique is to subtract two frames where the speckle contrast is reversed. The common background will be subtracted out while the amplitude of the speckled image will double. The speckle contrast reversal was implemented by shifting the position of grating  $G_3$  in Figure 2-18 by a quarter fringe. This caused a  $\pm\pi/2$  phase shift in the interfering images resulting in a reversal of speckle contrast. The result obtained with this technique is shown in Figure 2-19(g). Both the background bias and pattern noise were completely removed, and, comparing Figure 2-19(g) with Figure 2-19(f), we see that the peak signal amplitude in the image obtained with the  $\pi$  shift-subtract technique is approximately twice as high as that obtained with the defocus-subtract process.

Finally, we implemented high-pass filtering with the coherent image (-3 dB bandwidth, 5K to 200 kHz), and the result is shown in Figure 2-19(h). Once again, the background bias was removed, but the pattern noise remained. In Figure 2-19(i), we show the output after the pre-stored pattern noise was subtracted from the filtered image.

The operations of the defocus-subtract and high-pass filtering are functionally similar. However, the defocus-subtract process is able to eliminate detector pattern noise while high-pass filtering

permits true real-time operation. Both techniques are sensitive to the spatial frequency contents of the target image. The loss of low-frequency image information can be avoided with the using of speckle encoding provided that coherent illumination of the target is allowed. If coherent illumination is used, the grating interferometric technique is the most effective. With only the image speckles changed between frames, a complete removal of the background noise and pattern noise is achieved.

All these analog techniques for finding the background bias resulted in an output that is bipolar because they do not differentiate between the added background and the average values of the object image itself. Before the image can be displayed, the processed output must be made all positive by adding a bias or rectifying the output. If there are large variations in amplitudes within the processed output, adding the bias will once again obscure small signals. Moreover, adding a bias makes it difficult to apply SNR enhancement techniques such as thresholding. Rectification cannot be applied at all for incoherent images since it greatly distorts the images. In a later section, we shall introduce a digital approach called the "rolling ball." The digital technique can be applied directly to remove the background of both coherent and incoherent images, and it can also be used to post-process the image processed by the techniques described in this section. In addition, we shall show that by taking advantage of the statistical properties of speckles, the SNR of an image obscured by a nonuniform background bias can be further enhanced.

## 2.5 SNR PERFORMANCE COMPARISON

When imaging through a scattering medium, the output of the imaging detector can be written as

$$I_0 = S(t) + B(t) + N(t) \quad (2-14)$$

where  $S(t)$  is the signal due to the unscattered portion of the light,  $B(t)$  is the background bias caused by the scattering and  $N(t)$  is the system noise. In the previous section, we described different ways with which the bias term may be estimated and subtracted out. The signal, however, is still buried in random system noise.

For simplicity, we shall assume that the input is a two-tone object with a 100% contrast. Ideally, after bias subtraction the output becomes  $I_0(t) = S(t) + N(t)$ . For most detectors, the output noise characteristic can be approximated to be Gaussian distributed. Thus, the dark area of the output will have a probability density distribution of

$$f_0(I'_0) = \frac{1}{\sqrt{2\pi\sigma^2}} e^{-I'^2_0 / 2\sigma^2} \quad (2-15)$$

and for the bright area,

$$f_1(I'_0) = \frac{1}{\sqrt{2\pi\sigma^2}} e^{-(I'_0 - A)^2 / 2\sigma^2} \quad (2-16)$$

where  $\sigma^2$  is the noise variance, zero and  $A$  are the mean output values for the dark and bright areas, respectively, as shown in Figure 2-20. If we choose a threshold level of  $T$ , then the probability that we have a signal output at a dark area is

$$P_{e0} = \int_T^\infty f_0(I'_0) dI'_0 \quad (2-17)$$

and the probability that we have no output signal at a bright area is

$$P_{e1} = \int_{-\infty}^T f_1(I'_0) dI'_0 \quad (2-18)$$

If we choose the threshold too low,  $P_{e0}$  will be large and the output becomes noisy. If the threshold is set too high, then  $P_{e1}$

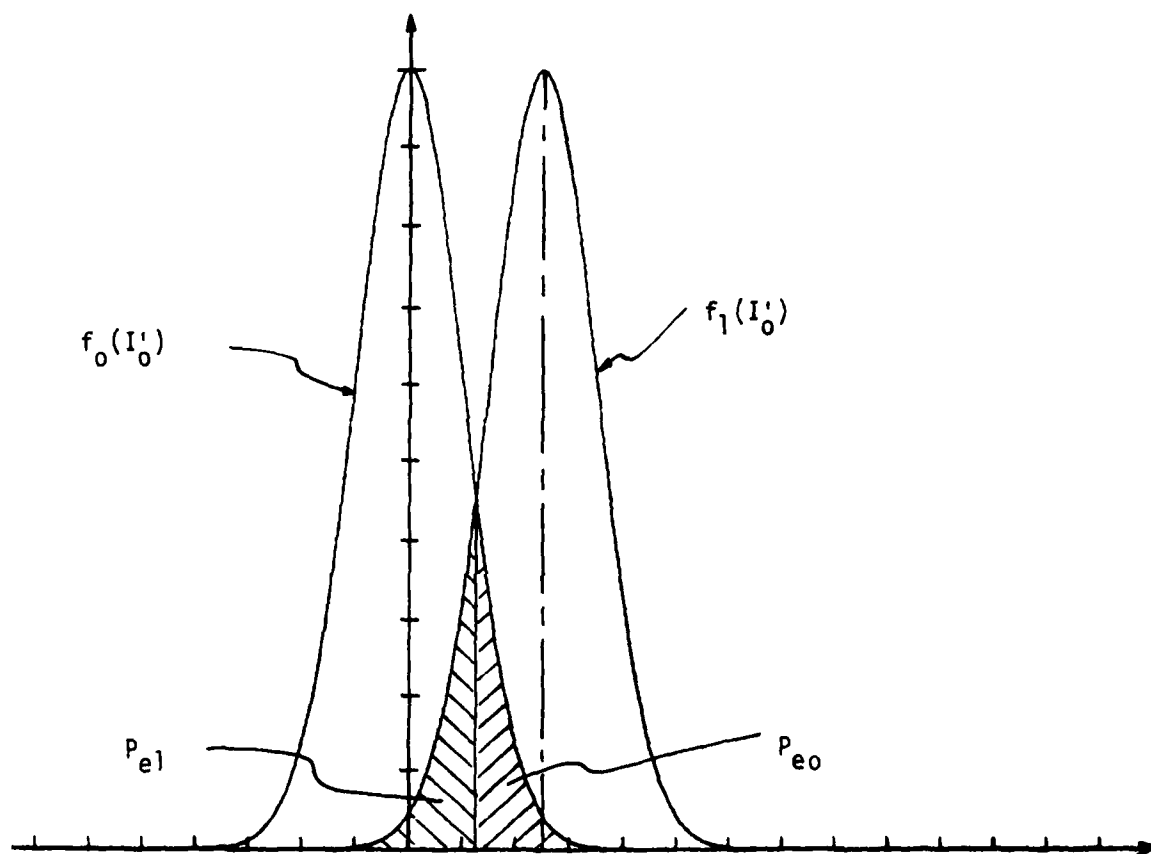


Figure 2-20. Probability Density Distributions of the Detector Output for a Dark and a Bright Area of an Incoherent Image.



will be large and the output image will have a poor fill and become spotty. For our present purpose, let us set  $T = A/2$  and require that  $P_{e0} = P_{e1} \leq 0.1$ .

Since

$$P_{e0} = P_{e1} = \frac{1}{2} \left( 1 - \operatorname{erf} \frac{A}{2\sqrt{2}\sigma} \right) \quad (2-19)$$

where

$$\operatorname{erf} x = \frac{2}{\sqrt{\pi}} \int_0^x e^{-y^2} dy, \quad (2-20)$$

with  $P_{e0} = P_{e1} \leq 0.1$ , we obtain a limit on the SNR,

$$\frac{A}{\sigma} \geq 2.6 \quad (2-21)$$

That is, the signal-to-rms-noise ratio must be larger than or at least equal to 2.6.

First, let us assume that the intensity distribution of the background is uniform; that is,  $B(t) = B$ . We can then remove the bias by simply lowering the dc level of the output electrically. We further assume that we can work near the saturation level of the detector array. The signal-to-noise ratio of the bias subtracted output from a CCD imaging detector for a single frame can be written as

$$\frac{A}{\sigma} = \frac{S}{\underbrace{\sqrt{\left(\frac{B}{D}\right)^2 + B}}_{\substack{\text{thermal noise, dark} \\ \text{current shot noise}}} \quad \text{shot noise} \quad (2-22)$$

where  $D$  is the dynamic range of the detector. (Dynamic range is defined as peak signal output at saturation level divided by rms noise for a bandwidth given by the detector scan rate.) For a CCD detector, the typical full well limit is about  $B = 10^6$  and the

dynamic range is around  $D = 1000$  (60 dB). The SNR for a single frame is then equal to

$$\frac{A}{\sigma} = \frac{S}{\sqrt{\left(\frac{10^6}{10^3}\right)^2 + 10^6}} = \frac{S}{\sqrt{2} \times 10^3} \quad (2-23)$$

Since we need  $A/\sigma \geq 2.6$ ,  $S$  must be  $\geq 3.68 \times 10^3$ . Converting SNR to image contrast, we note that

$$\frac{I_{\max} - I_{\min}}{I_{\max} + I_{\min}} \times 100\% \approx \frac{S}{2B} \times 100\% \quad (2-24)$$

Thus, the input image must have a minimum contrast of

$$\frac{3.68 \times 10^3}{2 \times 10^6} \times 100 = 0.184\%$$

in order to provide a SNR of  $A/\sigma \approx 2.6$ .

The SNR of an image can be enhanced by integrating several frames. If the system noise is uncorrelated, then the SNR, after integrating  $N$  frames, becomes

$$\frac{A}{\sigma} = \frac{NS}{\sqrt{N \left[ \left(\frac{B}{D}\right)^2 + B \right]}} = \frac{\sqrt{NS}}{\sqrt{\left(\frac{B}{D}\right)^2 + B}} \quad (2-25)$$

The minimum input image contrast for  $N$  frames is then equal to

$$\frac{2.6 \times \sqrt{2} \times 10^3}{\sqrt{N} \times 2 \times 10^6} \times 100 = \frac{0.184\%}{\sqrt{N}}$$

For example, if we integrate two frames, the minimum input image contrast is 0.13%.

In the above discussion, we have assumed that the background distribution is uniform enough that the bias can be removed by simply

lowering the dc level. If the background bias is not uniform, that is,  $B(t) \neq \text{constant}$ , then one of the schemes described earlier may be employed to remove the bias. First, let us examine the defocus-subtract technique. With this technique, the bias term  $B(t)$  is obtained by defocussing the image, and it is used to subtract a well-focussed frame with fine (high spatial frequency) details. Since the signal is present only in one frame while the noise is present in both frames, subtracting the two frames will result in a SNR of

$$\frac{A}{\sigma} = \frac{S}{\sqrt{2 \left[ \left( \frac{B}{D} \right)^2 + B \right]}} \quad (2-27)$$

The minimum input contrast needed to provide a SNR of  $A/\sigma = 2.6$  is then equal to 0.26%. If we integrate  $N/2$  frames each for the focussed and defocussed images, the SNR becomes

$$\frac{A}{\sigma} = \frac{\frac{\sqrt{N}}{2} S}{\sqrt{2 \left[ \left( \frac{B}{D} \right)^2 + B \right]}} = \frac{\frac{\sqrt{N}}{2} S}{2 \times 10^3} \quad (2-28)$$

The minimum input contrast is then

$$\frac{2.6 \times 2 \times 10^3}{\frac{\sqrt{N}}{2} \times 2 \times 10^6} \times 100 = \frac{0.26\%}{\sqrt{N}}$$

A similar approach is to blur the image of a second frame by low pass filtering instead of defocussing. Once again, the signal is present only in one frame. However, since the second frame is low pass filtered, the amount of noise is reduced by  $\sqrt{H_2/H_1}$  where  $H_1$  is the full bandwidth of the imaging detector array where the dynamic range  $D$  is defined and  $H_2$  is the bandwidth of the low pass filter. The SNR of the subtracted image is

$$\frac{A}{\sigma} = \frac{S}{\sqrt{\left[\left(\frac{B}{D}\right)^2 + B\right] \left(1 + \frac{H_2}{H_1}\right)}} \quad (2-29)$$

For  $H_2/H_1 = 0.1$ , the minimum input contrast is 0.185%. Integrating a total of  $N$  frames, the minimum input contrast becomes  $0.185/N/2\%$ .

Since the defocus-subtract and low pass-subtract processes both perform essentially a high pass operation, it is more efficient to perform the high pass filtering directly. The SNR of a high passed image is equal to

$$\frac{A}{\sigma} = \frac{S}{\sqrt{\frac{H_3}{H_1} \left[\left(\frac{B}{D}\right)^2 + B\right]}} \quad (2-30)$$

where  $H_1$  is the full bandwidth of the imaging detector and  $H_3$  is the bandwidth of the high pass filter. Unlike the first two techniques, high pass filtering requires only one frame. If two frames are also used, then the SNR becomes

$$\frac{A}{\sigma} = \frac{\sqrt{2}S}{\sqrt{\frac{H_3}{H_1} \left[\left(\frac{B}{D}\right)^2 + B\right]}} \quad (2-31)$$

Assuming that  $H_3/H_1 = 0.9$ , then the minimum input contrast is 0.124. Integrating  $N$  frames, the minimum input contrast is reduced to  $0.124/\sqrt{N/2}\%$ .

We have assumed in the discussion above that the image scene is composed of high spatial frequency structures and that the filtering operation does not remove any of the signal energy. Most images, however, contain both high and low frequency components, and the filtering will result in the loss in some of the low frequency information. Encoding the object imager with a speckle pattern gives the

image a high frequency structure that is independent of the characteristic of the object itself. This permits the filtering process to be applied regardless of the type of object scene being imaged.

The signal energy of a speckle image, however, is spread over a larger range of intensities. The probability density distribution of a speckled coherent image can be written as [9]

$$(1/A) \cdot \exp(-I/A) \text{ for } I \geq 0 \quad (2-32)$$

where  $A = \langle I \rangle$  denotes the mean intensity. Detecting the speckle pattern by a detector with a Gaussian noise characteristic, the probability density distribution of the detector output is then equal to

$$g(I) = \frac{1}{\sqrt{2\pi}\sigma} \exp[-I^2/2\sigma^2] \otimes \frac{1}{\langle I \rangle} \exp[-I/A] \quad (2-33)$$

where  $\sigma^2$  is the noise variance and  $\otimes$  denotes the convolution operation.

In Figure 2-21, we show the probability density distribution of a bright and a dark area of a speckled image. The speckled image has the same mean signal level  $A$  and noise variance  $\sigma^2$  as the incoherent image shown in Figure 2-20. The filtered waveform is bipolar, and to display it properly as an image, the waveform must first be rectified to produce an all-positive signal. The probability density distribution after rectification is shown in Figure 2-22. If we choose the same threshold level as before such that  $P_{e0} = 0.1$ , the probability of having a dark spot in a bright area is then equal to  $P_{e1} = 0.438$ . Comparing to the ideal incoherent case where  $P_{e1} = 0.1$ , we see that the image quality of the filtered speckled image is much poorer.

A better image quality can be obtained using the interferometric technique. In Figure 2-23, we show the probability density distribution of an image after the phase shift and subtract process. Once again, the processed output is bipolar, and rectification is needed

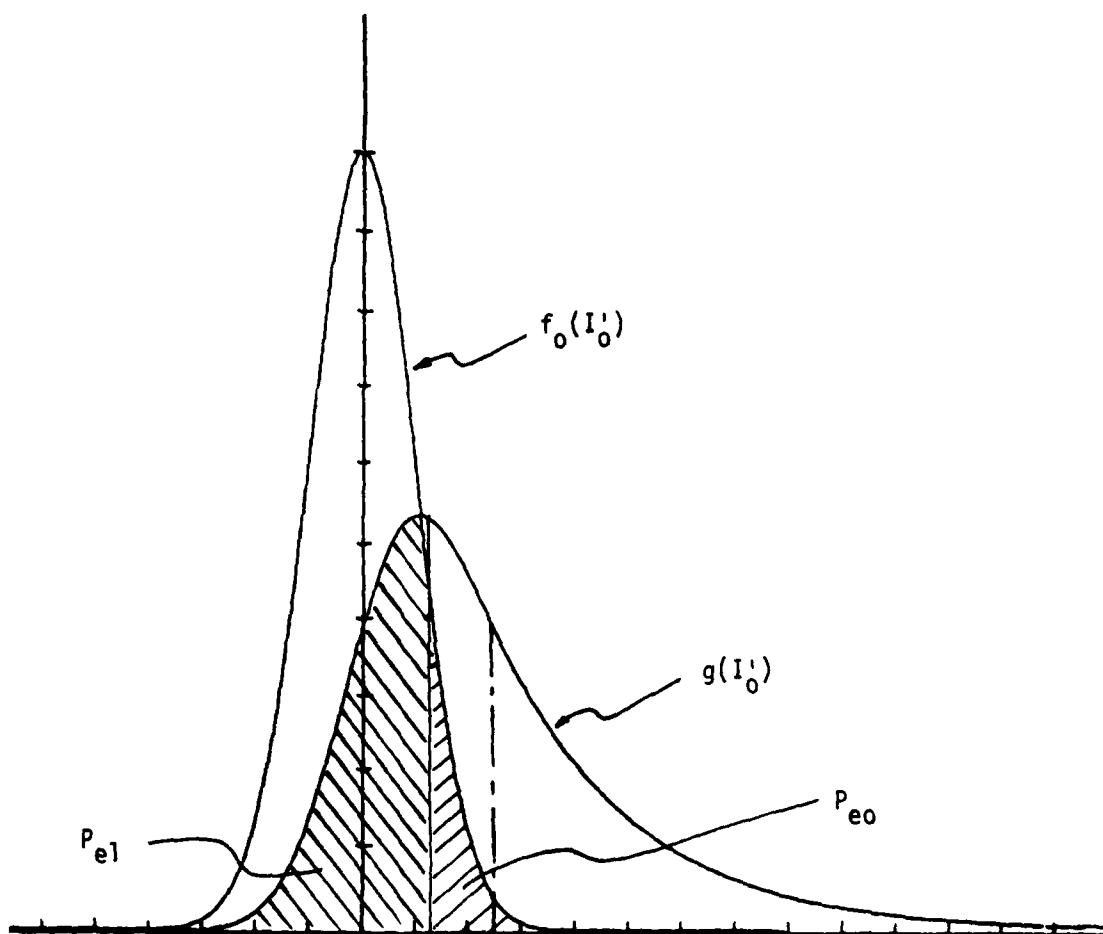


Figure 2-21. Probability Density Distributions of the Detector Outputs for a Dark and a Bright Area of a Speckled Image.

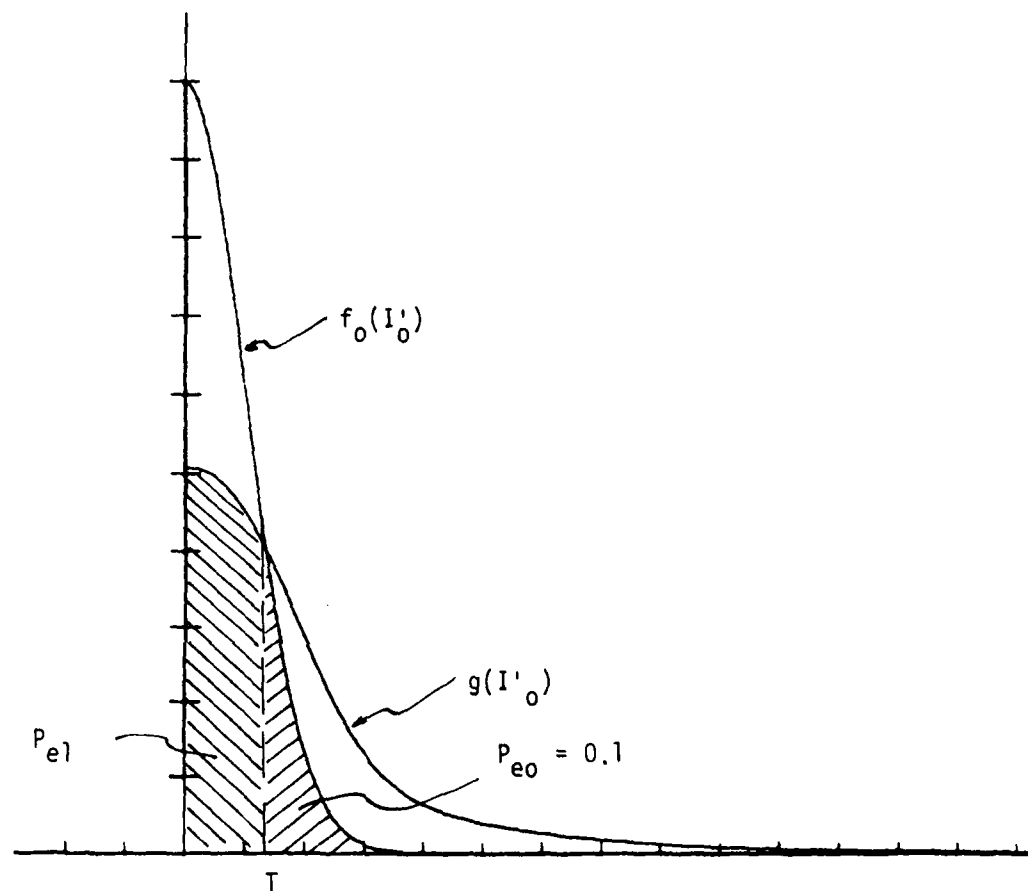


Figure 2-22. Probability Density Distributions of a Filtered and Rectified Speckled Image.

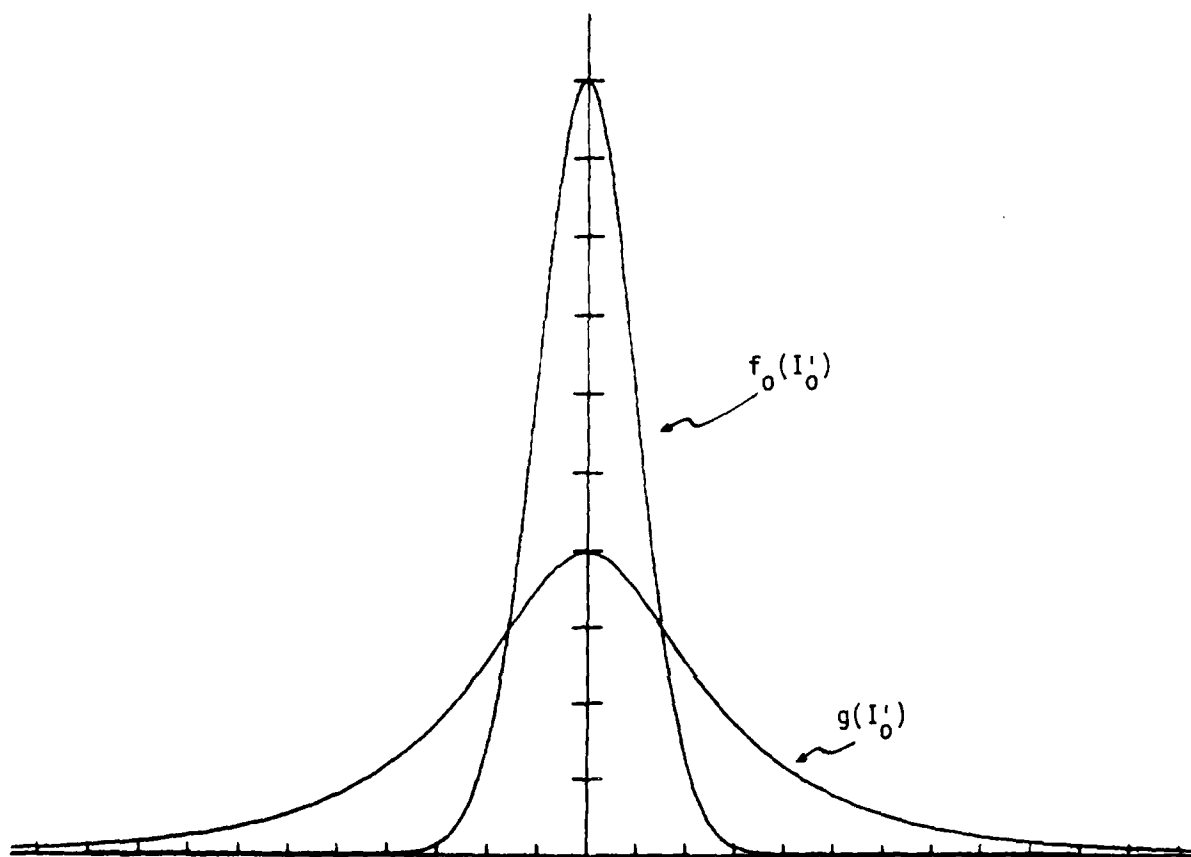


Figure 2-23. Probability Density Distributions of a Speckled Image Processed by the Interferometric Technique.



to produce an all-positive signal for image display. The probability density distribution after rectification is shown in Figure 2-24. Thresholding at the same level, we have  $P_{e0} = 0.1$  and  $P_{e1} = 0.34$ . The image quality is therefore better than simple high pass filtering but still worse than an incoherent image.

The factor of  $\sqrt{N}$  improvement can be achieved by integration only if the noise is uncorrelated. To see if the random system noise in a CCD detector is uncorrelated, the following experiment was performed.

A light bar was imaged onto a Reticon CCD detector array which was read out, digitized and processed with an EG&G 4202 signal averager. The processed digital signal was then entered into an HP 9815A desk top computer which performed statistical analysis on the image.

Besides the time-varying noise, CCD detectors also suffer from deterministic pattern noise. To study the effect of averaging, the pattern noise must first be removed. To do that, a frame was first stored in the signal processor. Then, with the detector covered, a second frame is taken and it is subtracted from the first frame. To average  $N$  frames,  $N$  frames were summed in the signal processor. With the detector covered, another  $N$  frame is summed and then subtracted from the sum of the first  $N$  frames. The result was scaled down by a factor of  $N$  before it was displayed on the monitor. The results after averaging 1, 2, 4, 16, and 64 frames are shown in Figure 2-25.

Signal-to-noise ratio was defined as

$$\frac{V_1 - V_0}{\sigma_{V_0}} \quad (2-26)$$

where  $V_1$  is the mean value of the detector output in the area with the image of the bar and  $V_0$  and  $\sigma_{V_0}$  are the mean value and

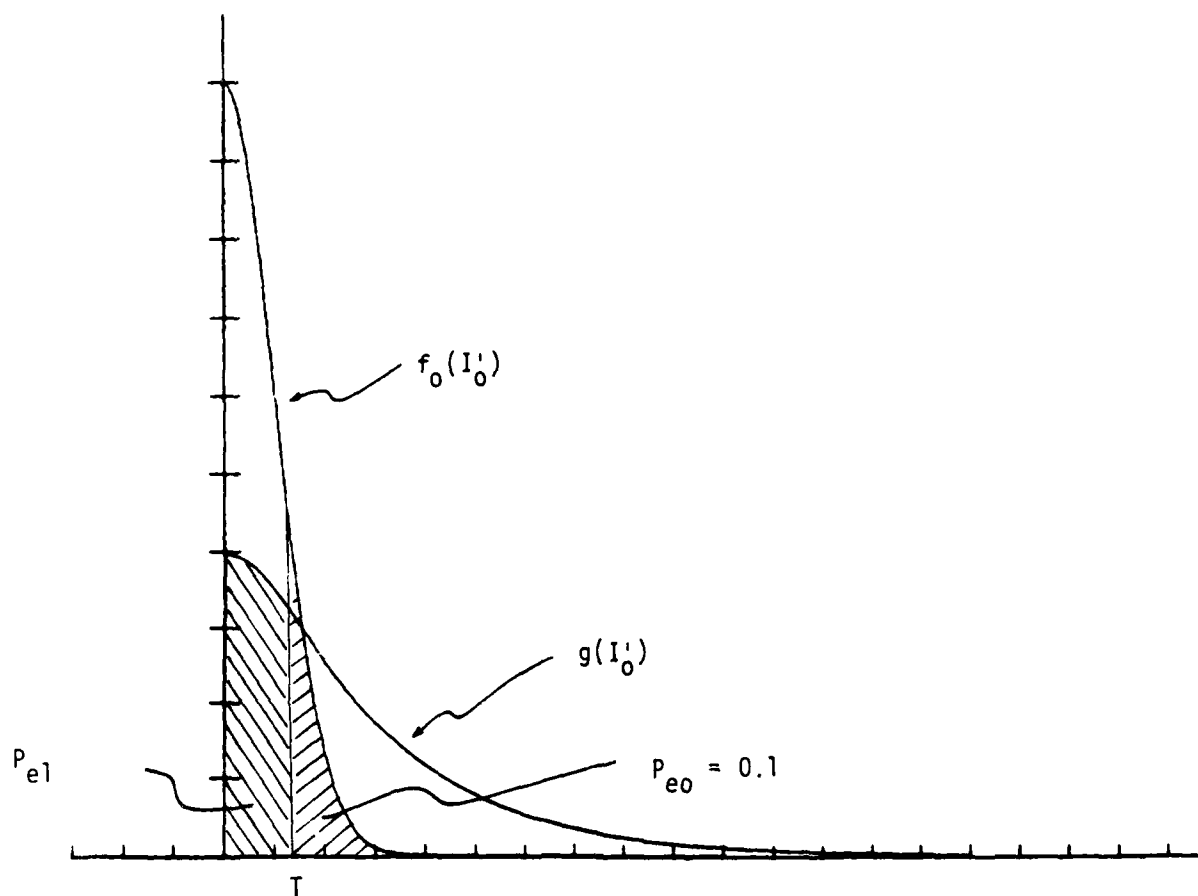


Figure 2-24. Probability Density Distribution of Image Processed by Interferometric Technique After Rectification.

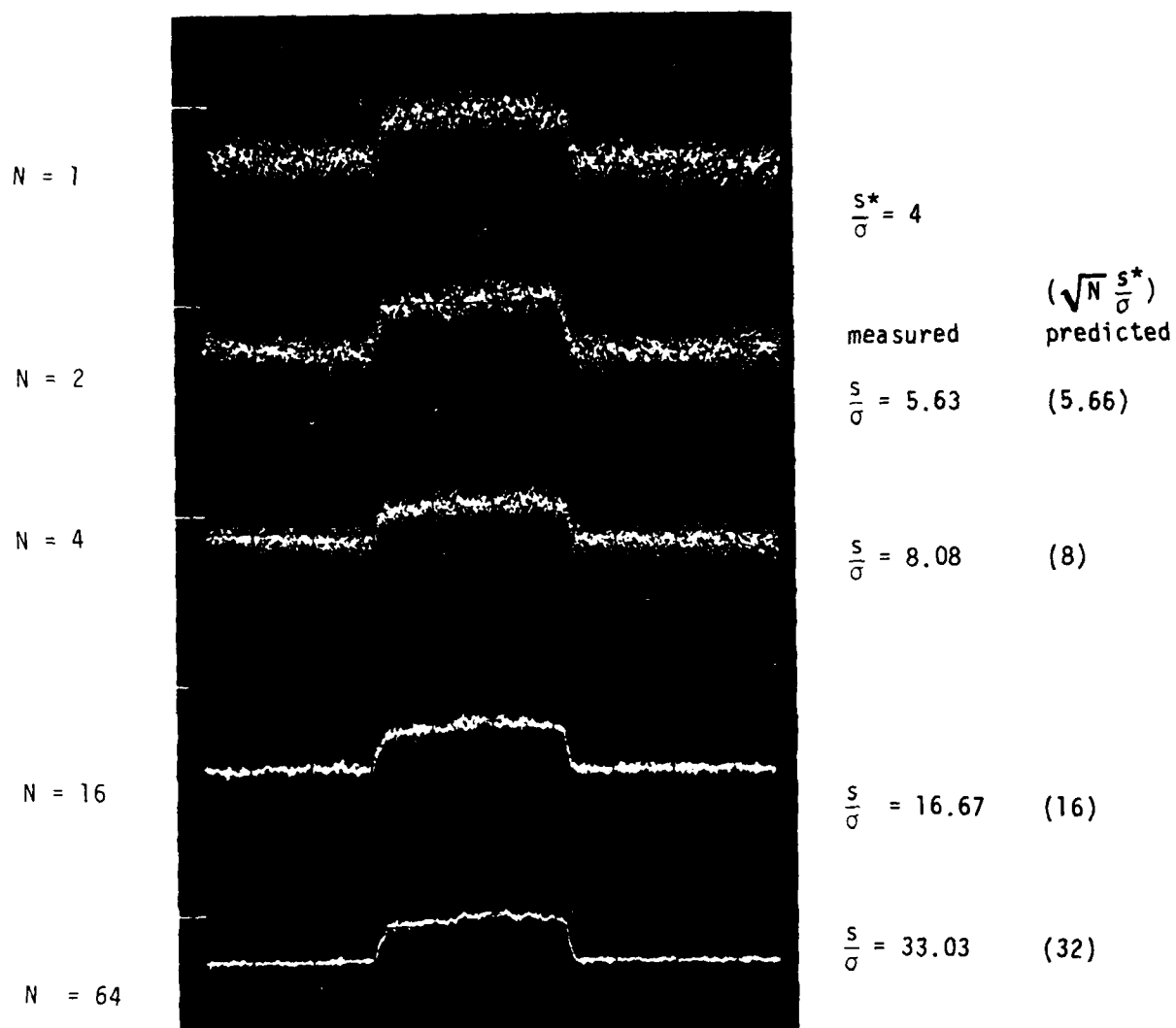


Figure 2-25. Computed and Measured Amount of SNR Improvement by Integrating N Frames.

standard deviation of the detector output in the area with no input signal. For a single frame, the SNR was measured to be 4. If the noise is uncorrelated, the SNR after averaging 2, 4, 16 and 64 frames should be 5.66, 8.0, 16.0 and 32.0, respectively. The measured SNRs after averaging 2, 4, 16 and 64 frames were 5.63, 8.08, 16.67 and 33.03, respectively. They are very close to the predicted values for uncorrelated noise. We can therefore conclude that the random detector noise from a CCD detector is uncorrelated.

A more dramatic demonstration of the effectiveness of frame integration is shown in Figure 2-26. In Figure 2-26(a), we have the isometric plot of an image retained with a vidicon camera. The signal-to-noise ratio of the image is about 2.5 to 1, and one can barely recognize the image of a cross. In Figure 2-26(b), we show the result after integrating just four frames; the image of the cross became much more distinct. Further improvement in image quality was obtained by integrating 16 frames as shown in Figure 2-26(c).

The techniques described in this section can be implemented completely by analog means. The subtraction of two frames can be achieved with the use of an analog delay line. Analog delays, however, tend to introduce noise which is critical in the present application. More practical is a hybrid approach. The estimation of the background, which is computationally more difficult, can be performed by analog means while the subtraction which is computationally simple can be performed digitally. In the next section, we present an all-digital approach for estimating the distribution of the added background bias.

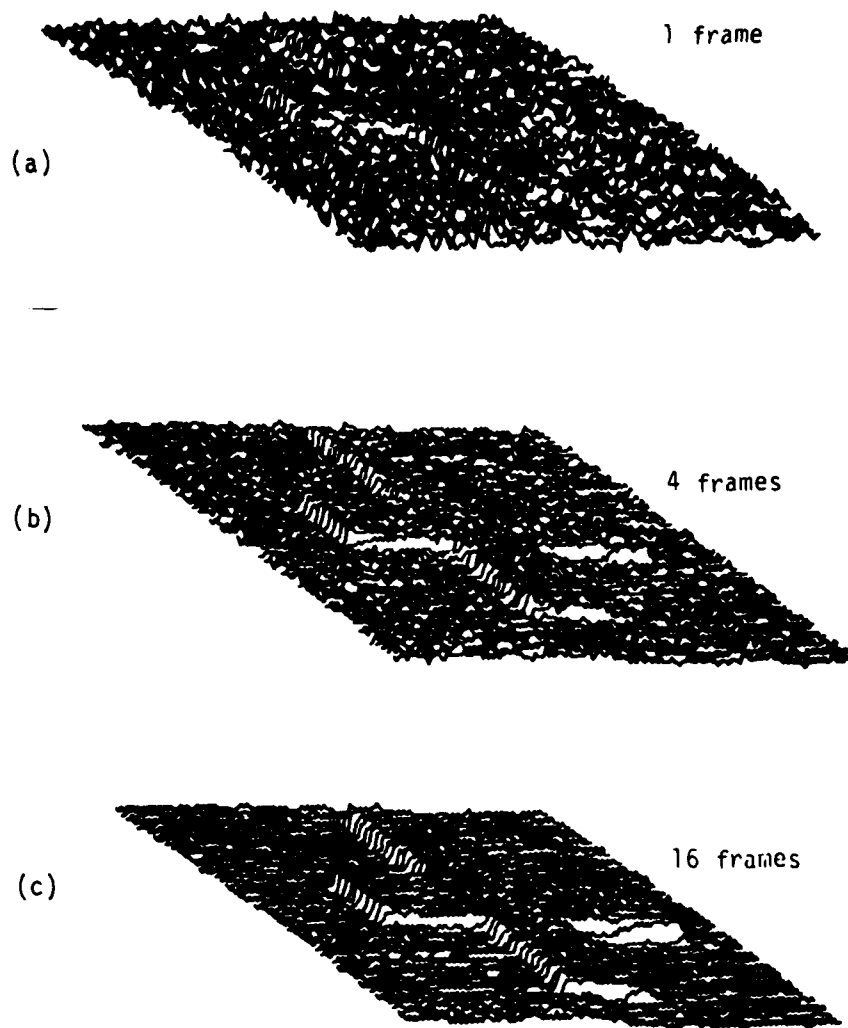


Figure 2-26. Improving the Image Quality of a Two-Dimensional Image by Integration.

### 3 DIGITAL TECHNIQUE

When imaging through a scattering medium, the object scene is obscured by a nonuniform background bias created by the scattered light. The detected light intensity distribution can be expressed as  $B(x, y) + [A(x, y) + g(x, y)]$ .  $B(x, y)$  is the nonuniform bias added to the image, and  $[A(x, y) + g(x, y)]$  describes the image intensity distribution.  $A(x, y)$  represents the slowly changing average values of the image intensity distribution, and  $g(x, y)$  represents the rapidly varying portion of the image. The average values can be obtained by low pass filtering or by defocussing. And, of course, it can also be computed digitally. The average values of the image intensity, however, corresponds to  $B(x, y) + A(x, y)$ , and subtracting it off the image produces a bipolar output  $g(x, y)$ .

To display the processed signal as an image, it is necessary to make the signal all-positive. For incoherent images, this is achieved by adding a bias equalling the largest negative value. Unfortunately, if there are large variations in the average brightness across the image field (i.e.,  $A(x, y) \neq \text{constant}$ ), the intensity distribution of the processed image may be altered enough to make it difficult to recognize. In addition, the bias introduced to accommodate a bright area may obscure an area of low image intensity.

For coherent speckle images, the processed signal can be rectified to create an all-positive output for image display. However, as described in Section 2.3, the filtering and rectification of a speckled image result in an unfavorable distribution of signal energy. The intensity distributions for the bright and dark areas center around the same region, resulting in images with poor SNR.

Ideally, we would like to obtain the values of the background bias  $B(x, y)$  and subtract it out from the image to obtain the object scene  $[A(x, y) + g(x, y)]$ . One possible method is to look at an

image cell of  $n$  pixels diameter and determine the minimum image value within the cell. Such a process may be described as a "sliding pedestal." One can imagine a pedestal being slid along the underside of the two-dimensional waveform that corresponds to the image as shown in Figure 3-1(a). If the pedestal diameter is chosen such that it is wider than the variations in the object scene but narrower than the variation in the background bias, the sliding pedestal will trace out a distribution that is a fairly good approximation of the background bias  $B(x, y)$ . The results obtained with a sliding pedestal, however, exhibit a peculiar step-like structure. A better approximation can be obtained with the use of a "rolling ball." Instead of sliding a pedestal, imagine a ball being rolled along the underside of the image waveform as shown in Figure 3-1(b). By choosing an appropriate ball diameter, the ball will trace out a distribution that is a good approximation of the background intensity variation  $B(x, y)$ . Subtracting this computed background variation from the image, we obtain the desired object scene as shown in Figure 3-1(c).

### 3.1 PROCESSING INCOHERENT IMAGES

The rolling ball processing technique can be employed to process images of targets under natural incoherent illumination. As an illustration, we used a picture of an army tank with camouflage markings as the object and imaged it onto a vidicon tube. The object image is displayed on a television monitor as shown in Figure 3-2(a). A bias is then added to the image to give a nominal signal-to-bias ratio of about 1:60 in the video output. The image with the added bias is shown in Figure 3-2(b). The image contrast was so low that the presence of a tank was not recognizable. In Figure 3-2(c), we show the processed image obtained with the rolling ball technique. The ball diameter was chosen to be 9 pixels, which is slightly wider than the largest white patch in the image. The bias was effectively removed and the image of the tank is clearly recognizable. The SNR

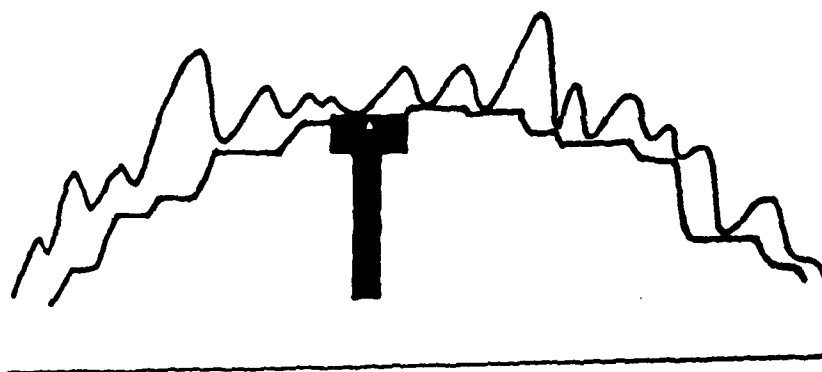


Figure 3-1(a). "Sliding pedestal"

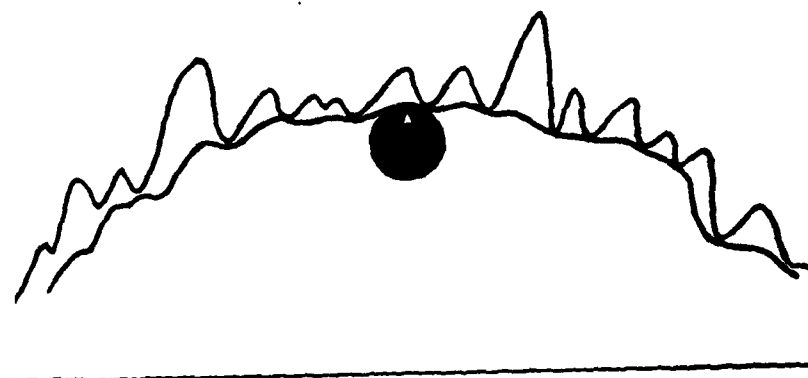


Figure 3-1(b). "Rolling Ball" Processing Techniques



Figure 3-1(c). Processed Output Obtained by Subtracting the Estimated Added Bias from the Input Image.

Figure 3-1. Bias Removal by Sliding Pedestal and Rolling Ball Processing Techniques.



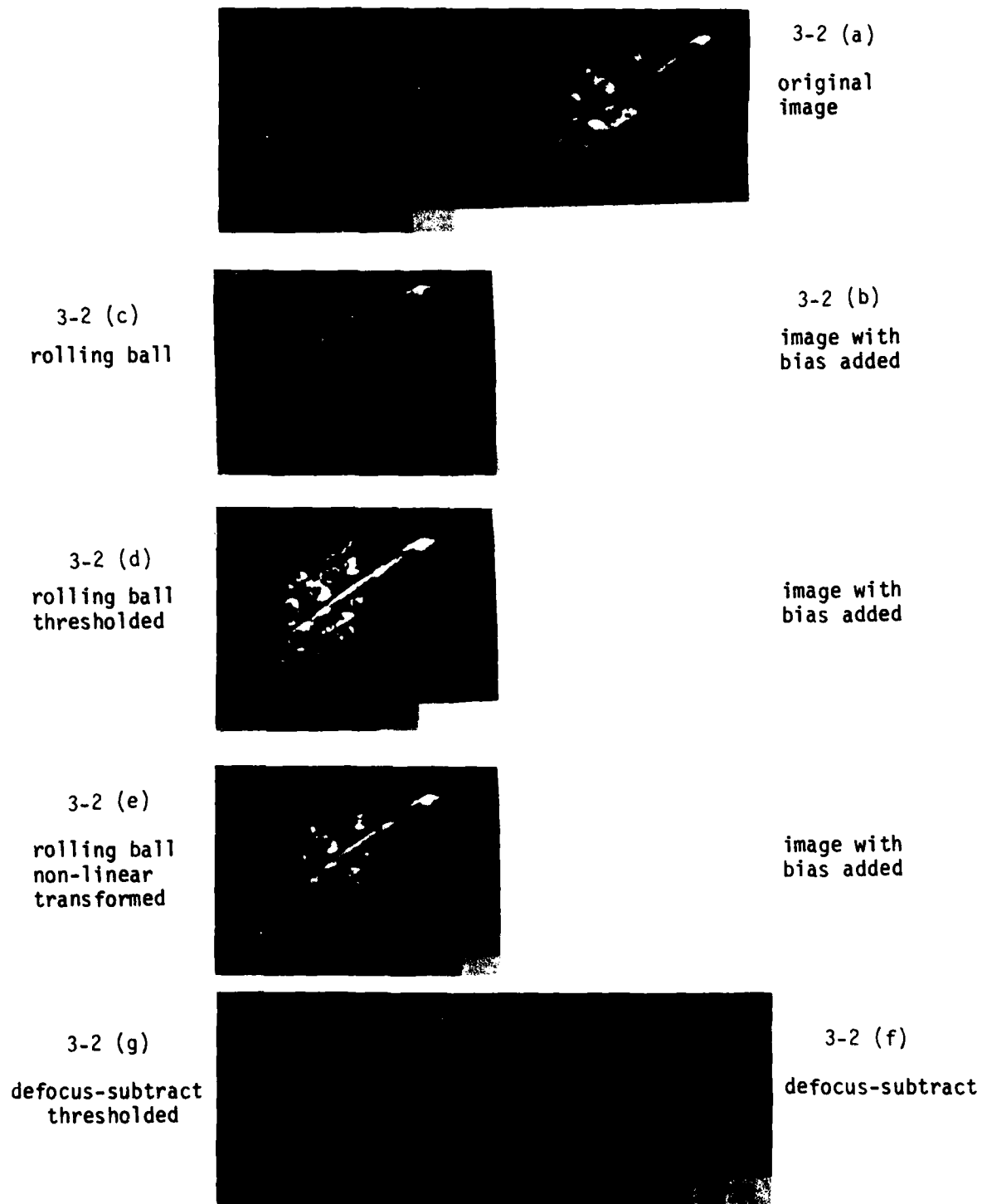


Figure 3-2. Digital Processing of Low Contrast Incoherent Image With the Rolling Ball and Defocus-Subtract Techniques.

of the image can be further enhanced by a nonlinear mapping of the image intensity distribution. In Figure 3-2(d), we show the result of simple thresholding. The background random noise is significantly suppressed while the object image is slightly degraded. Further enhancement may be achieved by the use of a more optimum nonlinear function. The image in Figure 3-2(e) is obtained with the nonlinear function shown in Figure 3-3. The background noise is almost imperceptible. For comparison, we also processed the image by the defocus-subtract technique. The result is shown in Figure 3-2(f); the image of the tank is barely recognizable. The poor result is due to two factors. First of all, as pointed out in Section 2, the random noise is present in both frames while the signal is present in only one frame. Subtracting the two frames resulted in a drop in SNR by a factor of 2. The bipolar nature of the image and the added bias also contribute to make the image difficult to recognize. In Figure 3-2(g), we processed the subtracted image by the nonlinear function shown in Figure 3-4 to improve the SNR of the image. The image of the tank is still just barely recognizable in sharp contrast with the clear images in Figure 3-2(d) and Figure 3-2(e) obtained with the rolling ball technique.

The rolling ball performs essentially a filtering operation with the ball diameter determining the filter bandwidth. If the ball size is made too small, a loss in low frequency information will result. If the ball size is too large, the ball may not be able to follow the variation of nonuniform background closely, resulting in a less than perfect background removal. In addition, the processing time is proportional to the square of the ball diameter. Thus, making the ball size too large will unnecessarily slow down the processed speed. Beside the high pass effect, there is also a halo effect for an isolated dark object on a bright background. The halo gives the image a peculiar look, but the image is not any more difficult to recognize since the object image inside the halo is not altered.

Output

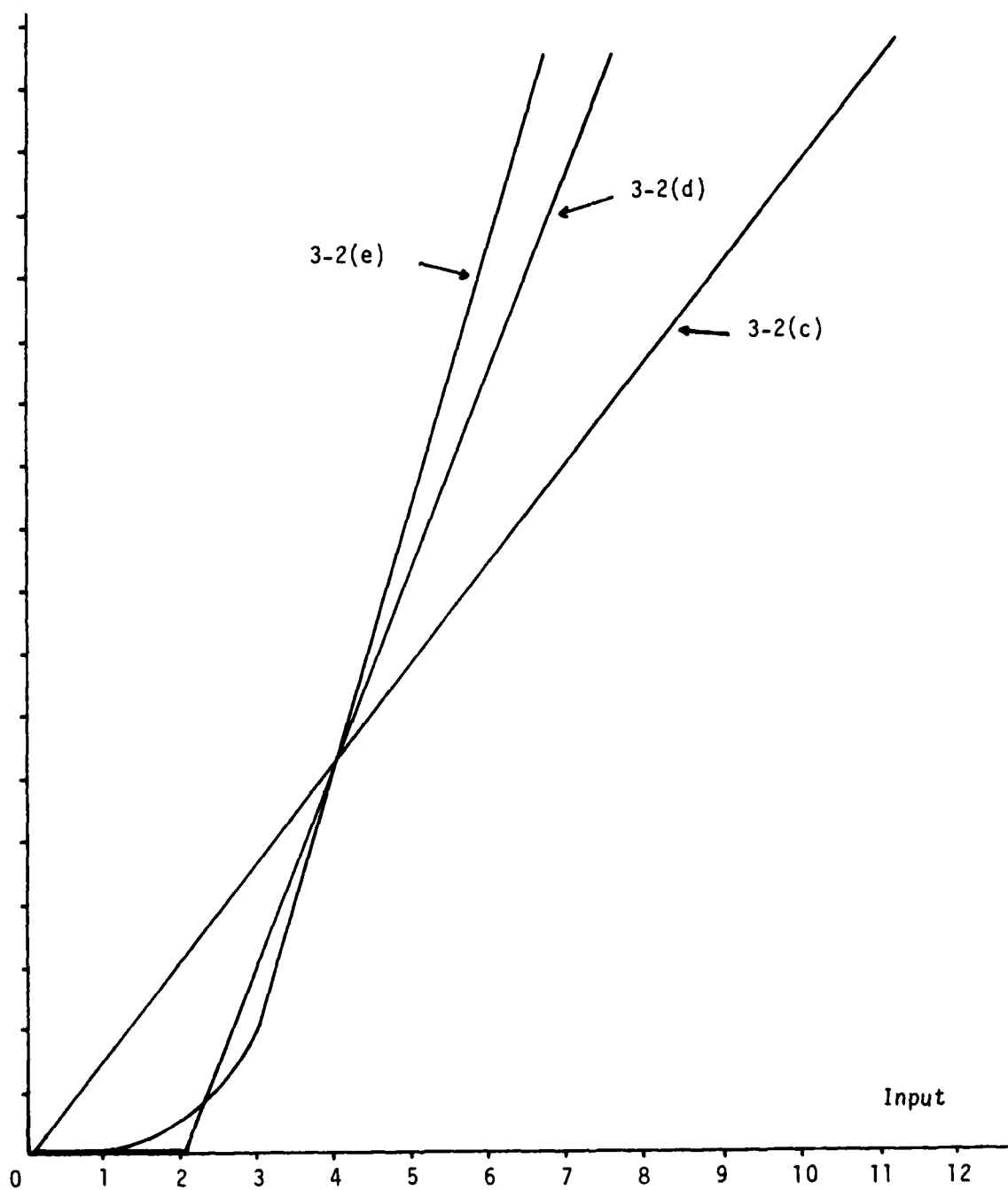


Figure 3-3. Intensity Mapping Functions Used in Figures 3-2(c), 3-2(d) and 3-2(e).

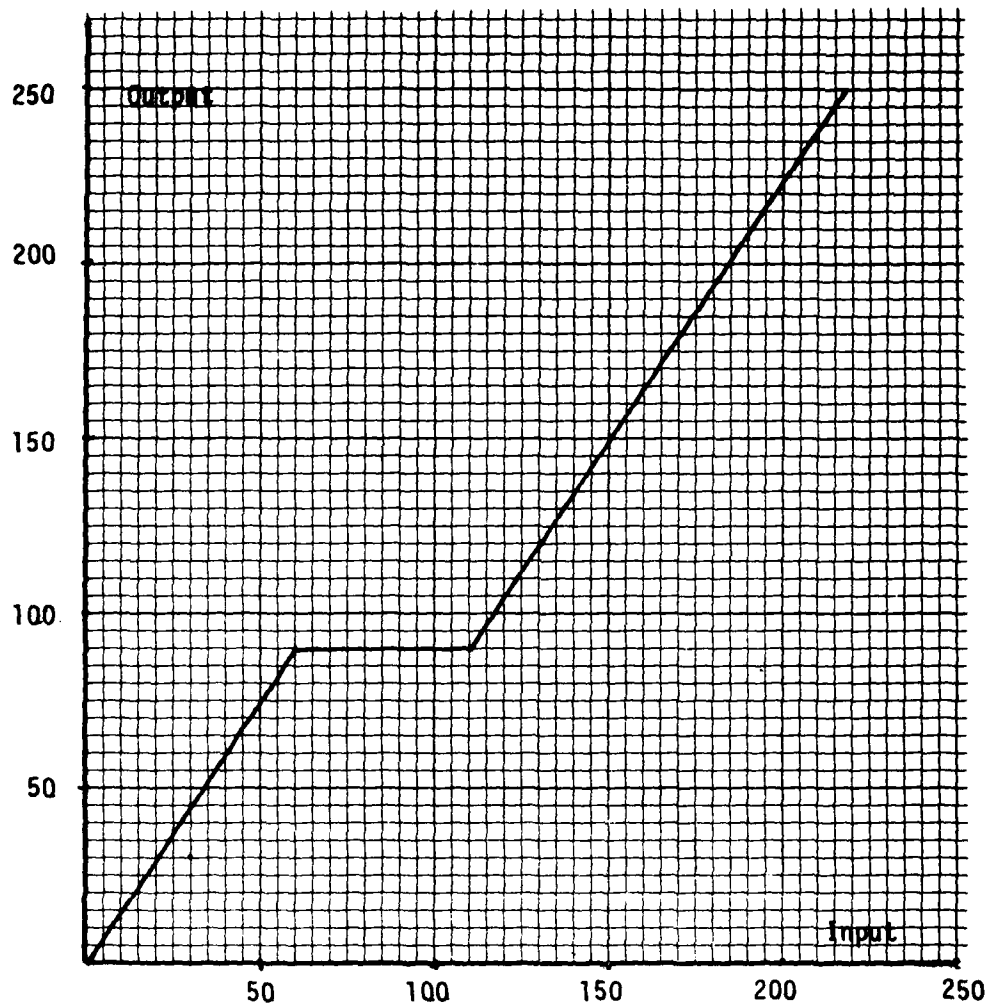


Figure 3-4. Intensity Mapping Function Used in Figure 3-2(f).

Both of these effects are illustrated in Figure 3-5. One way to avoid the halo effect for dark objects on a bright background is to roll the ball on the top instead of on the bottom. This will result in a contrast reversed image without any halo, as shown in Figure 3-6. After thresholding, the image contrast can easily be reversed to produce a normal image.

### 3.2 PROCESSING COHERENT IMAGES

All the background bias removal techniques we discussed operate on the video output of the imaging detector. However, the background bias ideally should be removed before it reaches the detector. When imaging through scattering atmospheres such as fog and smoke, the background bias is due mainly to sunlight scattering off the turbid atmosphere. The image visibility can be very much improved if we illuminate the target area with monochromatic laser light and use a narrow band interference filter at the detector to reject all other spectral frequencies. By doing so, the added background bias is limited essentially to the forward and back scattered laser light. The main contributor of the background bias, scattered sunlight, is thus removed before reaching the imaging detector. The use of coherent illumination also provides other advantages when used with the rolling ball process.

To optimally process the image, the ball size has to be chosen such that it is wider than the intensity variations in the object scene but smaller than the variation of the background bias. If the object scene contains a wide range of spatial frequencies, a compromise has to be made in the choice of the ball diameter. The result often is a loss in low frequency information. One way of getting around this problem is to encode the object scene with a high frequency spatial pattern. The speckles in a coherent image provide conveniently such a pattern. Since the light scattered off the moving scatterers does not form speckles (over the integration period of

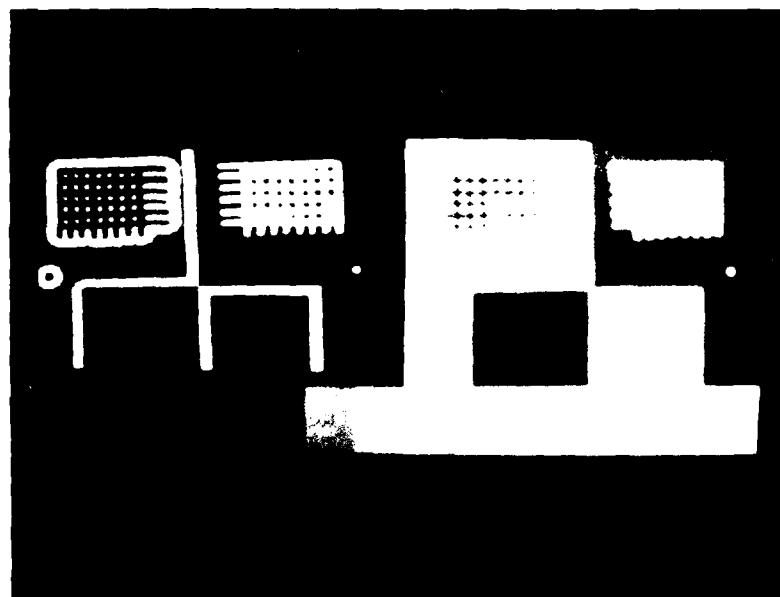


Figure 3-5. Illustration of High Pass and Halo Effects on Images Processed by the Rolling Ball.

the detector), speckles will only be present in the part of the image corresponding to the unscattered portion of the light. Speckle encoding also allows the use of a much smaller size ball. Instead of choosing a ball diameter that is slightly larger than the largest continuous bright patch in the image, the ball size is chosen to be slightly larger than the average speckle size. Since the processing speed is proportional to the square of the ball diameter, speckle encoding permits a higher processing speed. Moreover, speckle size is defined only by the impulse response of the imaging system; it is independent of the object scene. Thus, knowing the system impulse response (i.e., the average speckle size), an optimum ball size can be chosen regardless of the spatial frequency content of the object scene. On the other hand, in the processing of incoherent images, the ball size has to be readjusted to suite the object scene in order to optimize the system performance. As a demonstration, we show in Figure 3-7(a) the detector output of a coherent image (two bars) over a nonuniform background bias. In Figure 3-7(b) and (c), we have the background bias computed by the sliding pedestal and rolling ball techniques, respectively. After subtracting the computed background distribution from the input signal, we obtain the desired speckled image of the two bars as shown in Figure 3-7(d).

To analyze the SNR of an image processed by the rolling ball and to develop means of optimizing the procedure, we need to know how the process alters the probability density distributions of the image. For simplicity, we first analyze the case of the sliding pedestal and then show how the analysis can be modified for the rolling ball. We shall assume in the analysis that each sampled pixel of the digitized image represents one resolution element (or point spread), and the statistics of the intensity distribution among the pixels are the same as the original analog image.

First, we shall obtain the probability density distribution of the values traced out the by sliding pedestal. Let  $f(I)$  be the



original  
image



b.



a.

Figure 3-6. The Image of a Dark Object on a Bright Background Processed by the Rolling Ball. a) Rolling the Ball on the Bottom. b) Rolling the Ball on the Top.





a) Coherent Speckle Image on a Nonuniform Bias



b) Bias Estimated by Sliding Pedestal



c) Bias Estimated by Rolling Ball



d) Processed Output with Nonuniform Bias Removed

Figure 3-7. Applying the Rolling Ball to Coherent Speckle Image.

probability density distribution of an image area of uniform intensity. If we look at a single pixel, the probability that the intensity of the pixel is larger or at least equal to  $I'$  is determined by the probability distribution function.

$$F(I') = \int_{I'}^{\infty} f(I) dI \quad (3-1)$$

If we look simultaneously at  $N$  pixels, the probability that the intensities of all  $N$  pixels are larger or at least equal to  $I'$  is simply

$$H(I') = [F(I')]^N \quad (3-2)$$

$H(I')$  is therefore the probability distribution function for the local minimums over  $N$  pixels. The probability density distribution of the local minimum values can then be obtained by differentiating  $H(I')$ ,

$$G(I') = \frac{dH(I')}{dI'} \quad (3-3)$$

After the background is estimated by the sliding pedestal, it is subtracted from the original image. That is, the intensity of an image having a probability density distribution  $f(I)$  is lowered by an amount  $I'$  with a probability of  $G(I')$ . The probability density distribution of the processed image is therefore equal to

$$\begin{aligned} g(I) &= \int_{-\infty}^{\infty} G(I') f(I - I') dI' \\ &= G(I) \otimes f(I) \end{aligned} \quad (3-4)$$

where  $\otimes$  denotes the convolution operation.

The same approach can be used to compute the probability density distribution of an image processed by the rolling ball algorithm. The difference between a ball and a pedestal is that the ball has

lower values at the edge. Thus, the probability distribution function of the values traced out by the ball can be written as

$$H_B(I') = F_0(I') \cdot F_1(I') \cdot F_2(I') \cdot F_3(I') \cdot \dots$$

where

$$\begin{aligned} F_0(I') &= \int_{I'}^{\infty} f(I) dI, \\ F_1(I') &= \int_{I'}^{\infty} f(I - a) dI, \\ F_2(I') &= \int_{I'}^{\infty} f(I - b) dI, \\ F_3(I') &= \int_{I'}^{\infty} f(I - c) dI, \\ &\vdots \end{aligned} \tag{3-5}$$

and  $a, b, c \dots$  are the differences in intensity values between the central pixel of the ball and the pixels at the edge as illustrated in Figure 3-8. Once again, the probability density distribution of the values traced out by the rolling ball is obtained by differentiating  $H_B(I')$ . Thus,  $G_B(I') = dH_B(I')/dI'$ , and the probability density distribution of an image processed by the rolling ball is equal to

$$g_B(I) = \int_{-\infty}^{\infty} G_B(I') f(I - I') dI' \tag{3-6}$$

Detector noise may be assumed to be Gaussian distributed. Thus, the probability density distribution of the detector input for a dark area of the image is equal to

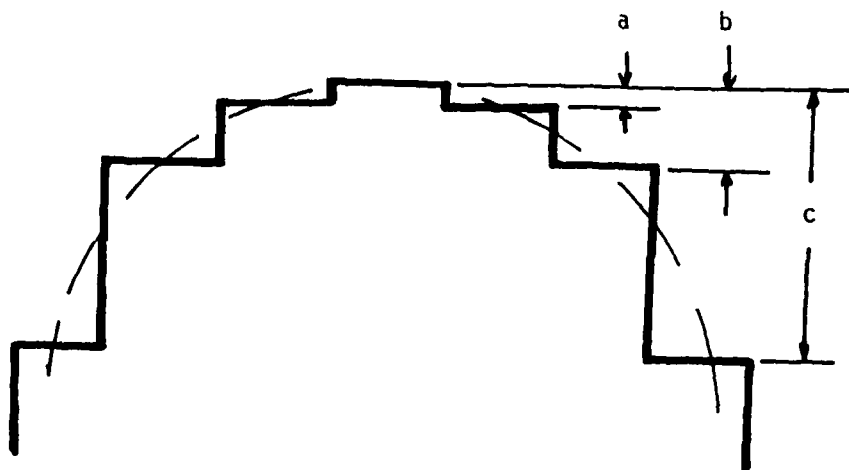


Figure 3-8. Parameters Describing the Shape of the Rolling Ball.

$$f_0(I) = \frac{1}{\sqrt{2\pi}\sigma} \exp [-I^2/2\sigma^2] \quad (3-7)$$

where  $\sigma$  represents the rms noise of the detector output. For a bright area of an incoherent image, the probability density distribution is

$$f_1(I) = \frac{1}{\sqrt{2\pi}\sigma} \exp [-(I - \langle I \rangle)^2/2\sigma^2] \quad (3-8)$$

where  $\langle I \rangle$  is the average detector output for the bright areas. The probability density distributions for the dark and the bright areas of a two-tone image with a signal-to-rms-noise ratio of  $\langle I \rangle/\sigma = 2.5$  are plotted in Figure 3-9.

For an incoherent image processed by the rolling ball technique, the probability density distributions are essentially shifted down as shown in Figure 3-10, provided that the ball size is larger than the white patches in the image scene.

The probability density distribution of the intensity of a speckled coherent image is equal to

$$\exp [-I/\langle I \rangle]/\langle I \rangle \quad \text{for } I \geq 0 \quad (3-8)$$

Assuming that the detector output is linearly proportional to the input intensity, the probability density function for a white area of a coherent image can then be written

$$g(I) = \frac{1}{\sqrt{2\pi}\sigma} \exp [-I^2/2\sigma^2] \oplus \frac{1}{\langle I \rangle} \exp [-I/\langle I \rangle] \quad (3-10)$$

where  $\oplus$  denotes convolution.

In Figure 3-11, we plotted the probability density distributions of a two-tone coherent image with the same  $\langle I \rangle/\sigma$  ratio as Figure 3-9. We see that energy of the coherent speckle image is spread out over a wider range of intensities, and much of the energy is concentrated near  $B$  instead of  $B + \langle I \rangle$ .

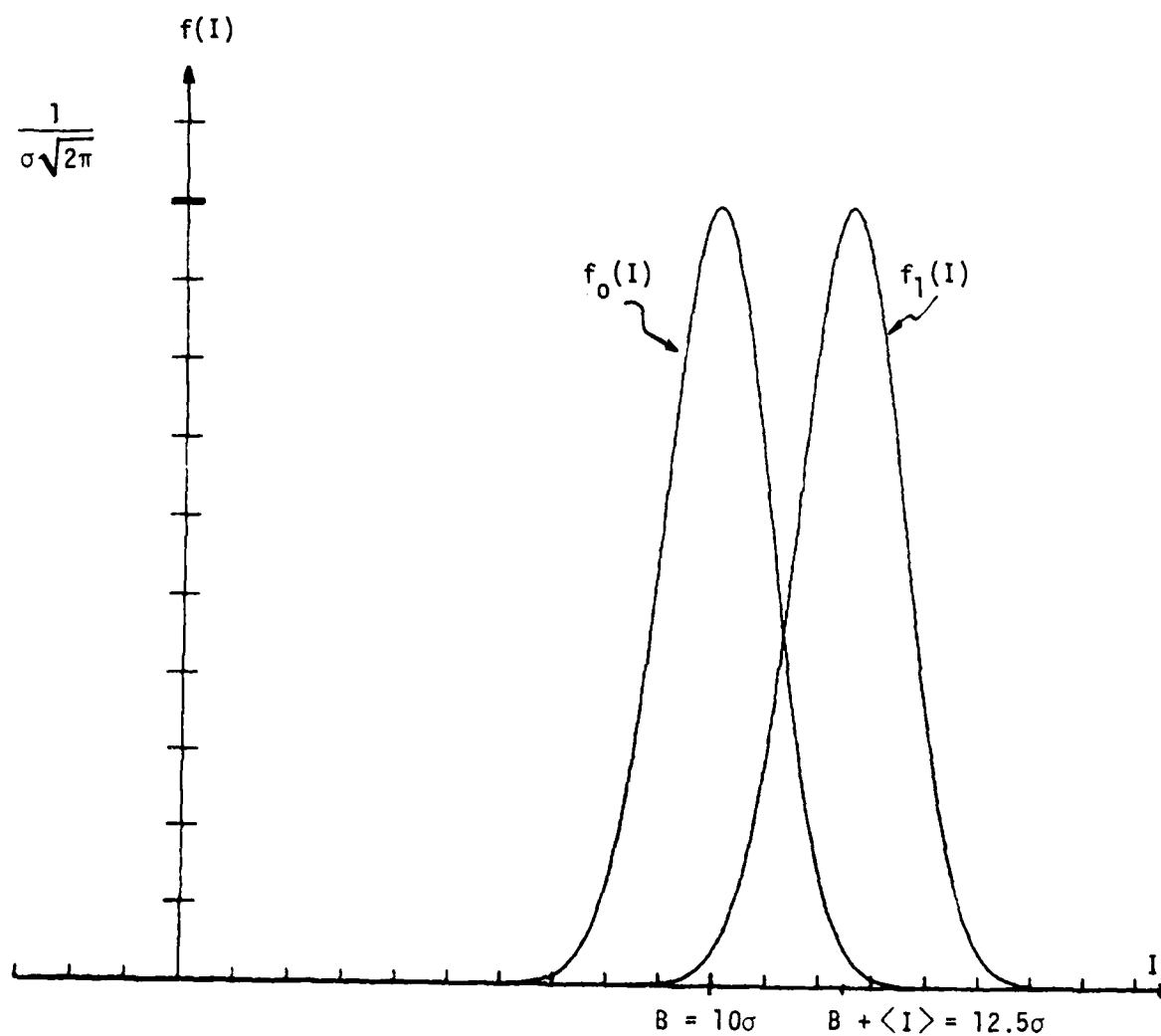


Figure 3-9. Probability Density Distributions of a Biased Two-Tone Incoherent Image with Gaussian Noise.

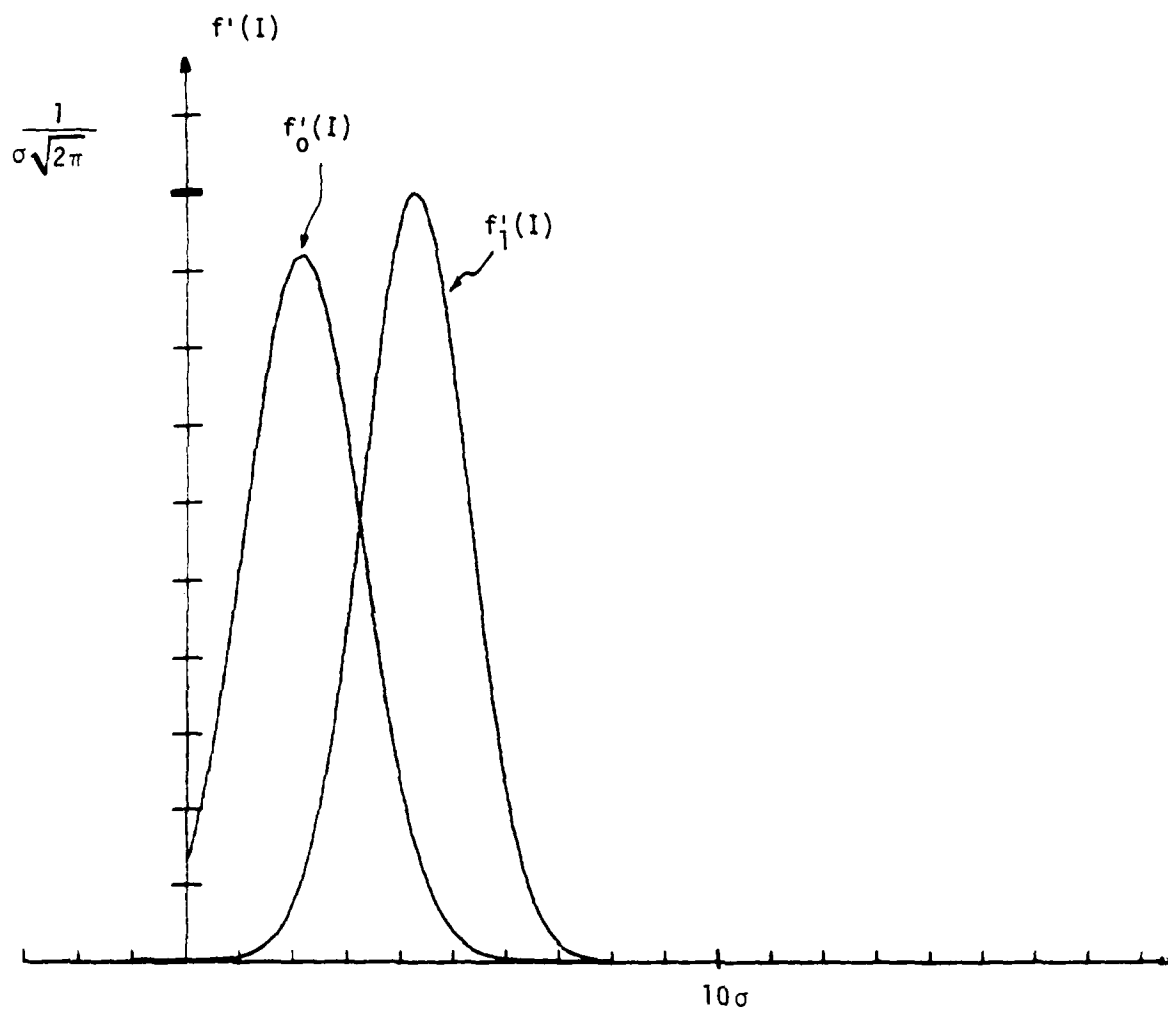


Figure 3-10. Probability Density Distributions of Two-Tone Incoherent after Being Processing by the Rolling Ball Technique.

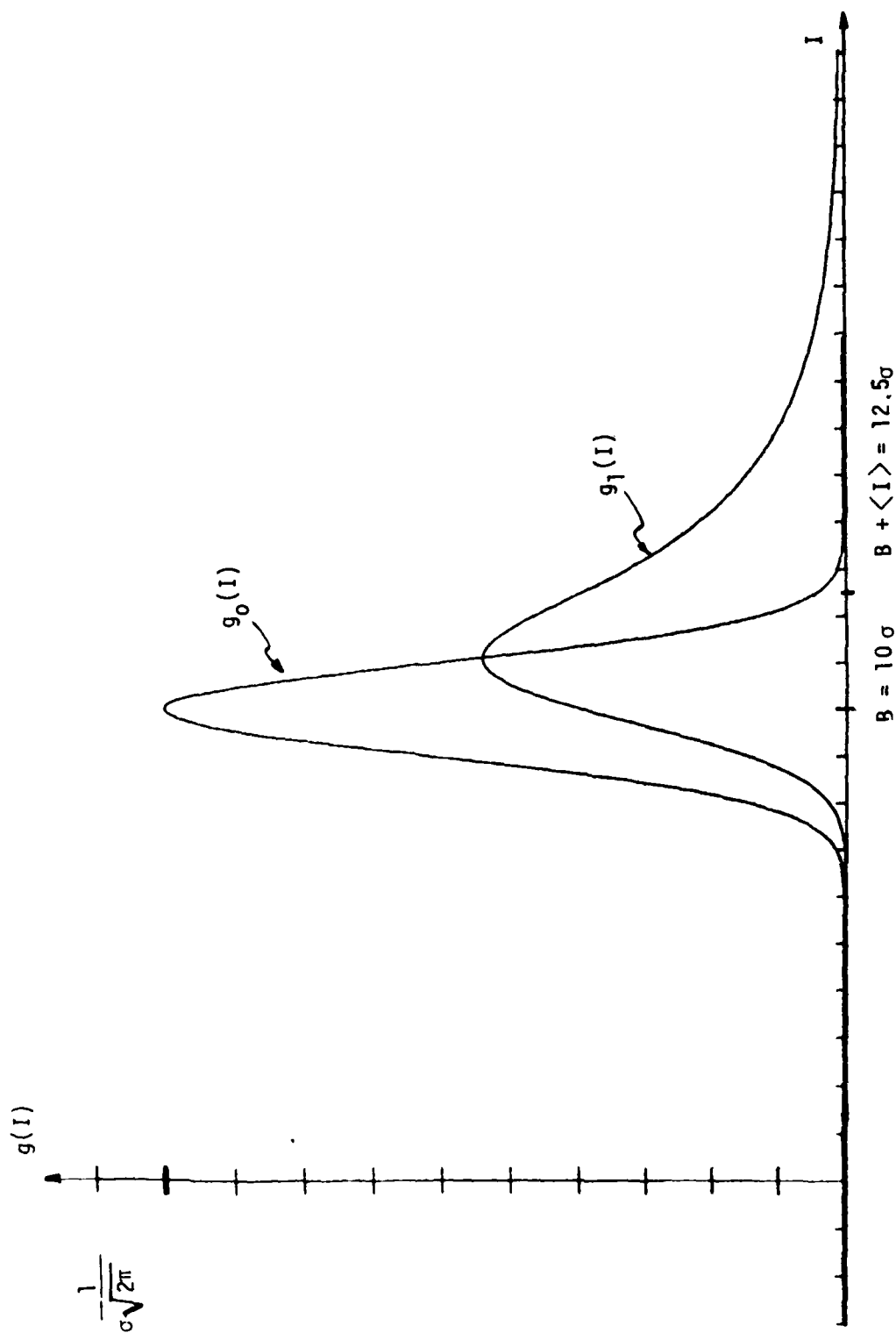


Figure 3-11. Probability Density Distribution of a Biased Two-Tone Coherent Speckle Image with Gaussian Noise.



For a coherent speckle image, the probability density distributions of the processed image are dependent on the ball size chosen. In Figures 3-12 and 3-13, we show the probability density distributions after being processed with two different ball sizes. Comparing Figure 3-10 with Figures 3-12 and 3-13, we see that the energy distribution of the signal for the processed coherent image is rather unfavorable. The probability density distributions of the dark and the bright areas in the image are concentrated near the same intensity level. This unfavorable energy distribution is due to the asymmetric distribution of coherent speckle intensities. However, this same asymmetry can also be taken advantage of to improve the SNR of the processed image.

Before the image is processed with the rolling ball algorithm, let us invert the image waveform (i.e., reversing the contrast as shown in Figure 3-14). The rolling ball processing algorithm is then employed, and we find that its processed image has a much better fill as shown in Figure 3-15. The probability density distributions obtained with the waveform reversal are shown in Figures 3-16 and 3-17 using the same ball sizes as Figures 3-12 and 3-13. The signal energy is now shifted away from the background noise, resulting in a much more favorable signal energy distribution. In fact, comparing Figure 3-17 with Figure 3-10, the SNR performance of the processed coherent image is even better than the incoherent image. We note that larger is the ball size, farther is the signal probability density distribution shifted away from the noise. However, if the ball size is too large, it can no longer follow the variations of the bias, and the bias will not be effectively removed. In addition, the processing speed is proportional to the square of the ball diameter. Thus, using too large a ball will also unnecessarily slow down the processing speed. In Table 3-1, we compared the computed SNR for images processed by the rolling ball algorithm. All the images have an initial SNR of  $\langle I \rangle / \sigma = 2.5$ , and they are thresholded to give  $P_{e0} = 0.1$

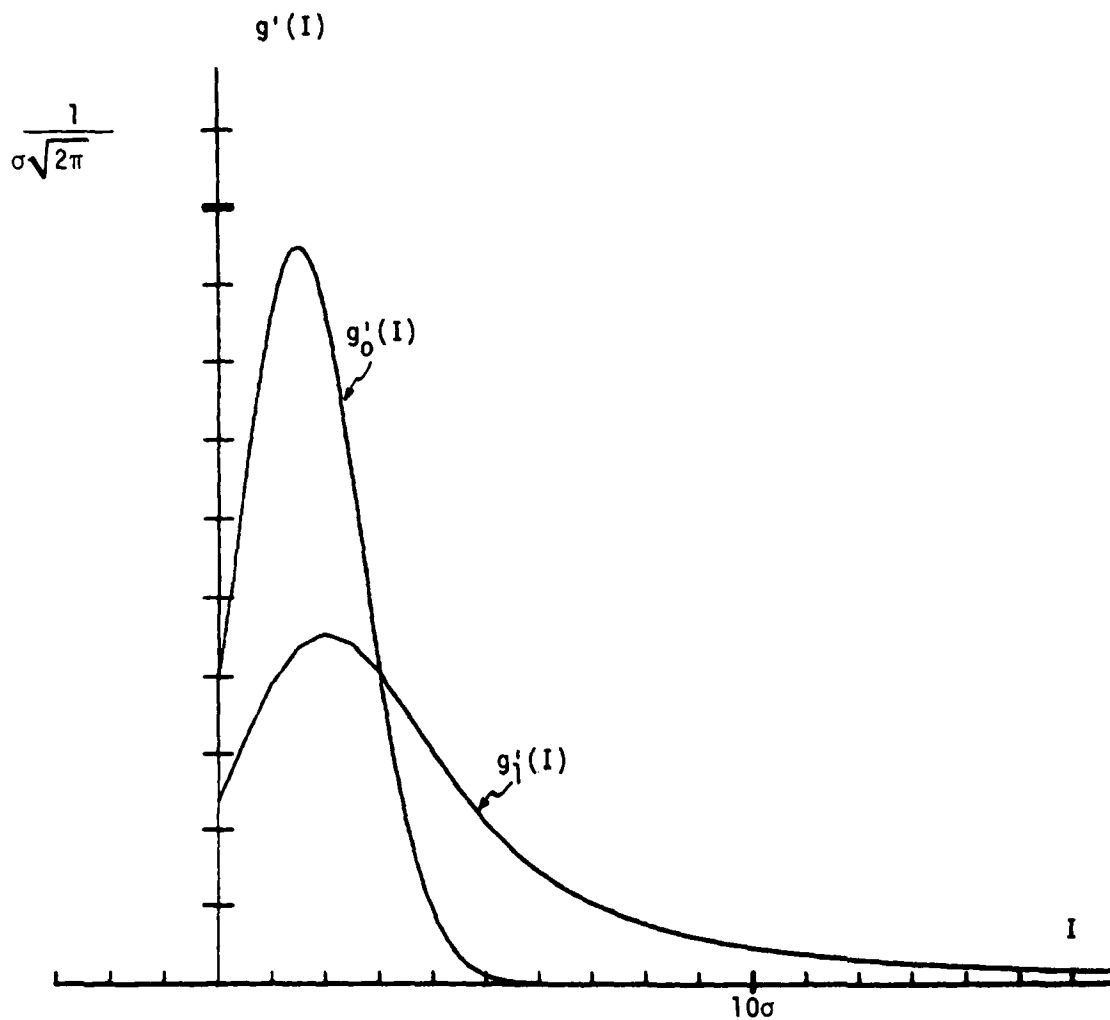


Figure 3-12. Probability Density Distributions for a Two-Tone Coherent Speckle Image after Being Processed by a Rolling Ball Covering an Area of 9 Pixels.

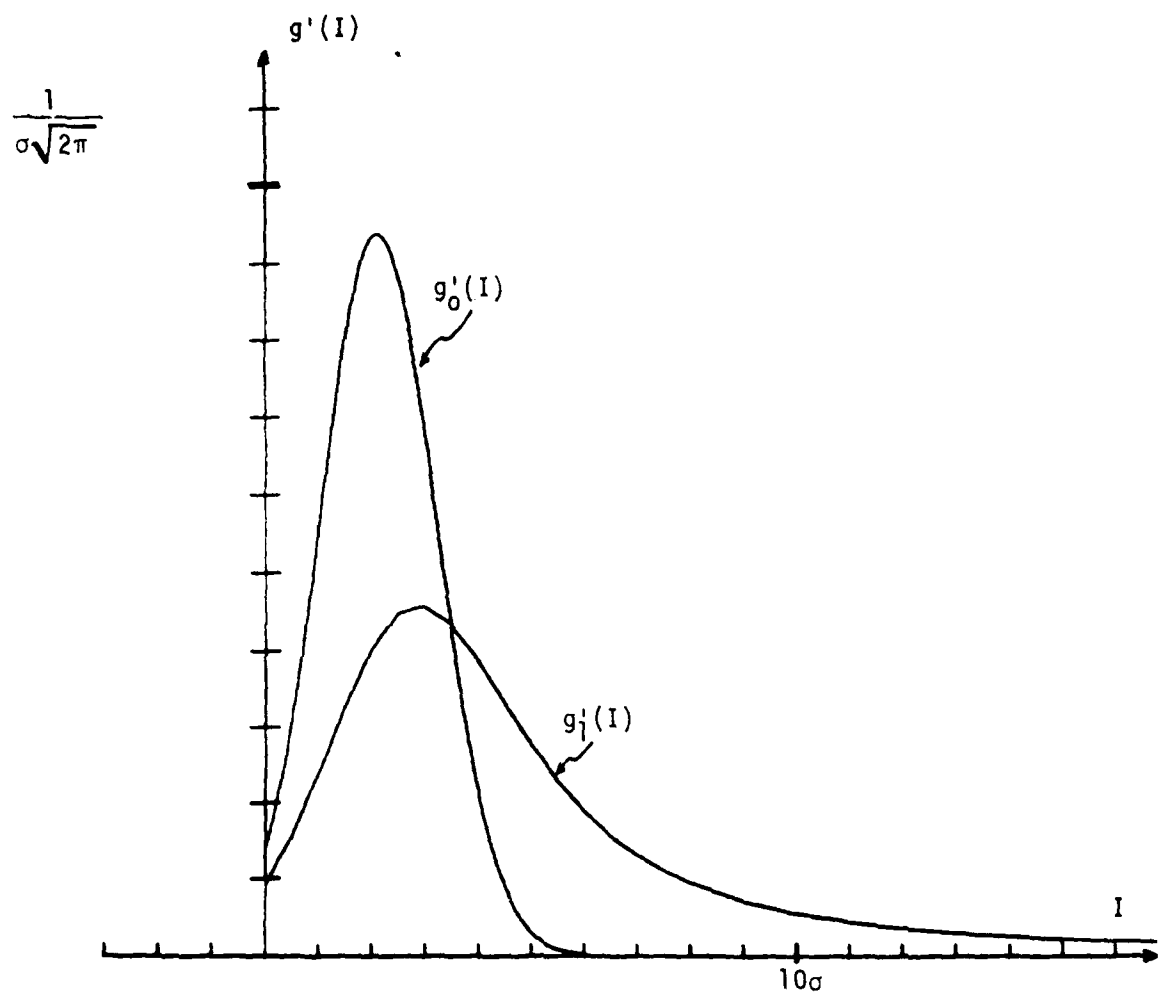


Figure 3-13. Probability Density Distributions for a Two-Tone Coherent Speckle Image after Being Processed by a Rolling Ball Covering an Area of 45 Pixels.

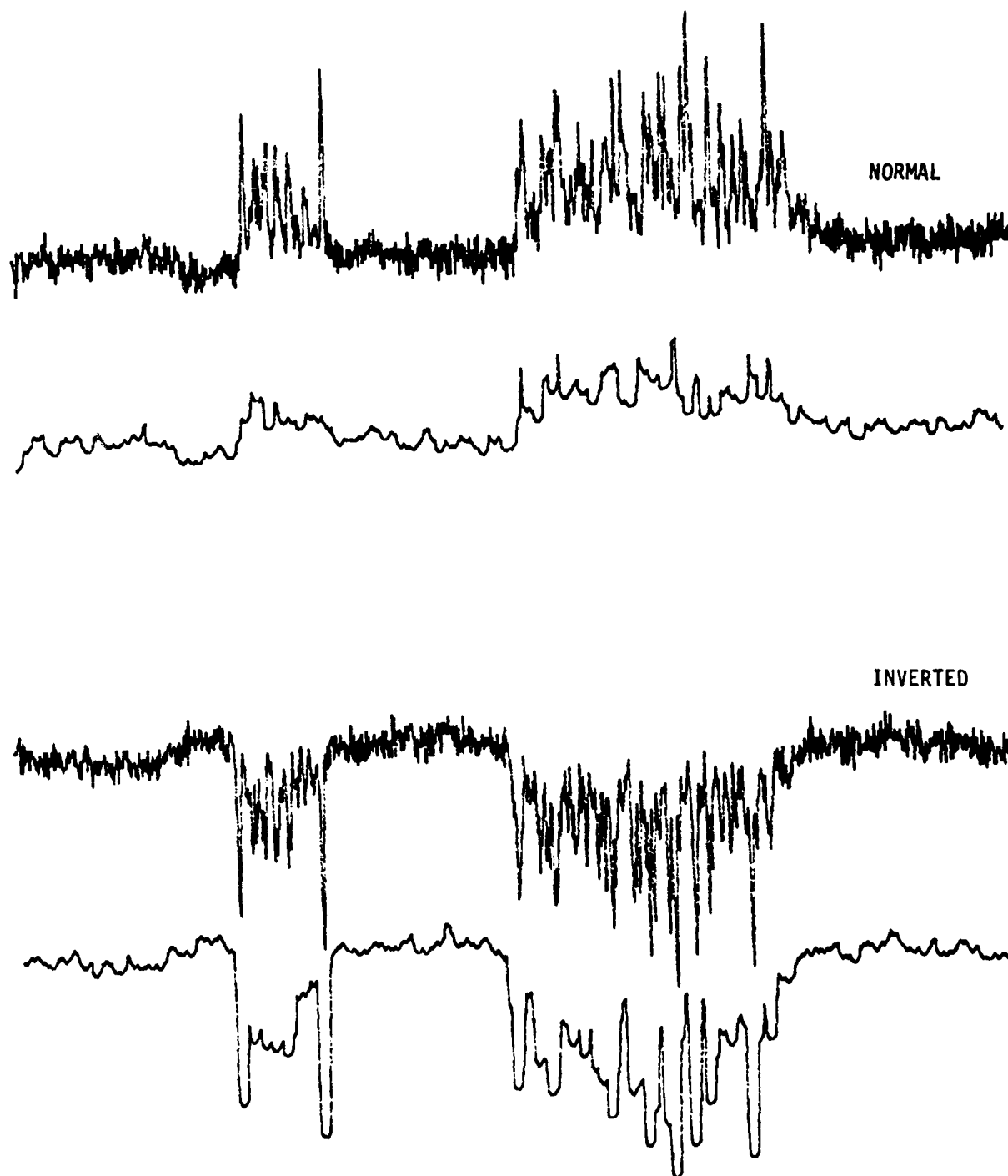
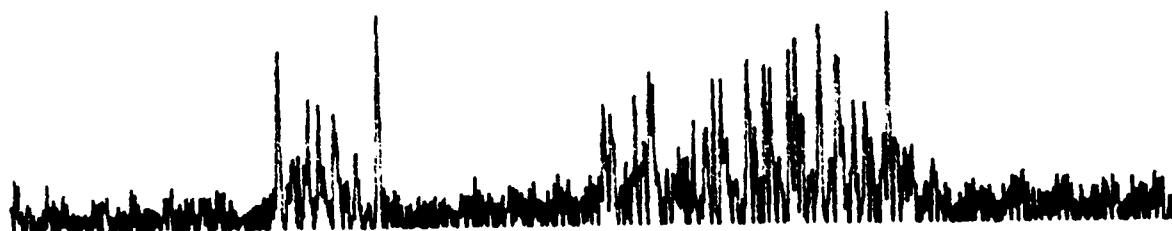
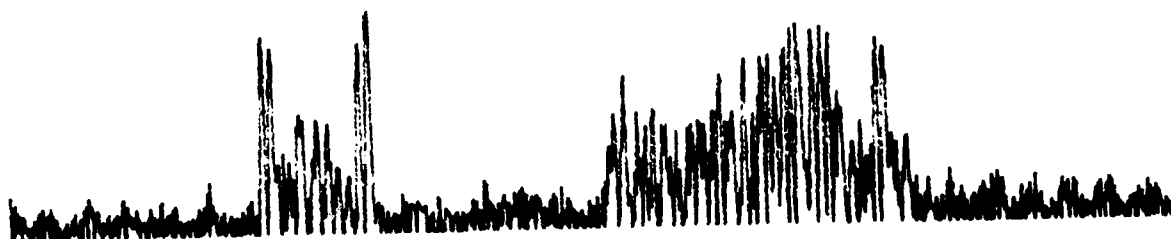


Figure 3-14. Waveform Reversal before Applying Rolling Ball.



WITHOUT WAVEFORM REVERSAL

(B)



WITH WAVEFORM REVERSAL

(A)

Figure 3-15. Processed Coherent Speckle Image a) with and b) without Waveform Reversal.

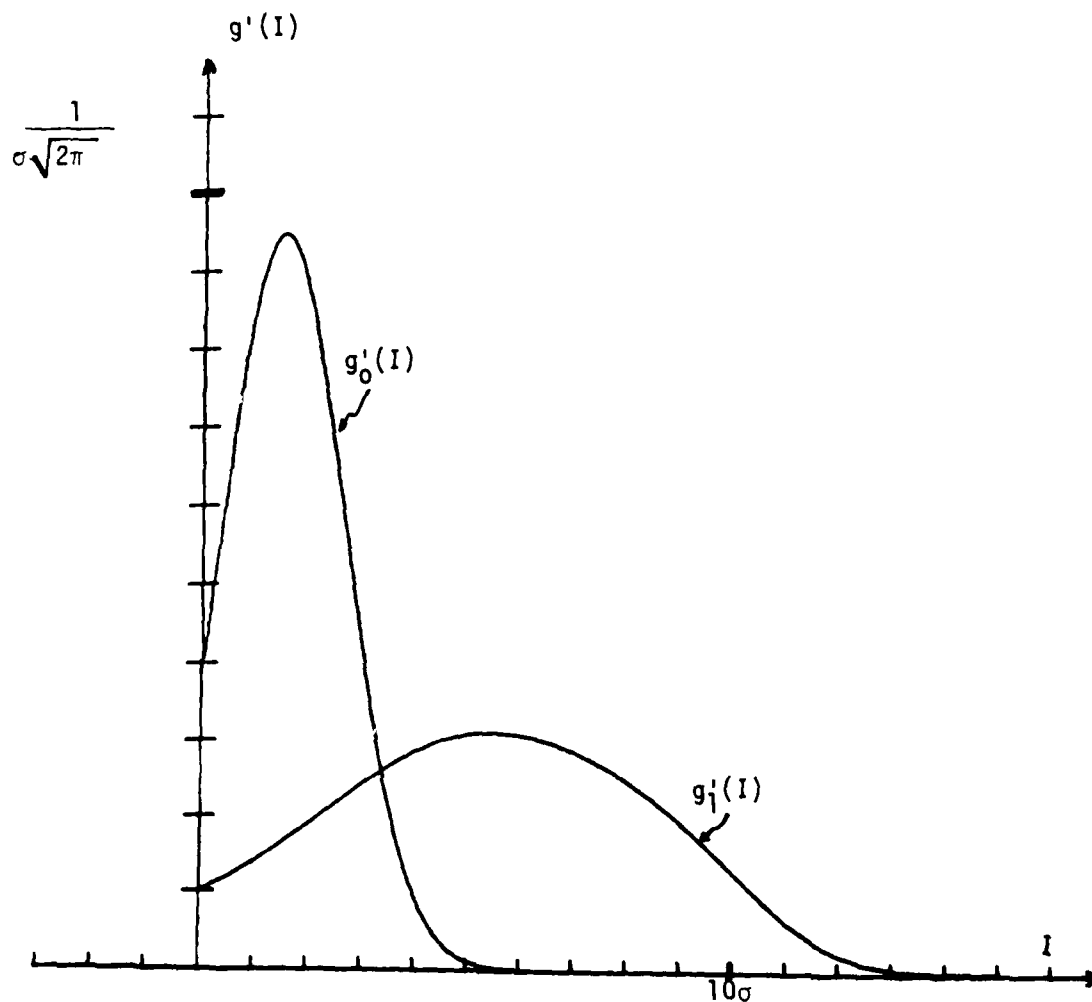


Figure 3-16. Probability Density Distributions for a Two-Tone Coherent Image after Being Processed by a Rolling Ball Covering an Area of 9 Pixels Using Waveform Inversion.

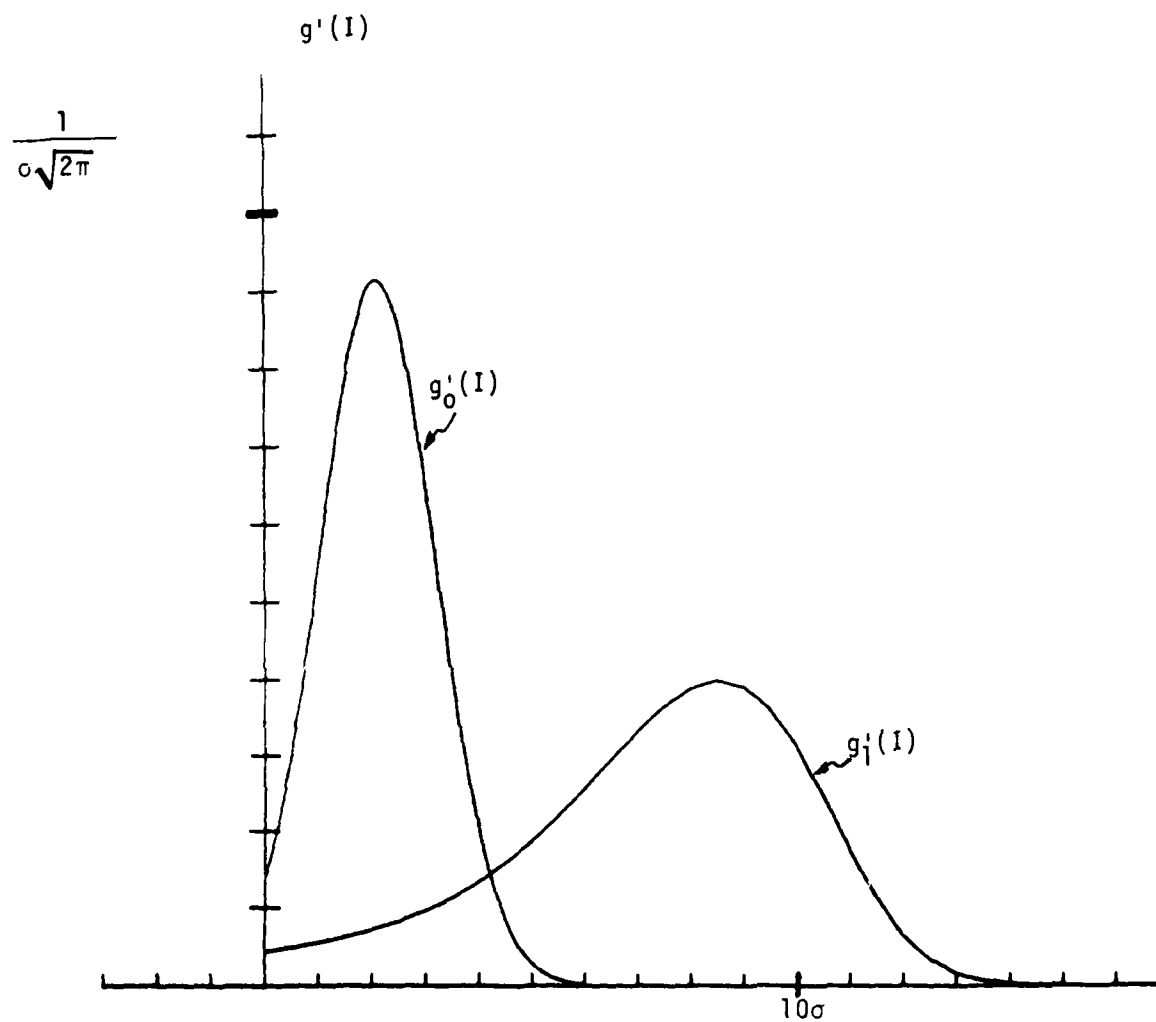


Figure 3-17. Probability Density Distributions for a Two-Tone Coherent Image after Being Processed by a Rolling Ball Covering an Area of 45 Pixels Using Waveform Inversion.

Table 3-1

RATIO OF SIGNAL TO NOISE POWERS WITH  
THRESHOLD LEVEL SET TO GIVE  $P_{eo}=0.1$

	Ball Size 9 Pixels	Ball Size 45 pixels
Incoherent	7	7.7
Coherent	5.4	5.9
Coherent (with waveform inverted)	8	9.2



The speckle pattern in the processed coherent image may also be smoothed using the same rolling ball algorithm by rolling the ball on the top of the processed image waveform. In Figure 3-18, we show the output of the processed image of a light bar and the smoothed coherent image processed with and without the image waveform inversion. We see that the processed coherent image without the waveform inversion produces a higher peak value than the incoherent image, but the image fill is poor. (Also compare Figures 3-9 and 3-13.) The processed coherent image with the use of waveform reversal, on the other hand, exhibits a higher peak value and also a better fill. (Compare Figures 3-9, 3-13 and 3-17.)

We have described a digital technique for the processing of both coherent and incoherent images obtained through scattering media. Preliminary experimental results demonstrated the effectiveness of the approach. A novel image waveform inversion approach was taken to utilize the asymmetry of the speckle intensity distribution to enhance the SNR of the processed image. The advantage of the rolling ball algorithm is that it involves only shifting of data, addition and magnitude comparison, functions that can be performed at very high speed. Operating only on a few neighboring pixels at a time, the amount of memory space required can be quite small. By pipelining the system architecture of the processor, the rolling ball algorithm can be operated at video rate (4 MHz). Our experience at ERIM in developing the cytocomputer has shown that such a digital processor can be constructed in a small package at a modest cost.

In Table 3-2, visibility ranges for different visibility attenuation coefficients ( $D$ ) are compared between direct observation and the use of a CCD imaging detector together with the rolling ball algorithm. In the computation, the minimum required image contrast for direct observation was taken to be 2 percent. The CCD detector was assumed to possess a dynamic range of 60 dB, and the visibility ranges were determined by the criteria that  $P_{e0} \leq 0.1$  and  $P_{e1} \leq 0.1$ . For both cases, the object scene was assumed to be illuminated

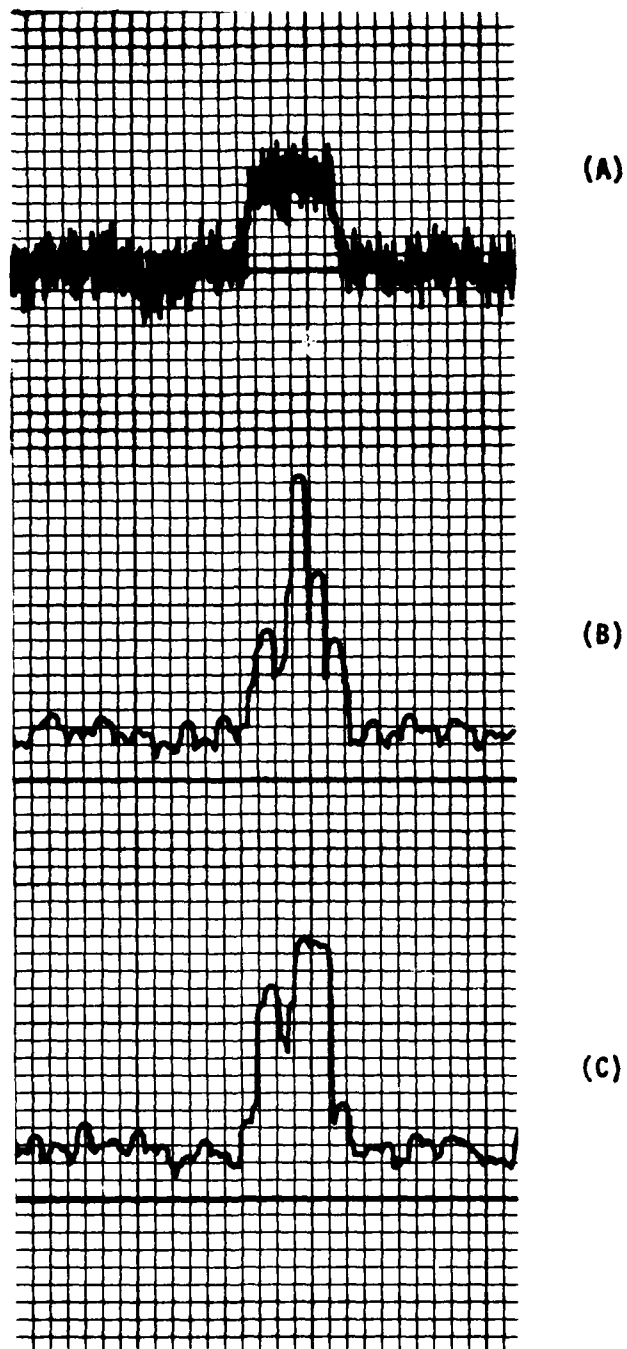


Figure 3-18. Comparison of Smoothed Outputs Obtained With and Without Waveform Inversion.

- a) Two Tone Incoherent Image.
- b) Coherent Image Processed and Smoothed by Rolling Ball.
- c) Coherent Image Processed and Smoothed by Rolling Ball Using Waveform Reversal.

by natural incoherent light. We see from Table 3-2 that the use of a low noise CCD imaging detector together with the rolling ball processing technique can provide a 70 percent improvement in visibility range over direct observation.

Table 3-2

VISIBILITY ATTENUATION COEFFICIENTS (D)  
VERSUS  
VISIBILITY RANGES

D=1 Haze  
D=5 Light Fog  
D=10 Moderate Fog  
D=20 Heavy Fog

RD2= Visibility Range for Direct Viewing  
with 2% Minimum Contrast Criterion  
RD5= Visibility Range for Direct Viewing  
with 5% Minimum Contrast Criterion  
RB1= Visibility Range using Rolling Ball Algorithm  
and a Single Frame  
RB9= Visibility Range using Rolling Ball Algorithm  
and Integrating 9 Frames

$Km^{-1}$	Kilometers			
D	RD5	RD2	RB1	RB9
1	3.0	3.9	6.3	7.4
5	0.60	0.78	1.27	1.49
10	0.30	0.39	0.63	0.74
20	0.15	0.20	0.32	0.37

4  
PHOTOPLASTIC RECORDING

In our earlier work [1-2], we have demonstrated the feasibility of using a grating interferometer to create fringes with the coherent unscattered light. We showed that by recording the target image encoded with the fringe pattern on a photographic plate, the target image can be separated from the background by spatial filtering. Besides being a non-real-time recording material, the silver halide photographic plate also possesses other drawbacks. The silver halide emulsion darkens when exposed to light to produce variations in transmittance. To record a low contrast fringe pattern, the exposure is biased at a region of the transmittance-exposure curve that provides the highest amplitude modulation. There is very little that can be done to enhance the modulation depth. Further exposure of the emulsion only darkens the whole transparency and lowers the amplitude modulation.

A better result can be obtained if the silver halide emulsion is converted from an amplitude modulation material into a phase modulation material. The bias term will simply add a constant phase shift instead of lowering the average amplitude transmittance of the resulting transparency. This allows the use of a higher exposure to create a larger index of modulation. The most common method of producing a phase modulation recording with a silver halide material is bleaching. The bleaching action converts the opaque silver grains into transparent silver salts which exhibit a slightly higher refractive index than the gelatin. Bleaching, however, also tends to increase the amount of scattering noise. We introduced an alternate method called the silver halide gelatin process [1, 10] which alters the local refractive indices in the gelatin. The process produces a transparency with lower scattering noise than simple bleaching. However, with any of these materials and processing techniques, the

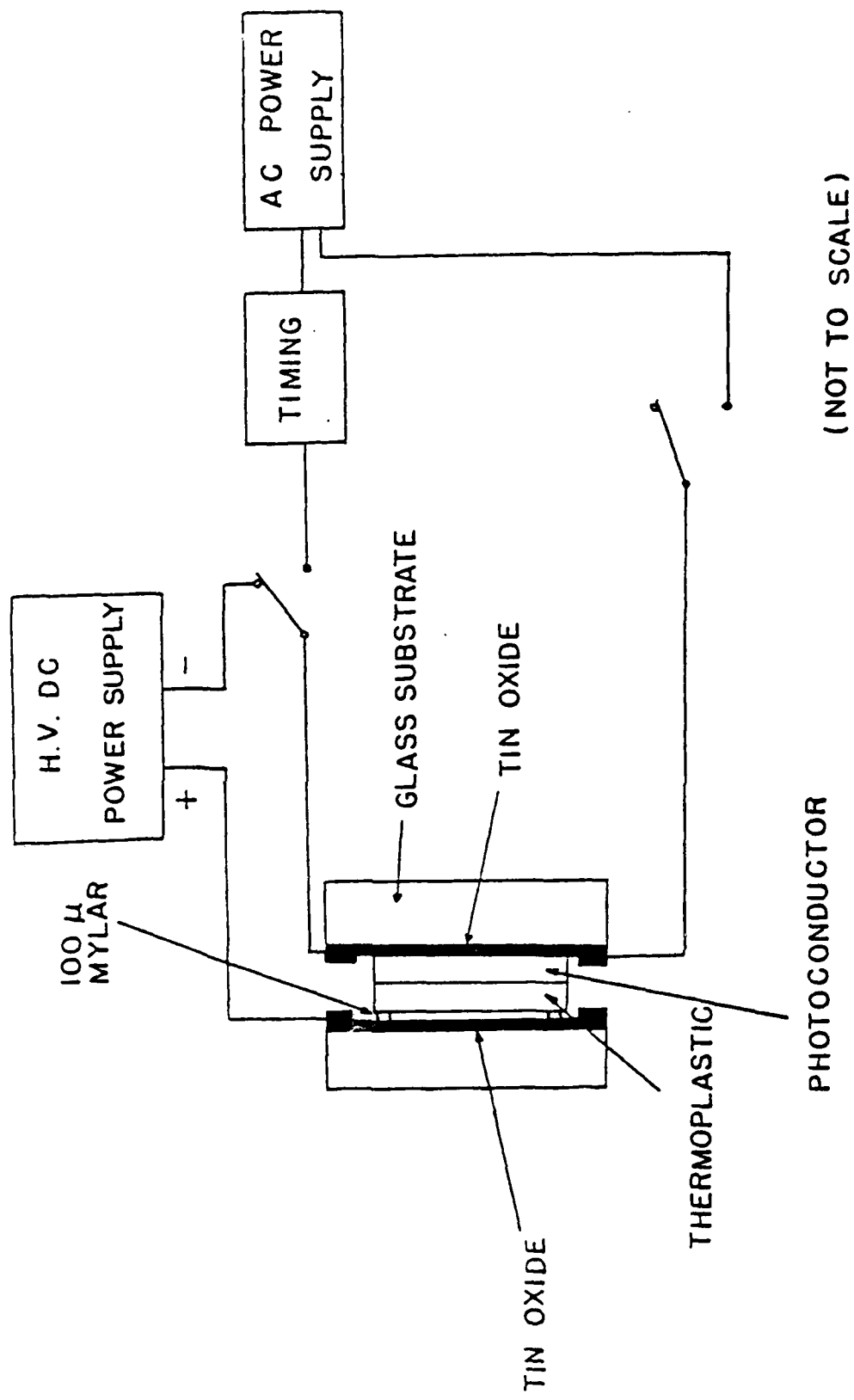
fringe contrast cannot be continuously built up by longer exposures since the amount of light sensitive elements (e.g., silver halide grains) in the material is finite.

The photoconductor-thermoplastic (photoplastic) recording material provides an attractive alternative. There are three main features that makes it suitable for use with a grating interferometer to record low contrast images:

1. The photoplastic is a phase material. As mentioned before, the bias term results only in a constant phase shift instead of causing a reduction in average transmittance.
2. It has a bandpass characteristic. The target image is modulated by a fringe pattern that occupies a finite bandwidth. By matching the bandwidth of the target image to the passband of the photoplastic material, an optimum filtering operation is naturally performed.
3. The most attractive feature of the photoplastic is offered by its unique recording mechanism. Potentially, the device is able to continuously build up the fringe contrast with time. To see how this may be achieved, let us first describe the recording mechanism of the photoplastic recording device.

#### 4.1 RECORDING MECHANISM

The photoplastic is a phase recording material with the input intensity pattern recorded in the form of surface deformation. The basic components of a photoplastic recording device is shown in Figure 4-1. It is composed of a clear substrate (usually glass), coated with a transparent conductive layer (tin oxide or indium oxide) over which is a layer of photoconductive material and then a layer of thermoplastic. For the photoconductor, poly-n-vinyl carbazole (PVK) sensitized with trinitrofluorenone (TNF) can be used with an ester resin thermoplastic (e.g., Herculite Floral 105). Before



(NOT TO SCALE)

Figure 4-1. Composition of a Photoplastic Recording Device.

the exposure, the device is charged either by corona discharge or with a charging plate made of another transparent conductive material as shown in Figure 4-2. After the charging process, the device is then exposed to light. The photoconductor in the exposed areas becomes conductive, and it causes a displacement of negative charges from the conductive layer to the photoconductor-thermoplastic interface. The surface potential of the thermoplastic is proportionally reduced in the exposed areas, producing a spatial variation in the charge pattern that corresponds to the input light intensity distribution. Since the charge density remains more or less unchanged, the electric field in the thermoplastic stays constant. The thermoplastic is then recharged to the original surface potential. The recharging increases the charge density and thus the electric field in the exposed areas. The thermoplastic is then developed by raising the temperature of the thermoplastic to soften point and lowering rapidly the temperature rapidly back to room temperature. This is done by passing a pulse of current through the conductive layer. The electrostatic force, due to the electric field, produces a surface deformation on the thermoplastic according to the input light intensity distribution, and the rapid cooling freezes the deformation. The recording can be erased by raising the temperature of the thermoplastic above the plastic point. The high temperature reduces the resistivity of the thermoplastic and dissipates the electric field across the thermoplastic. This allows the surface tension of the softened thermoplastic to smooth out the surface deformation and erase the recording.

The description above is the standard operating procedure of a photoplastic device. Using it to record low contrast fringes will suffer the same limitation as a photographic plate. The amount of charge placed on the thermoplastic is finite. The surface potential is reduced to zero after a certain exposure level is reached. To be able to build up the variation in electric field when recording the low contrast fringes, the following procedure can be used.



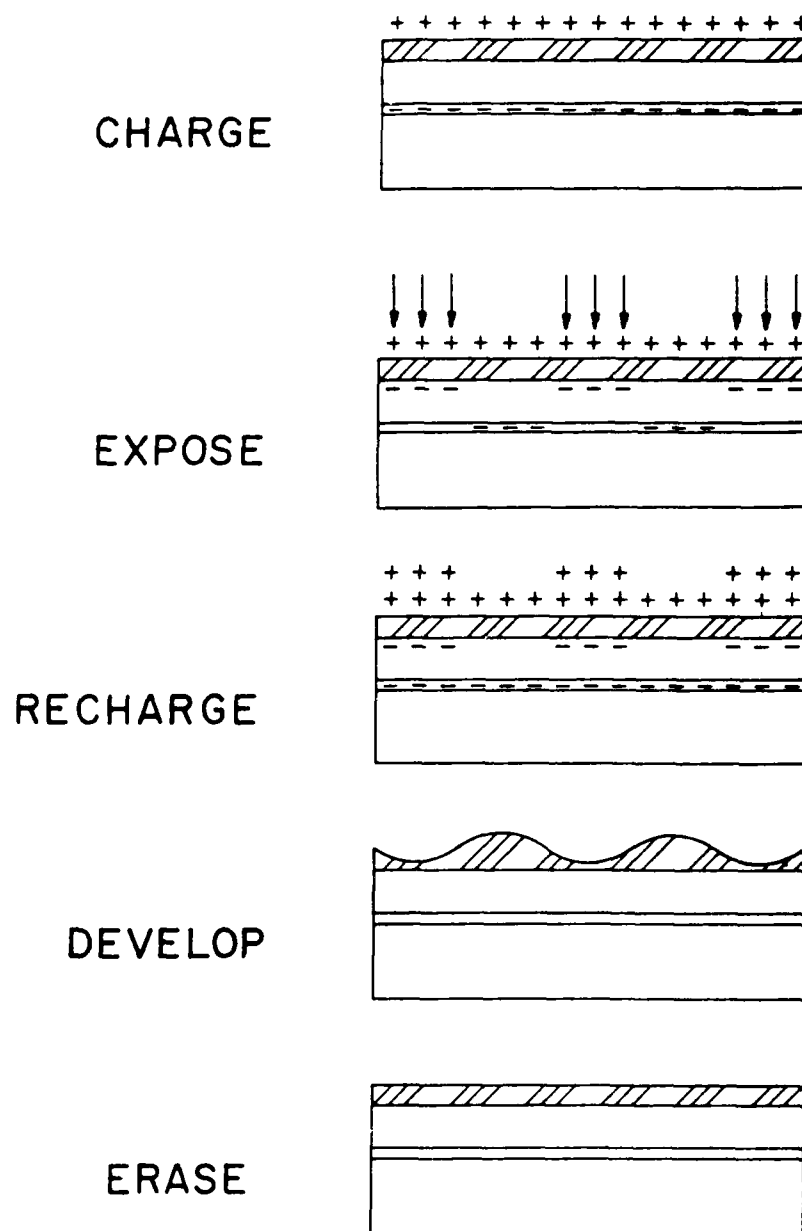


Figure 4-2. Standard Recording Procedure for Photoplastic Device.

Instead of removing the charge before the exposure, the charge is left on when the photoplastic plate is being exposed [11]. The surface potential is thus kept constant, and the electric field in the exposed area increases with time. In order to achieve a continuous buildup of the electric field, the exposure has to be carefully controlled. If the input light intensity is too high, the photoconductor can become so conductive that the surface potential of the thermoplastic cannot be maintained. Ideally, the bias intensity of the incident light should cause a migration of electrons at a rate that is equal to the placement of positive charge on the thermoplastic. When the electric field variation reaches the desired strength, the thermoplastic is heated to produce the deformation. The process is illustrated in Figure 4-3.

To see if this modified operating procedure can indeed improve the ability of the photoplastic device in recording low contrast fringes, the following experiment was performed.

Two coherent collimated beams from an Argon laser were made to interfere at the photoplastic plate and a third incoherent beam was added to provide the bias. The intensities of the beams were adjusted to give a fringe contrast of 2 percent. A small square transparent aperture was inserted in one of the coherent beams and imaged onto a photodetector in the output plane as shown in Figure 4-4. Both operating procedures were utilized in performing the holographic recording. The exposure time was fixed at 5 seconds while the input intensities were varied. After each recording, the bias and object beams were blocked, and the SNR of the reconstructed image was measured. The SNR was defined as the ratio between the intensities in the bright square ring and the dark center. In Figure 4-5, we plotted the measured SNR obtained with the two operating procedures. We see that the modified procedure produces substantially better results.

AD-A126 675

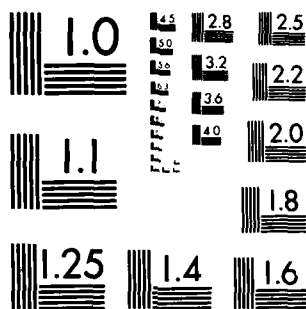
IMAGING SENSOR DEVELOPMENT FOR SCATTERING ATMOSPHERES  
(U) ENVIRONMENTAL RESEARCH INST OF MICHIGAN ANN ARBOR  
RADAR AND OPTICS DIV A M TAI MAR 83 ERIM-155600-3-F  
ARBRL-CR-00508 DAAK11-81-K-0005 F/G 17/8

22

UNCLASSIFIED

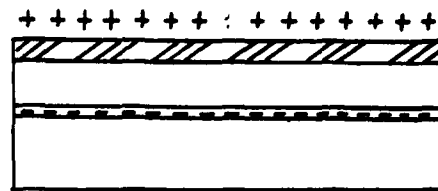
NL

END  
DATE  
FILMED  
4 83  
DTIC

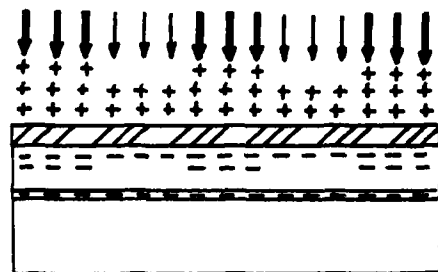


MICROCOPY RESOLUTION TEST CHART  
NATIONAL BUREAU OF STANDARDS-1963-A

Charge



Charge and Expose



Develop

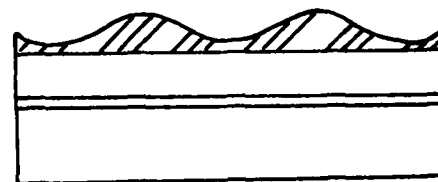


Figure 4-3. Modified Recording Procedures for Low Contrast Fringes.

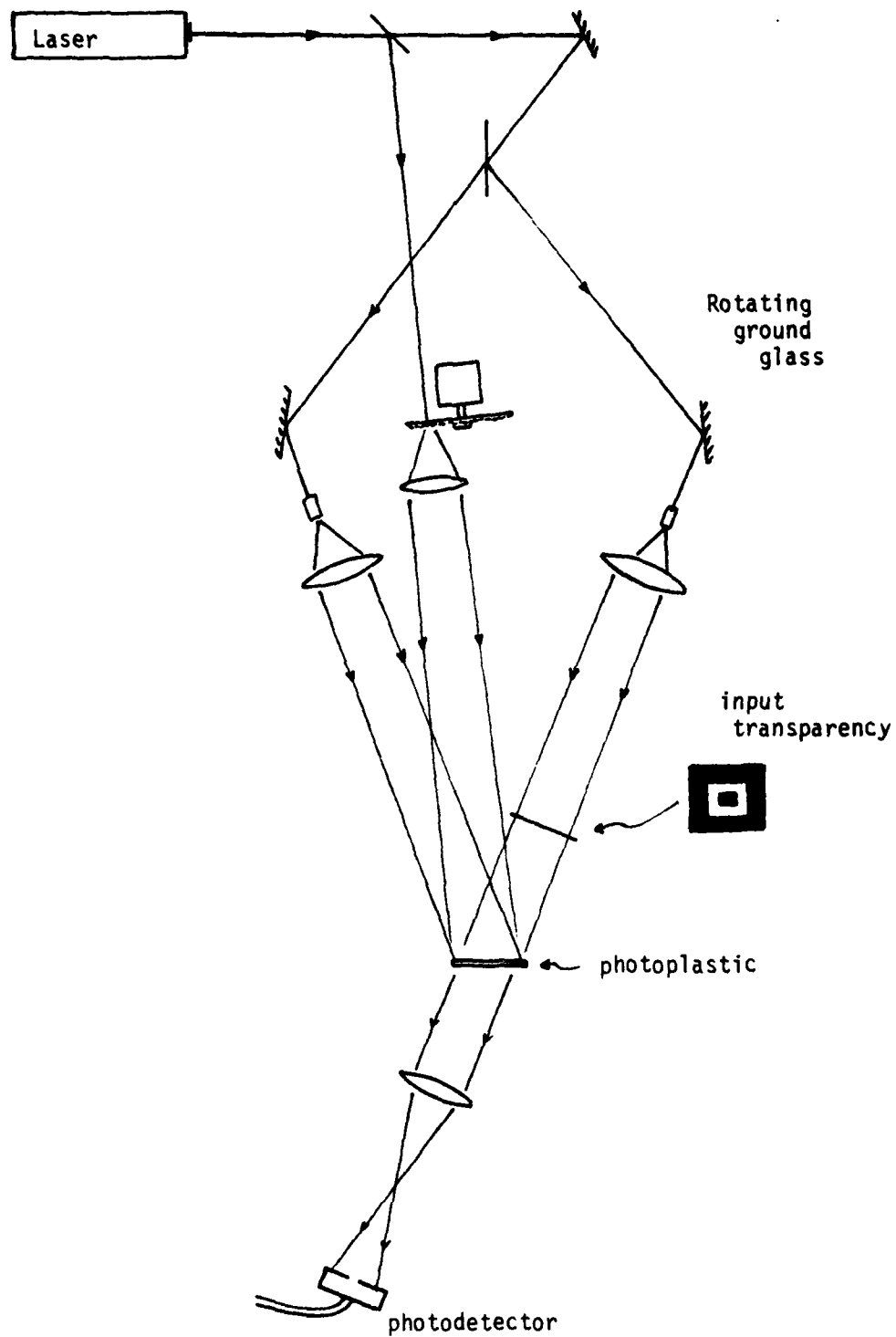


Figure 4-4. Experimental Setup for Testing the SNR Performances of Two Different Recording Procedures on the Photoplastic Device.

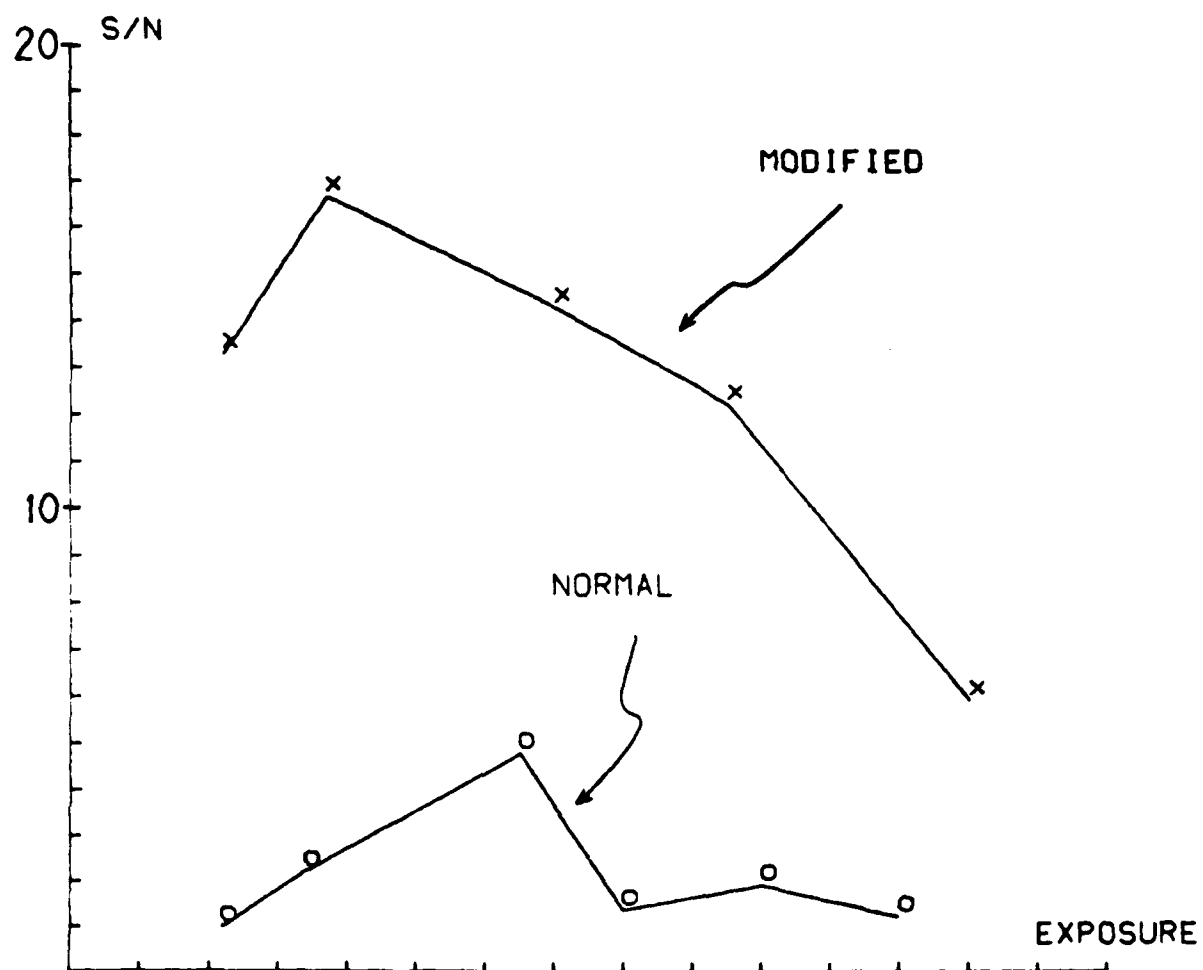


Figure 4-5. SNR Performances of the Photoplastic Device Using the Normal and Modified Recording Procedures.

We next explored the thermoplastic device with a grating interferometer in an optical arrangement as illustrated in Figure 4-6. The experiment we performed in our previous work [1] using the Kodak 649F plate as the recording medium was repeated. In Figure 4-7, the results obtained with the photoplastic devices and the 649F plate are compared. We find the photoplastic device to be much noisier than the 649F plate. However, there is one encouraging note. The output image contrast does not drop as rapidly with the photoplastic. For low modulation inputs, the diffraction efficiency is proportional to the square of the fringe modulation, the fact that the output image contrast decreased at a slower rate seems to indicate that some gain in fringe contrast was obtained.

One reason for the poor result is that the photoplastic device we used was optimized for cycling life time instead of SNR. Frost formation is found on most photoplastic and elastomer devices. Different techniques have been proposed to suppress the frost. They include the use of thermoplastic with very uniform molecular weight [12] and very thin thermoplastic layer [11]. The cycle life time of these photoplastic devices, however, tends to be much shorter.

The ability of the photoplastic device to build up the fringe contrast makes it potentially useful for imaging through scattering media. However, present-day devices have several drawbacks that limit their usefulness.

1. Thermoplastic materials that exhibit good SNR have short life time while thermoplastic that has long life time tends to be noisy. More material development is needed to improve the performance of the thermoplastic.
2. The photoplastic device utilizes heat for development and erasure. Since it takes time for heat to dissipate, the cycle time is relatively slow. Force cooling can be used to improve the cycling rate. However, it will be very difficult to achieve T.V. frame rate.



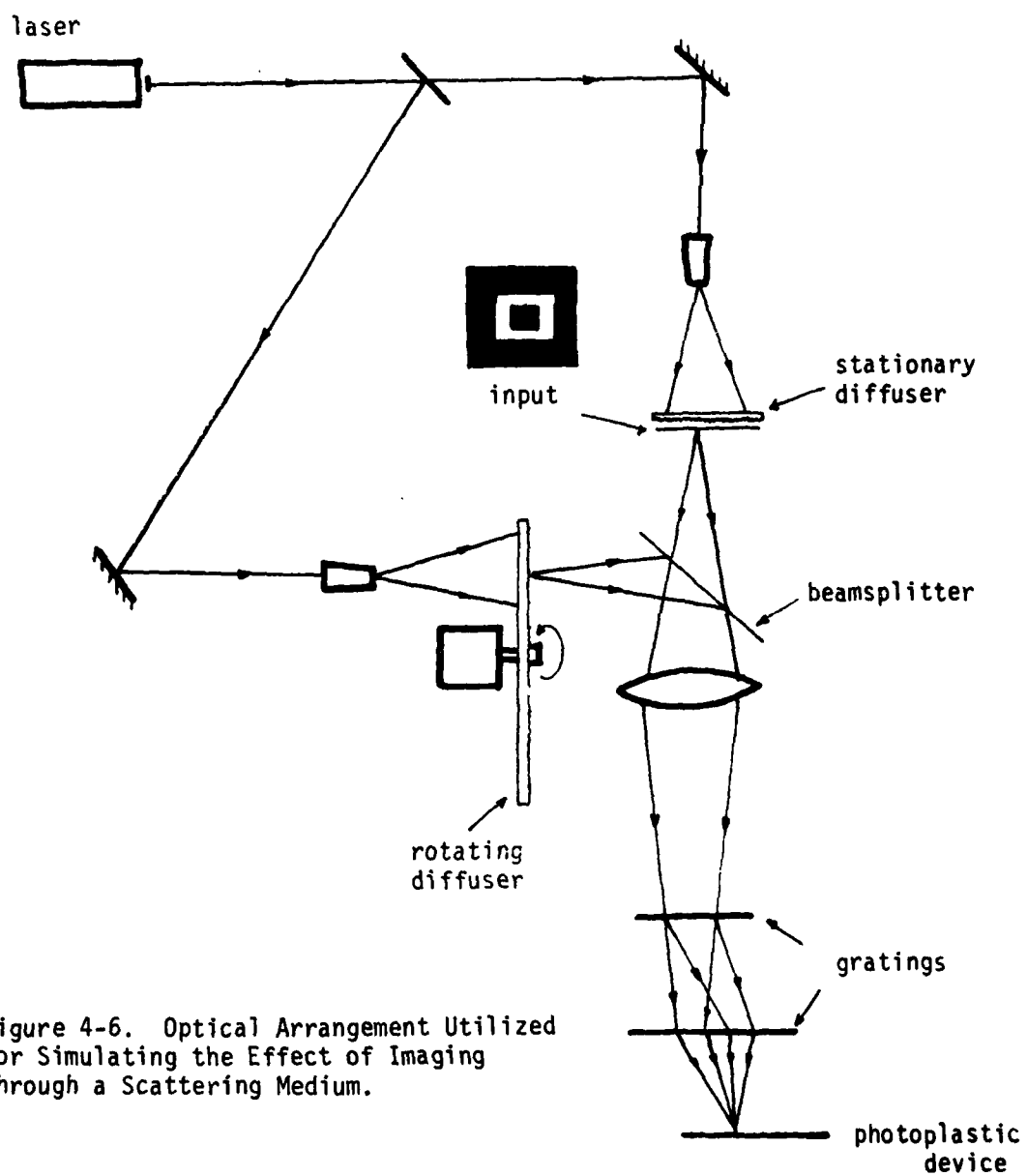


Figure 4-6. Optical Arrangement Utilized for Simulating the Effect of Imaging through a Scattering Medium.

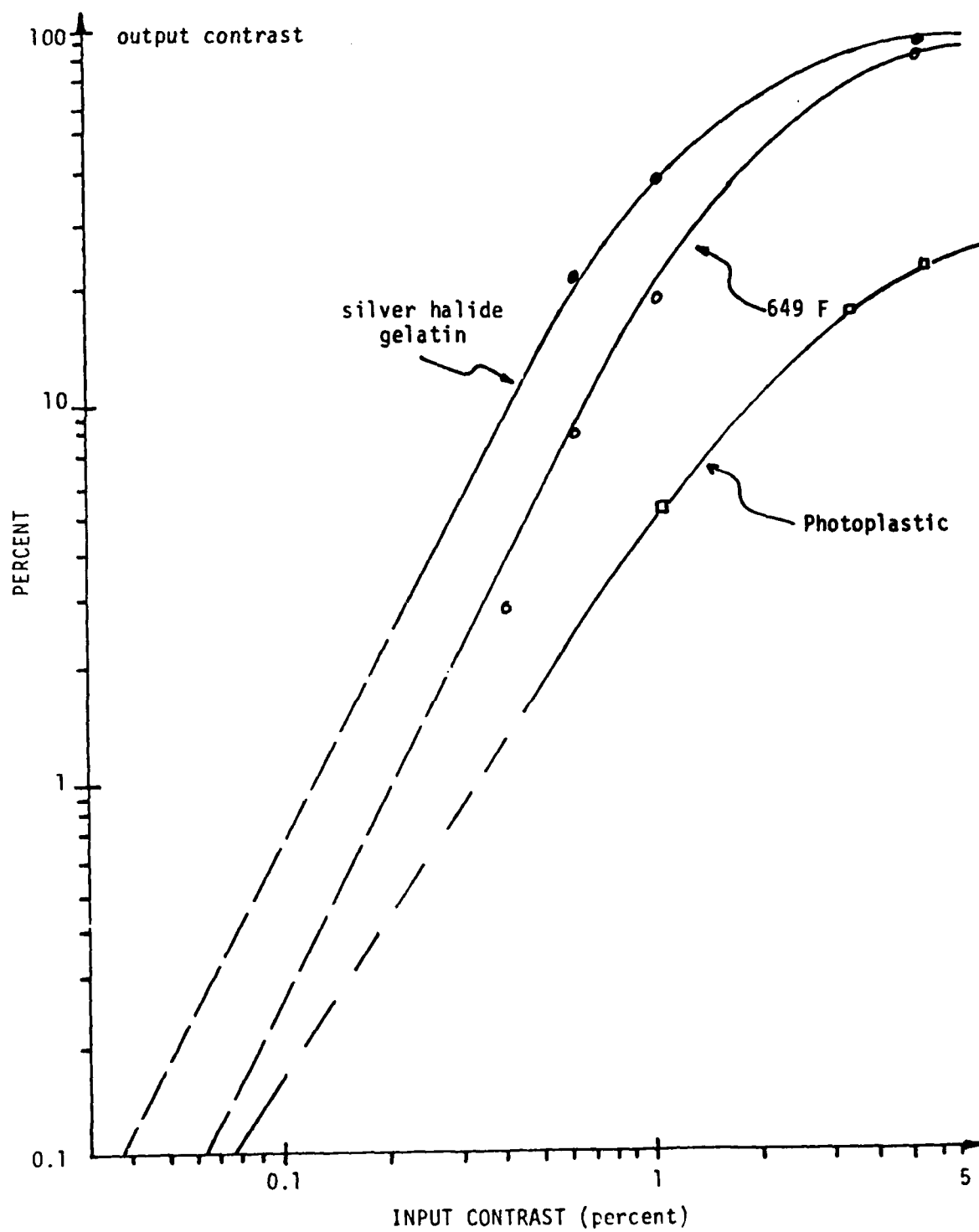


Figure 4-7. Performances of the Photoplastic Device and Kodak 649F Plates in Imaging Low Contrast Signal.

3. The sensitivity of current devices is quite low, and it is limited to the visible region. In imaging through scattering media, it is desirable to operate at longer wavelengths where scattering is less severe. Further research is needed to develop photoconductors that can respond efficiently in the infrared region.

## 5 CONCLUSIONS AND RECOMMENDATIONS

We examined in this report several approaches to a sensor system for imaging through scattering media. The sensor system consisted of a receiver followed by a processor, and design aspects of both subsystems were considered. Selected approaches for near real-time implementation of the processor using digital and analog techniques were studied, and an interferometric approach to the receiver design was introduced.

The various approaches investigated are summarized in the functional diagram shown in Figure 5-1. The basic operation in enhancing images obtained through a scattering atmosphere is to separate the background bias caused by the scattering light from the target image formed by the unscattered light. For coherently illuminated targets, the separation can be achieved by discriminating between the coherence properties of the scattered and unscattered light. Specifically, the ability of coherent light to form interference patterns is utilized to separate coherent and incoherent components in the detected light field. The advantage of this method is that a nearly complete removal of the background bias can be achieved without degradation of the target image. Its applicability, however, is limited to situations where it is possible to actively illuminate the target area with coherent light. For incoherently illuminated targets (or self-luminous objects), the background bias and the target image can often be separated by the differences in their spatial frequency contents. Whenever the intensity of the background bias changes slowly across the image while image contains high spatial frequency details then the target image can be enhanced by a two-dimensional filtering process utilizing analog, digital or hybrid techniques.

Although real-time operation is directly achievable with analog processing techniques, analog approaches tend to be more limited in their capabilities. Frame integration of video images and detector

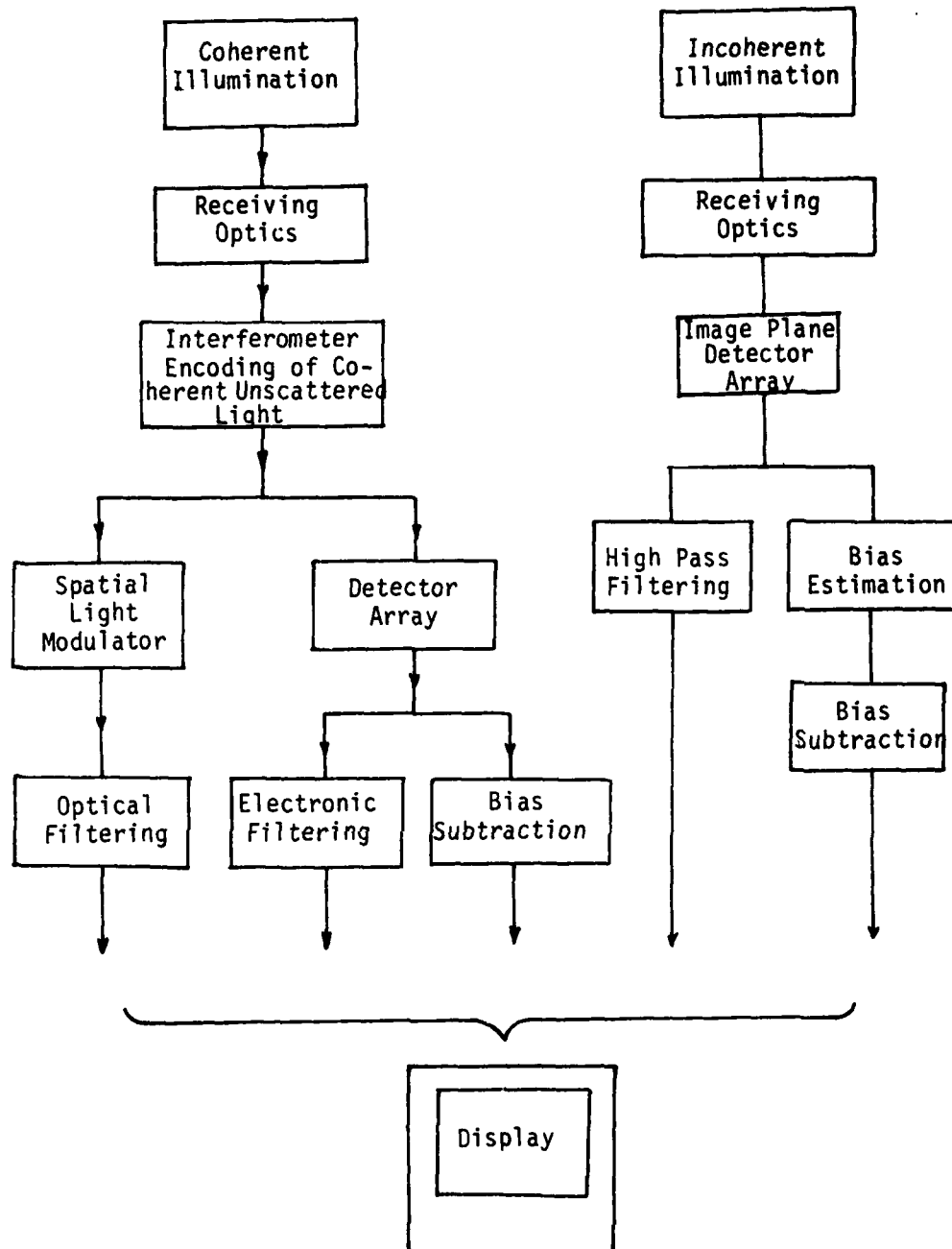


Figure 5-1. Functional Diagram of Approaches for an Imaging Sensor for Scattering Atmospheres.

pattern noise removal are two examples where digital techniques are more effective than analog techniques. In order to eliminate pattern noise, it is necessary to store the noise pattern in memory which is then recalled and subtracted from the processed image. Analog processing also tends to produce images with lower SNR since additional system noise is introduced as the signal propagates through the processing channel. But with digital processing, after the initial digitization, the inherent SNR can usually be maintained no matter how many processing channels are implemented. While analog processing permits only a limited number of processing operations, digital processing can perform any operation that can be mathematically described. Image data can be stored and retrieved as needed and the memory can be maintained for a long period of time without degradation. However, real-time operation is more difficult to achieve with digital processing since the amount of data representing an image is very large. Real-time (T.V. frame rate) processing typically requires a great deal of parallelism in the processing hardware and software.

We examined in detail a very effective digital approach suitable for real-time implementation. Operating on neighboring pixels, the algorithm provides a good estimate of the distribution of the background bias created by the scattered light and subtracts it off the image data. The algorithm involves only simple operations and requires little memory. The simplicity of the algorithm permits a real-time processor to be constructed at a modest cost. The ultimate visibility limit is determined by the dynamic range of the imaging detector and the amount of time available for integration. Without integration (i.e., operating on a single frame), the visibility range is increased by about 70 percent over direct observation using currently available CCD detector arrays.

An alternate approach is to perform the more complex operation of estimating the bias distribution by analog techniques such as low pass filtering or defocussing, or by digital techniques such as image

subtraction and frame integration. If active coherent illumination is used, the background can also be obtained by interferometric techniques. Since only the coherent unscattered light is affected by the changes made in the interferometer, the intensity distribution of the incoherent scattered light forming the background is unchanged between frames. Thus, by subtracting successive frames, the background can be completely removed. To be able to implement the interferometric technique, the imaging detector must be able to resolve the interference pattern. The pixel sizes of imaging detectors available today are fairly large. Resolving the interference pattern requires either the wavelength be long or the numerical aperture of the imaging lens be small. Thus, higher efficiency with the interferometric technique is obtained at the longer wavelengths (e.g., in the infrared).

As indicated, the system efficiency, especially at short wavelengths, tends to be limited by the pixel size of the detector. Spatial light modulators such as photographic film and photoplastic are capable of resolving extremely small patterns. Photographic materials, however, require a slow chemical development process. Photoplastic, on the other hand, offers near real-time capability. (The photoplastic can be developed in a few milliseconds, but the erasure step requires hundreds of milliseconds to complete.) In addition, the unique recording mechanism of the photoplastic device permits the fringe contrast to be built up. However, these devices tend to form frost-like patterns on the thermoplastic that introduce significant scattering noise. The frost formation can be suppressed with the use of thermoplastic with very uniform molecular weight. Unfortunately, these materials also have a short cycle lifetime. More material development work is necessary to improve the devices' SNR performance and sensitivity and to extend the spectral response of the device to the infrared region. However, there is still a strong potential that the photoplastic can be useful in a sensor system for imaging through scattering media.

Digital techniques are versatile, and real-time operation can be achieved using efficient algorithms such as the "rolling ball" algo-

rithm. If coherent illumination of the target is possible, the image can be further enhanced by spectral filtering and speckle encoding.

In Figure 5-2, we illustrate a possible integrated design of a multimode sensor system for imaging through scattering media. We note that the achromatic geometry used for the grating interferometer allows the system to be operated with both monochromatic and wideband illumination. When coherent illumination is available, the grating interferometer can be used to generate the contrast reversal on the interference pattern, as described in Section 2. Alternatively, the rolling ball processing can be applied directly on the speckled image, as presented in Section 3. When imaging targets under natural incoherent illumination, the grating front end will be inactive, and the rolling ball processing technique is applied to enhance the image contrast. The system can be designed to allow the user to define operation mode, integration period, ball size and shape, threshold level and intensity scaling factor in order to optimize the enhancement process.



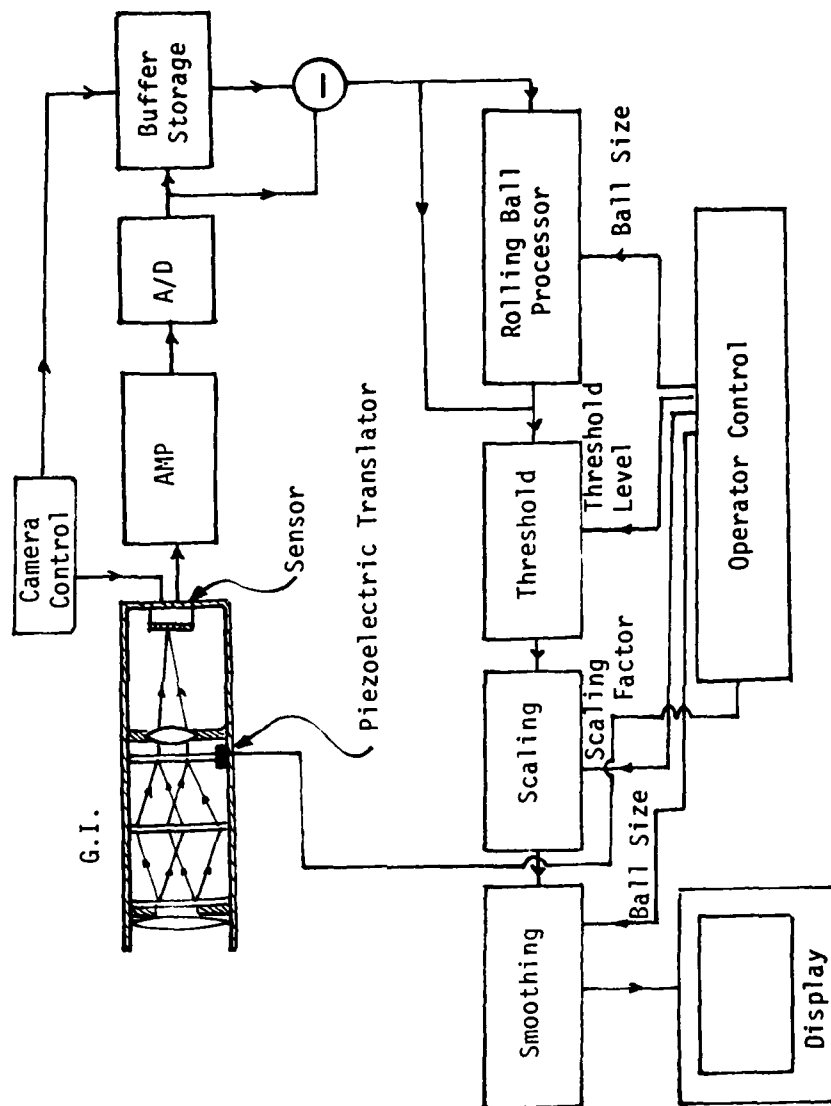


Figure 5-2. Multimode Sensor System for Imaging through Scattering Media.

# REFERENCE LIST

1. Anthony M. Tai and Carl C. Aleksoff, "Holographic Imaging through Scattering Media," Final Report to U.S. Army ARRADCOM, ARBRL-CR-00439 (AD A093480).
2. A.M. Tai, C.C. Aleksoff, and B.J. Chang, "Imaging through Scattering Media by Interferometric Techniques," Appl. Opt. 20, p. 2484, 1981.
3. Anthony M. Tai and Carl C. Aleksoff, "Transmission of Incoherent Images through Scattering Media with a Grating Interferometer," Optics Letter, 6, p. 308, 1981.
4. W.S. Colburn and B.J. Chang, "Photoconductor-Thermoplastic Image Transducer," Opt. Eng., 17, p. 334, 1978.
5. W.S. Colburn and E.N. Tompkin, "Improved Thermoplastic-Photoconductor Devices for Holographic Recording," Appl. Opt. 13, p. 2934, 1974.
6. T.D. Beard, W.P. Bleha and S.Y. Wong, "AC Liquid Crystal Light Values," Appl. Phys. Letter, 22, p. 90, 1973.
7. S. Iwasa and F. Feinleb, "The PROM Device in Optical Processing Systems," Opt. Eng., 13, p. 235, 1974.
8. E.B. Champagne, "A Qualitative and Quantitative Study of Holographic Imaging," Ph.D. Dissertation, Ohio State University, University Microfilms, No. 67-10876, 1967.
9. J.W. Goodman, "Statistical Properties of Laser Speckle Patterns," Laser and Related Phenomena, Ed. J.C. Dainty, Springer-Verlag, New York, 1975.
10. B.J. Chang and K. Winick, "Silver Halide Gelatin Holograms," Proc. SPIE, 215, 1980.
11. T.L. Credelle and F.W. Sprong, "Thermoplastic Media for Holographic Recording," RCA Review, 33, p. 206, 1972.
12. S. Reich, Z. Rav-Noy and A.A. Friesem, "Frost Suppression in Photoconductor-Thermoplastic Holographic Recording Devices," Appl. Phys. Letter, 31, p. 654, 1977.

# DISTRIBUTION LIST

<u>No. of Copies</u>	<u>Organization</u>	<u>No. of Copies</u>	<u>Organization</u>
12	Administrator Defense Technical Info Center ATTN: DTIC-DDA Cameron Station Alexandria, VA 22314	1	Commander US Army Communications Research & Development Command ATTN: DRDCO-PPA-SA Fort Monmouth, NJ 07703
1	Commander US Army Materiel Development & Readiness Command ATTN: DRCDMD-ST 5001 Eisenhower Avenue Alexandria, VA 22333	1	Commander US Army Electronics Research & Development Command Technical Support Activity ATTN: DELSD-L Fort Monmouth, NJ 07703
2	Commander US Army Armament Research & Development Command ATTN: DRDAR-TSS Dover, NJ 07801	1	Night Vision Electro Optics Laboratory ATTN: C. Freeman Fort Belvoir, VA 22060
1	Commander US Army Armament Materiel Readiness Command ATTN: DRSAR-LEP-L Rock Island, IL 61299	1	Commander US Army Missile Command ATTN: DRSMI-R Redstone Arsenal, AL 35898
1	Director US Army ARRADCOM Benet Weapons Laboratory ATTN: DRDAR-LCB-TL Watervliet, NY 12189	1	Commander US Army Missile Command ATTN: DRSMI-YDL Redstone Arsenal, AL 35898
1	Commander US Army Aviation Research & Development Command ATTN: DRDAV-E 4300 Goodfellow Blvd. St. Louis, MO 63120	1	Commander US Army Missile Command ATTN: Dr. Charles R. Christensen Redstone Arsenal, AL 35898
1	Director US Army Air Mobility Research & Development Laboratory Ames Research Center Moffett Field, CA 94035	1	Commander US Army Tank Automotive Research & Development Command ATTN: DRSTA-TSL Warren, MI 48090
1	Commander US Army Armament Research & Development Command ATTN: DRDAR-TDC Dover, NJ 07801	2	Commandant US Army Infantry School ATTN: ATSH-CD-CSO-OR Fort Benning, GA 31905

# DISTRIBUTION LIST

<u>No. of Copies</u>	<u>Organization</u>	<u>No. of Copies</u>	<u>Organization</u>
1	Director US Army TRADOC Systems Analysis Activity ATTN: ATAA-SL White Sands Missile Range NM 88002		<u>Aberdeen Proving Ground</u>  Dir, USAMSAA ATTN: DRXSY-D DRXSY-MP, H. Cohen  Cdr, USATECOM ATTN: DRSTE-TO-F
2	Environmental Research Institute of Michigan ATTN: Dr. Anthony M. Tai/ Dr. Carl C. Aleksoff Radar and Optics Div. P.O. Box 8618 Ann Arbor, MI 48107		Dir, CSL Bldg E3516, EA ATTN: DRDAR-CLB-PA DRDAR-CLN DRDAR-CLJ-L  Dir, CSL ATTN: E. Steubing J. Vervier Bldg E3516, EA
1	Environmental Research Institute of Michigan ATTN: Carl D. Leonard Electro Optics Dept. P.O. Box 8618 Ann Arbor, MI 48107		Cdr, PM Smoke & Obscurants ATTN: DRCPM-SMK Bldg 324
1	University of Connecticut Department of Chemistry ATTN: Prof. C. E. Waring Storrs, CT 06268		

### USER EVALUATION OF REPORT

Please take a few minutes to answer the questions below; tear out this sheet, fold as indicated, staple or tape closed, and place in the mail. Your comments will provide us with information for improving future reports.

1. BRL Report Number \_\_\_\_\_

2. Does this report satisfy a need? (Comment on purpose, related project, or other area of interest for which report will be used.)  
\_\_\_\_\_  
\_\_\_\_\_  
\_\_\_\_\_

3. How, specifically, is the report being used? (Information source, design data or procedure, management procedure, source of ideas, etc.) \_\_\_\_\_  
\_\_\_\_\_  
\_\_\_\_\_

4. Has the information in this report led to any quantitative savings as far as man-hours/contract dollars saved, operating costs avoided, efficiencies achieved, etc.? If so, please elaborate.  
\_\_\_\_\_  
\_\_\_\_\_  
\_\_\_\_\_

5. General Comments (Indicate what you think should be changed to make this report and future reports of this type more responsive to your needs, more usable, improve readability, etc.) \_\_\_\_\_  
\_\_\_\_\_  
\_\_\_\_\_  
\_\_\_\_\_

6. If you would like to be contacted by the personnel who prepared this report to raise specific questions or discuss the topic, please fill in the following information.

Name: \_\_\_\_\_

Telephone Number: \_\_\_\_\_

Organization Address: \_\_\_\_\_  
\_\_\_\_\_  
\_\_\_\_\_

----- FOLD HERE -----

Director  
US Army Ballistic Research Laboratory  
ATTN: DRDAR-BLA-S  
Aberdeen Proving Ground, MD 21005



NO POSTAGE  
NECESSARY  
IF MAILED  
IN THE  
UNITED STATES

OFFICIAL BUSINESS  
PENALTY FOR PRIVATE USE, \$300

**BUSINESS REPLY MAIL**  
FIRST CLASS PERMIT NO 12062 WASHINGTON, DC  
POSTAGE WILL BE PAID BY DEPARTMENT OF THE ARMY

Director  
US Army Ballistic Research Laboratory  
ATTN: DRDAR-BLA-S  
Aberdeen Proving Ground, MD 21005



----- FOLD HERE -----

FILMED  
— 8